# ACTIVE LEARNING METHODS FOR COMPUTATIONAL DELINEATION AND CELLULAR PROFILING OF CORTICAL LAYERS IN RAT WHOLE BRAIN SECTIONS USING MULTIPLEX IMMUNOFLUORESCENT IMAGING AND CLASSIFICATION OF HISTOPATHOLOGICAL IMAGES USING CONVOLUTIONAL NEURAL NETWORKS

by
Aditi Singh

A Dissertation submitted to the Electrical and Computer Engineering Department,
The Cullen College of Engineering
in partial fulfillment of the requirements for the degree of

DOCTOR OF PHILOSOPHY

in Image Processing and Machine Learning

Chair of Committee: Dr. Badrinath Roysam

Committee Member: Dr. Saurabh Prasad

Committee Member: Dr. Dragan Maric

Committee Member: Dr. Hien Nguyen

Committee Member: Dr. David Mayerich

University of Houston
May 2021

**ACKNOWLEDGEMENTS**

First and foremost, I would like to thank my research supervisor, Dr. Badrinath Roysam for his invaluable advice, continuous support, and patience during my PhD study. His immense knowledge, vision and plentiful experience has encouraged me in all the time of my academic research and daily life.

I would also like to show gratitude to my committee, including Dr. Saurabh Prasad, Dr. Hien Van Nguyen, Dr. Dragan Maric and, Dr. David Mayerich. I discussed the early versions of my work on cortical layer delineation with Dr. Prasad. He raised many precious points in our discussion, and I hope that I have managed to address several of them here. I am extremely grateful to have had a chance to work with Dr. Nguyen. His enthusiasm for the topic of deep learning has made a strong impression on me. Dr. Maric helped me advance the morphological segmentation and cortical layer delineation algorithms during my internship at NINDS, NIH and after that as well. Even though I have not had the opportunity to work with Dr. Mayerich previously, he has provided me constructive feedback throughout on my work.

I am so grateful to my lab members Dr. Xiaoyang Li, Dr. Jahandar Jahanipour, Dr. Hengyang Lu, Dr. Kedar Grama, and Rachel Mills who not only made my doctoral journey fun, but also provided great ideas during our numerous impromptu brain storming sessions. I also appreciate Farideh Foroozandeh, Pengyu Yuan, Dr. Leila Saadatifard, and Dr. Aryan Mobiny, and collaborators Dr. Dash Pramod, Dr. John Redell, Dr. Kannan Kasthuri and Anthony Wang for all the illuminative discussions I have had with each of them. My sincere appreciation goes to Dr. Mark Maynard for providing continuous feedback on my work from a biologist's perspective.

I would like to express my gratitude to my parents. Without their tremendous understanding and encouragement in the past few years, it would be impossible for me to stay optimistic and keep progress. I owe all my achievements to them. Special thanks to Abhay Gupta for all the home-cooked meals he has provided me along with care and support in the past few months. I thank my dog, Candy for ensuring that I get some fresh air daily during this pandemic era of remote work. I thank everyone who has ever helped me directly or indirectly in the past decades. I would also like to express my appreciation to Stack Overflow, GitHub and myriad other publicly available online resources which have been of help.

Lastly, my gratitude extends to Cullen College of Engineering and National Institute of Health for funding my studies and this research respectively that allowed me to conduct this thesis.

**ABSTRACT**

Most machine learning algorithms require an abundance of high-quality training data. Such a requirement creates a major obstacle when using machine learning in the medical image domain, as labeled data collection is difficult. We explore active learning solutions for cortical layer delineation and for training Convolutional Neural Networks with less amount of labeled data. For the former, we develop an objective and automated multiplex imaging-based method for delineation of cortical layers in the whole brain sections. This is an advance over current methods where layers are visually delineated by biologists. We further carryout comprehensive and quantitative profiling of the cell layers with respect to their composition (presence of neuronal and glial cell types and sub-types), cell-phenotypic status, and the spatial arrangement of cells. Our method is based on spatial cluster analysis of neuronal features using the Dirichlet Process Mixture Model and refined using active machine learning. It is versatile, modular, and readily amenable to visual inspection and proofreading. The accuracy of the computational cortical layer delineation was validated by comparing it to brain sections that were immunostained with layer-specific molecular markers (NECAB1, FOXP1) and by comparison against manual delineation by biologists. We implement our proposed method on healthy rat brains and rat brains with mild traumatic brain injury (mTBI). Our in-depth cellular profiling of the layers allows us to study the patterns of tissue perturbations in the cortex for mTBI brains. We propose whole cell morphological segmentation methods for five different types of cells which allow an in-depth analysis of the cell state activation and spatial distribution. These are also used in neuronal feature extraction for cortical layer delineation. For the second implementation of active learning, we formulate an active deep learning framework to train CNNs with less

amount of labeled data. We implement two parallel active learning criteria for the same. We provide extensive experimental results and in-depth analysis to demonstrate the effectiveness of our algorithm on a breast tumor classification problem. We offer active learning solutions for addressing two different problems encountered in whole brain analysis.

**TABLE OF CONTENTS**

## LIST OF TABLES

**LIST OF FIGURES**

# CHAPTER 1 INTRODUCTION

## 1.1 Rat Brain Atlas

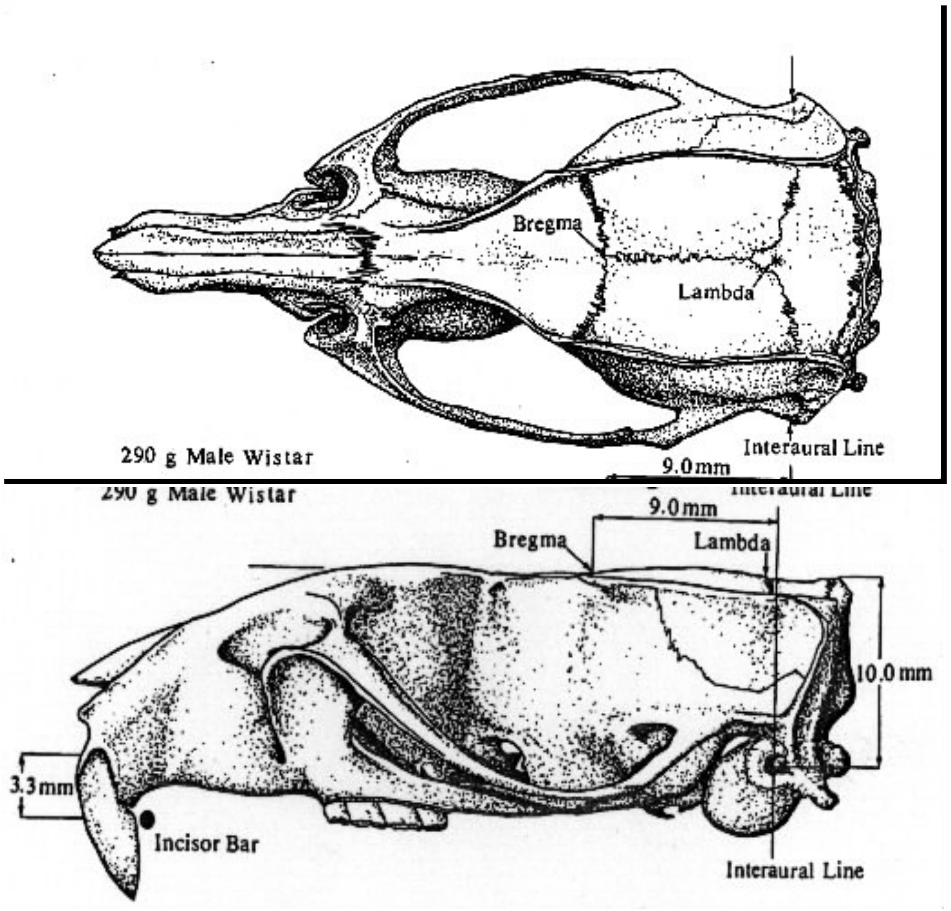


Figure 1-1. Location of Bregma and Lambda in dorsal (top) and lateral (bottom) views of rat skull.

Brain atlases are composed of serial sections of a brain with each section given a coordinate relative to the reference points on the skull (see Figure 1-1 as defined by Dr. George Paxinos [1]). In the rat, three most common reference points are bregma, lambda, and the interaural line. Bregma is the anatomical reference point on the skull at which the coronal suture is intersected perpendicularly by the sagittal suture (bregma=0 for this point). Lambda is the anatomical reference point on the skull where sagittal suture

intersects the interaural line. Interaural line is the straight line between the points of ear bars in the external auditory meatus of each ear.

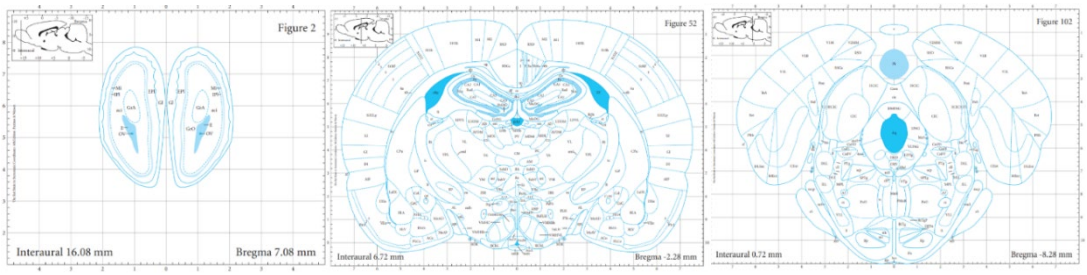


Figure 1-2. Brain atlas for rat coronal level sections from the Paxinos Atlas.

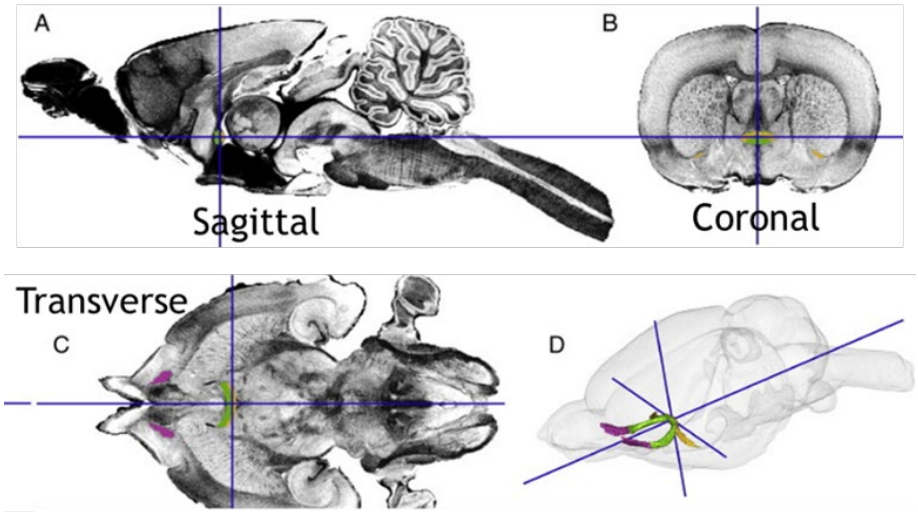


Figure 1-3.Woxholm Space atlas of the Sprague Dawley rat brain.

Each atlas level delineates different brain structures within the section based on a corresponding histologically stained tissue section (see Figure 1-2, from [1]). Brain atlases can depict coronal, sagittal or transverse sections (see Figure 1-3, from [2]**)**. Brain atlases

allow for the ability to identify where relevant structures are normally found in the brain with a high degree of accuracy, helpful in drug administering using stereotaxic surgery.

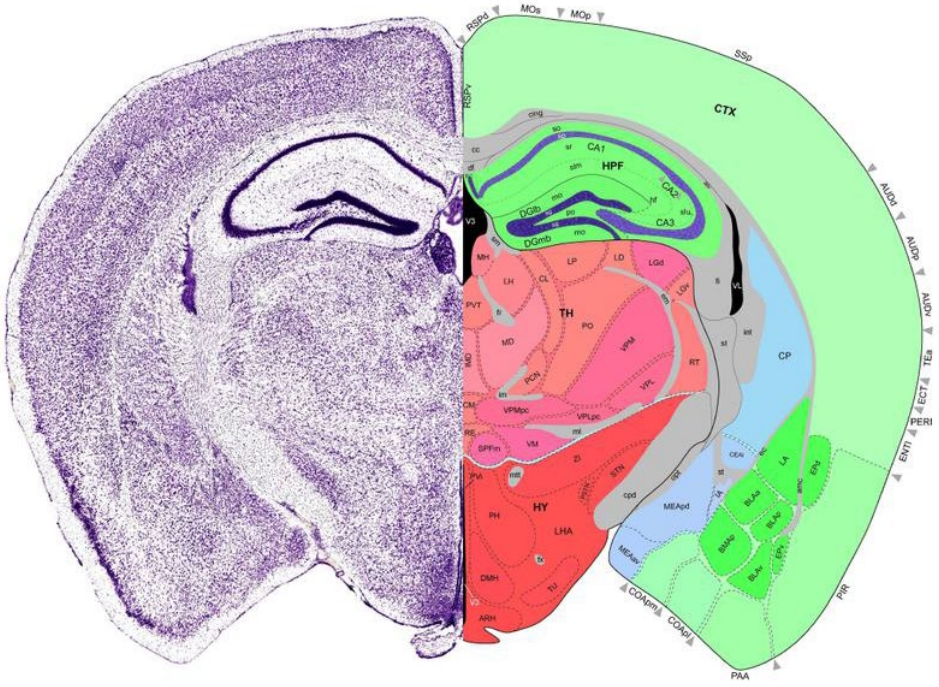


Figure 1-4. Allen Mouse Brain Atlas, 2004. Nissl stain on the left, atlas on the right.

Brain atlas is a guide to the spatial location and identity of brain structures (see Figure 1-4, from [3]). Analogous to “Google Maps” for Neuroanatomy. It can be combined with multiplex imaging or functional imaging to view and analyze brains at the cellular, functional, and structural level. Brain atlas can help in studying anatomy and architecture of different neuronal groups in the rat brain. It provides a neuroanatomy-based interpretation to study structure and function in healthy and diseased brains. Brain atlas allows extraction, quantitative analysis, display, and modeling of neuroanatomical data.

Brain atlases can be used to compare distribution patterns of neuroanatomical data on the same set of templates and a collaborative platform for future brain studies.

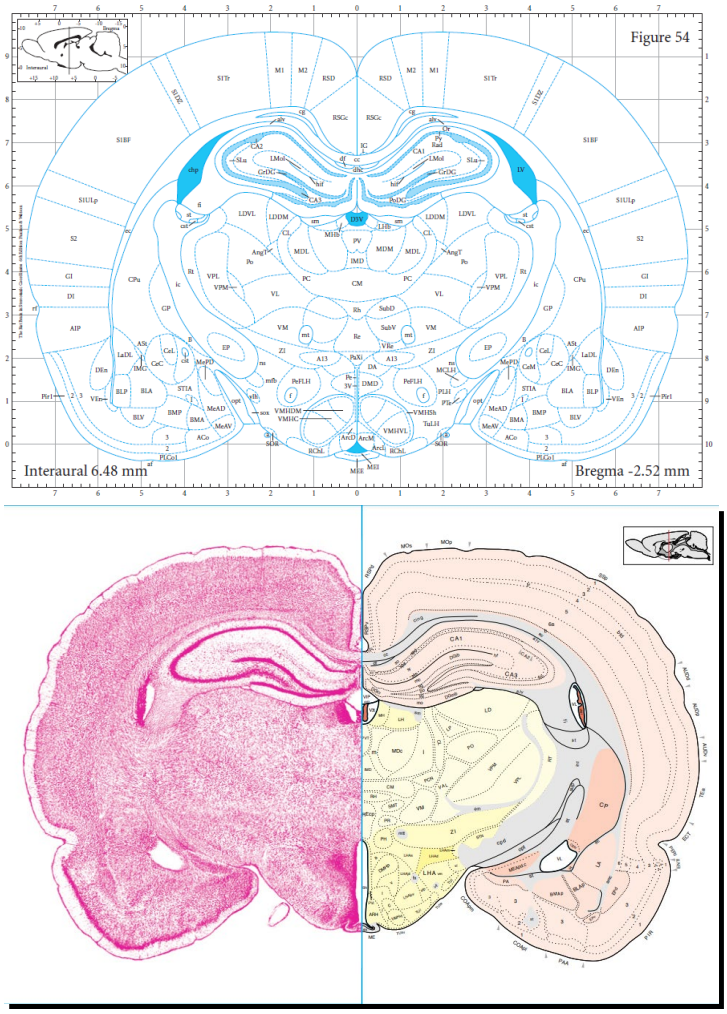


Figure 1-5. Paxinos (top) and Swanson's (bottom) atlases compared for bregma values 2.52mm ± 0.12 mm.

The most popular publicly available brain atlases are Paxinos [1] atlas and Swanson's [4] atlas (see Figure 1-5). The first edition of Paxinos atlas was published in the year 1982. The current 6$^{th}$ edition of the atlas consists of coronal, sagittal, transverse and horizontal sections. For this thesis, we will be working with two-dimensional whole rat brain slices and hence sticking on coronal sections. The Paxinos atlas consists brain mapping for 161

coronal sections each 0.12 mm apart. The Paxinos atlas does not delineate the cortex into cytoarchitectonic layers. Swanson's atlas published in 1992, is an alternative to Paxinos atlas, with cortical layers delineated, and built on the same stereotaxic coordinates. It consists of 73 coronal sections, which are unequally placed, which makes it difficult to use it for a new rat brain (see Figure 1-6). Swanson's atlas offers delineation of the cortical layers, which is an important attribute for this thesis.

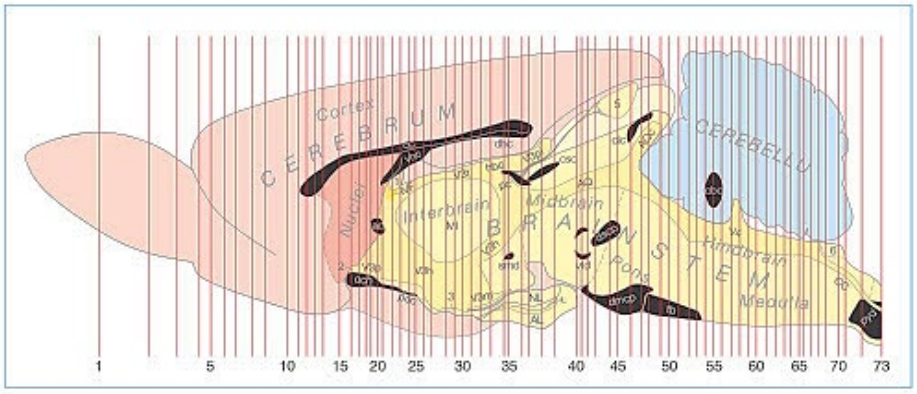


Figure 1-6. The atlas levels in Swanson's atlas.

There is lot of variability in animal brains within and between species, depending on the experiments, age, and other developmental factors. Therefore, atlases should not be used as static, authoritative representations of the brain, but as a rough starting point. Instead these should be used as starting points for a new brain. Both Paxinos' and Swanson's atlases are based on Nissl-stained sections, which stains the RNA and DNA of all neurons in the brain. Due to this, it does not provide any phenotypical marker for cell profiling. Nissl doesn't stain glial cells. Glio-vascular profiling for regions in atlas can help in studying drug treatments.

## 1.2 Cerebral Cortex

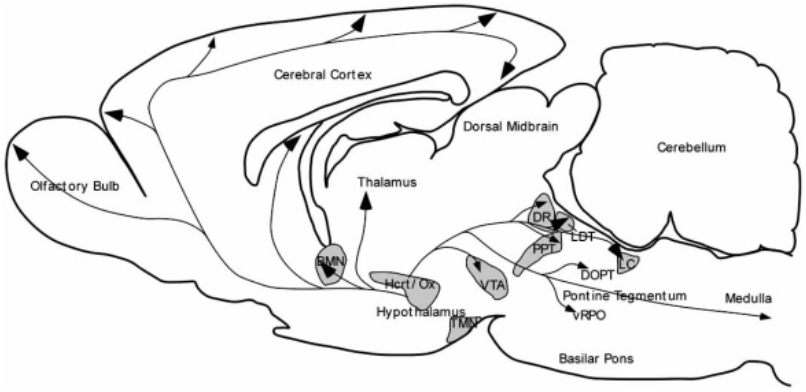


Figure 1-7. Sagittal Scheme of Rat Brain.

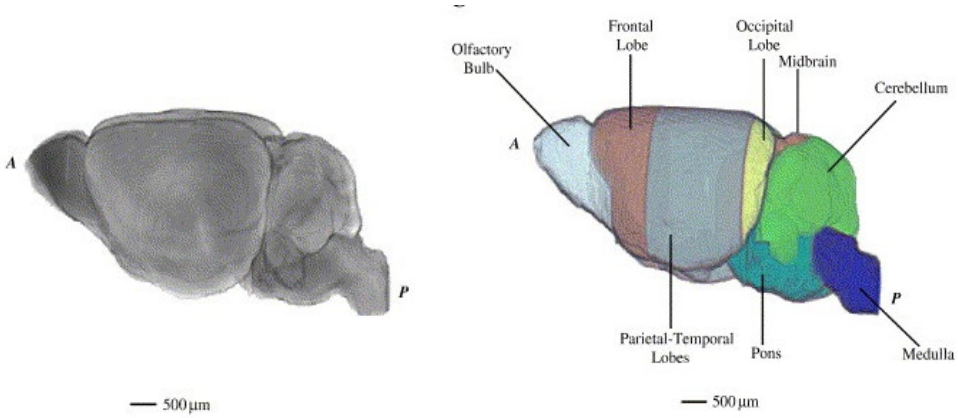


Figure 1-8. Rat brain lobes (Sagittal View).

Cerebral cortex is the most developed part of the brain. The cerebral cortex (see Figure 1-7 from [5]) is the folded or ridged outer layer of the cerebrum and is composed of mostly neuronal cell bodies. The cortex consists of four lobes (see Figure 1-8 from [6]) which control numerous functions. Frontal lobe is responsible for decision making, impulse control and judgement. Parietal lobe is responsible for sensory perception and movement. Temporal lobe is responsible for language, hearing, and memory. Occipital lobe is responsible for primary vision.

## 1.3 Experiment Preparation

Dr. John Redell's team at The University of Texas Health Science Center at Houston has cut healthy rat brains into slides of 10 μm-thick coronal cryo-sections (see Figure 1-9). Each section is incubated using a cocktail mixture of 10 non-cross reactive and spectrally compatible biomarkers [7]. To generate readouts of a rich panel of biomarkers, the sample slides are stained in precisely designed fluorescent protocol in Dr. Dragan Maric's Lab at National Institute of Neurological Disorders and Stroke, National Institute of Health (see Figure 1-10). Then, the full sets of multiplex images of the rat brains are scanned by microscopies (see Figure 1-11).

Figure 1-9. Healthy Rat Brain Sample in UT Health.


Figure 1-10. Tissue Staining in the Wet Lab at NINDS, NIH.

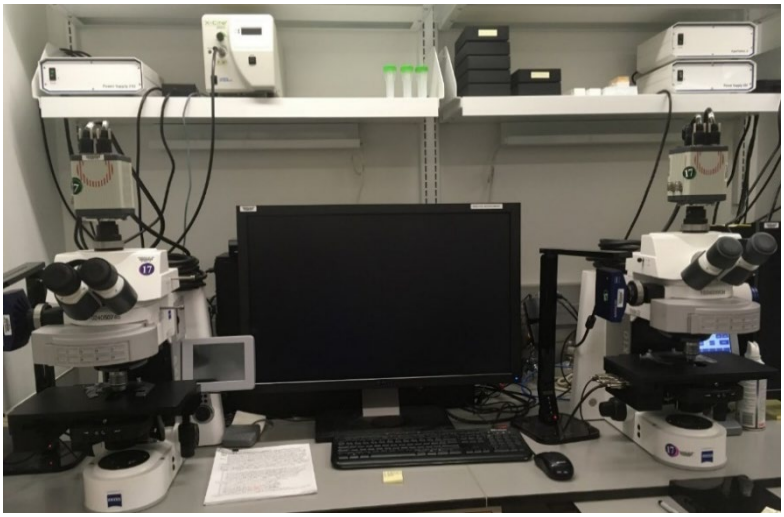

Figure 1-11. Microscopy Imaging in the Dry Lab at NINDS, NIH.

## 1.4 Descriptions of the Dataset

We use three datasets for our study all obtained as per the protocol mentioned in the previous section. First consists of coronal brain section of a healthy 8-week old male Lewis LEW-Tg (CAG-EGFP) YsRrrc transgenic rats. This section is stained in 5 rounds of 11 iterative multiplex IHC (immunohistochemistry) staining each [7] (see Figure 1-12 (A) and Figure 1-13). The second study consists of 12 coronal brain sections belonging to sham-

operated and mTBI (mild traumatic brain injury) rats. We will be using this to denote a normal brain vs. injured vs. drug-treated brains, allowing investigators to analyze the effects of experimental manipulations in a sensitive manner with cell-layer specificity. This dataset has 2 rounds of 10 iterative multiplex IHC. The major channels are DAPI and Histone channels representing the nuclei, and main cell type channels for Neurons, Astrocytes, Oligodendrocytes, Endothelial Cells and Microglia (shown in Figure 1-12 (B)-(F), respectively).

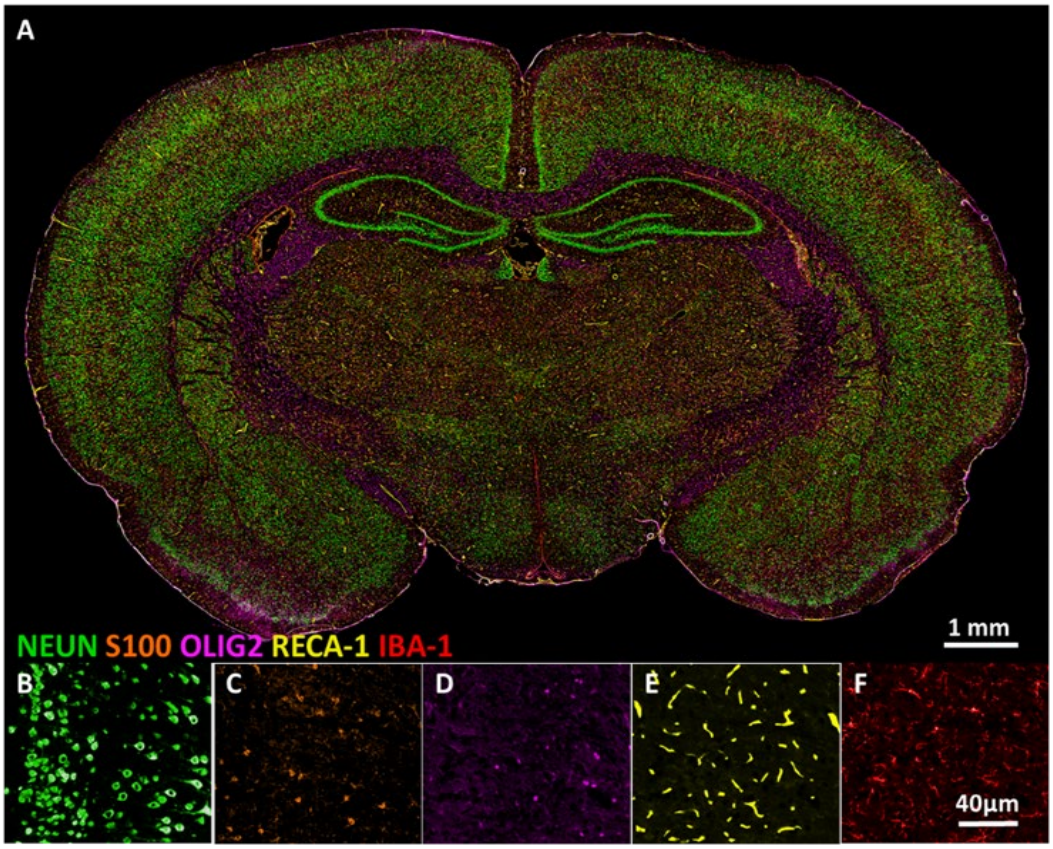


Figure 1-12. Whole Rat Brain Tissue from Multiplex Imaging.

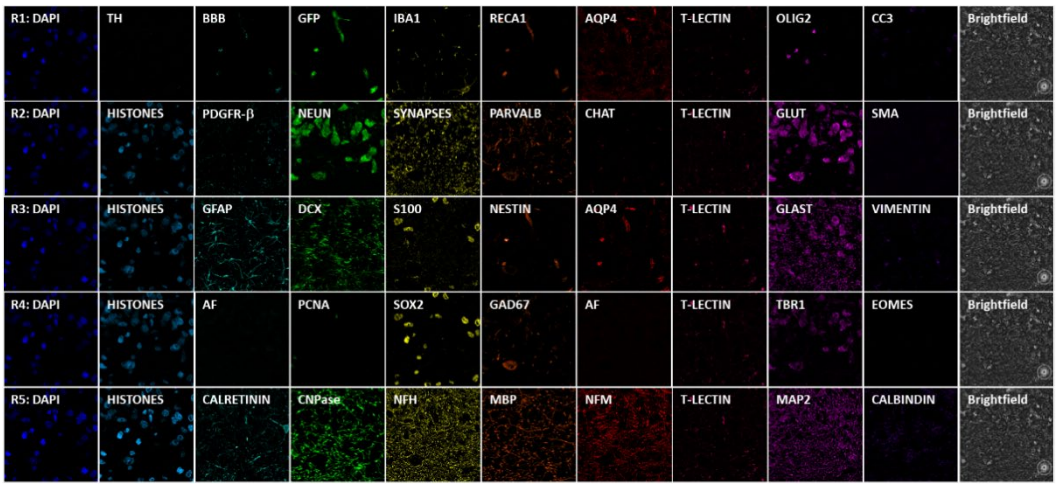


Figure 1-13. Close-up Images from Five 10-plex Imaging Rounds.

The library of molecular markers for the first two dataset is mentioned in Table 1-1. The third dataset for consists of coronal section stained with layer-specific molecular markers along with the molecular markers in Table 1-2 for an accurate quantitative performance analysis.

Table 1-1. Library of primary antibodies used for multiplex IHC staining of rat brain tissue sections.

| Channel ID | Cell Classification | Cell Function |
|---|---|---|
| DAPI | All Nucleated Cells | Gene Expression, Cell Cycle, Death |
| NeuN | Neurons-Pan Specific | Gene Expression |
| RECA1 | Endothelial Cells | Cell Adhesion |
| S100 | Astrocytes-Pan Specific | Cell Signaling-Calcium Mediated |
| Olig2 | Oligodendrocytes | Gene Expression |
| Iba1 | Microglia | Cell Signaling-Calcium Mediated |
| GAD67 | Neurons-GABAergic | Neuronal Signaling-GABAergic |
| Tyrosine Hydroxylase (TH) | Neurons-Dopaminergic | Dopaminergic Signaling |
| Choline Acetyltransferase | Neurons-Cholinergic | Neuronal Signaling-Cholinergic |
| Glutaminase | Neurons-Glutamatergic | Neuronal Signaling-Glutamatergic |
| Cleaved Caspase-3 | Apoptotic Cells | Cell Death |
| Tomato Lectin | Endothelial Cells, Microglia | Cell Adhesion |
| PCNA | All Actively Proliferating Cells | Cell Cycle |
| GFAP | Astrocytes-Subset | Cell Motility, Cell Morphology |
| MAP2 | Neurons-Dendritic Innervation | Neuronal Signaling-Dendritic |

Table 1-2. Library of antibodies for multiplex IHC staining of layer-specific rat brain tissue sections.

| Channel ID | Cell Classification | Cell Function |
|---|---|---|
| DAPI | All Nucleated Cells | Gene Expression, Cell Cycle, Death |
| NeuN | Neurons-Pan Specific | Gene Expression |
| GAD67 | Neurons-GABAergic | Neuronal Signaling-GABAergic |
| Parvalbumin | Interneurons-Subset | Neuronal Signaling-Inhibitory |
| FoxP1 | Neurons-subset | Layer 6 neurons |
| Necab1 | Neurons-subset | Layer 4 neurons |

Traditional nuclei images stained are performed only using DAPI, a DNA binding dye. However, uniquely to the rat brain, some cells' nuclei are barely visible in the DAPI channel. To overcome this problem, Dr. Dragan Maric added a complementary channel using Histone antibodies, enabling more reliable nuclei detection and segmentation results [7]. We will use DAPI and Histone channels for automatic nuclei segmentation by watershed; DAPI, Histone and five main biomarkers for expectation driven segmentation and phenotyping; the main biomarkers and the cell status/ cell subpopulation channels for neighborhood analysis; all 50-plex channels for image registration.

Below (see Table 1-3) are the cortical cell population distributions in the healthy 50-plex datasets calculated using work done in Dr. Jahanipour's thesis [8]. As seen, the cortex is high neuronal density region.

Table 1-3. Cell populations in 50-plex Rat Brain Cortex.

| Cell Type | | Cell Counts |
|---|---|---|
| Neurons | Glutamatergic | 34,728 |
| | GABAergic | 1,808 |
| Vascular Cells | | 13,764 |
| Glial Cells | Oligodendrocytes | 7,891 |
| | Astrocytes | 8,874 |
| | Microglia | 4,269 |

The largest part of the cortex (~ 90%), consists of a phylogenetically newer structure called neocortex, consisting of six layers of stacked nerve cell bodies. Layers are delineated into 1, 2+3, 4, 5, 6a and 6b (see Figure 1-14). The shapes and diameters of neuron somata vary as a function of cortical depth. Density of neurons changes depending on the cortical depth. Each cortical layer is comprised of a different distribution of neuronal cell. The cytoarchitectonic subdivision of cortical layers can be used to describe the organization of the cortical circuitry, sensory-evoked signal flow, or cortical functions. Glio-vascular profiling of the cortical layers can help in quantifying drug discovery. The motivation is to use the above discussed structural differences to delineate cortical layers for a comprehensive whole tissue based phenotypical profiling and understanding the functionality of cortical regions.

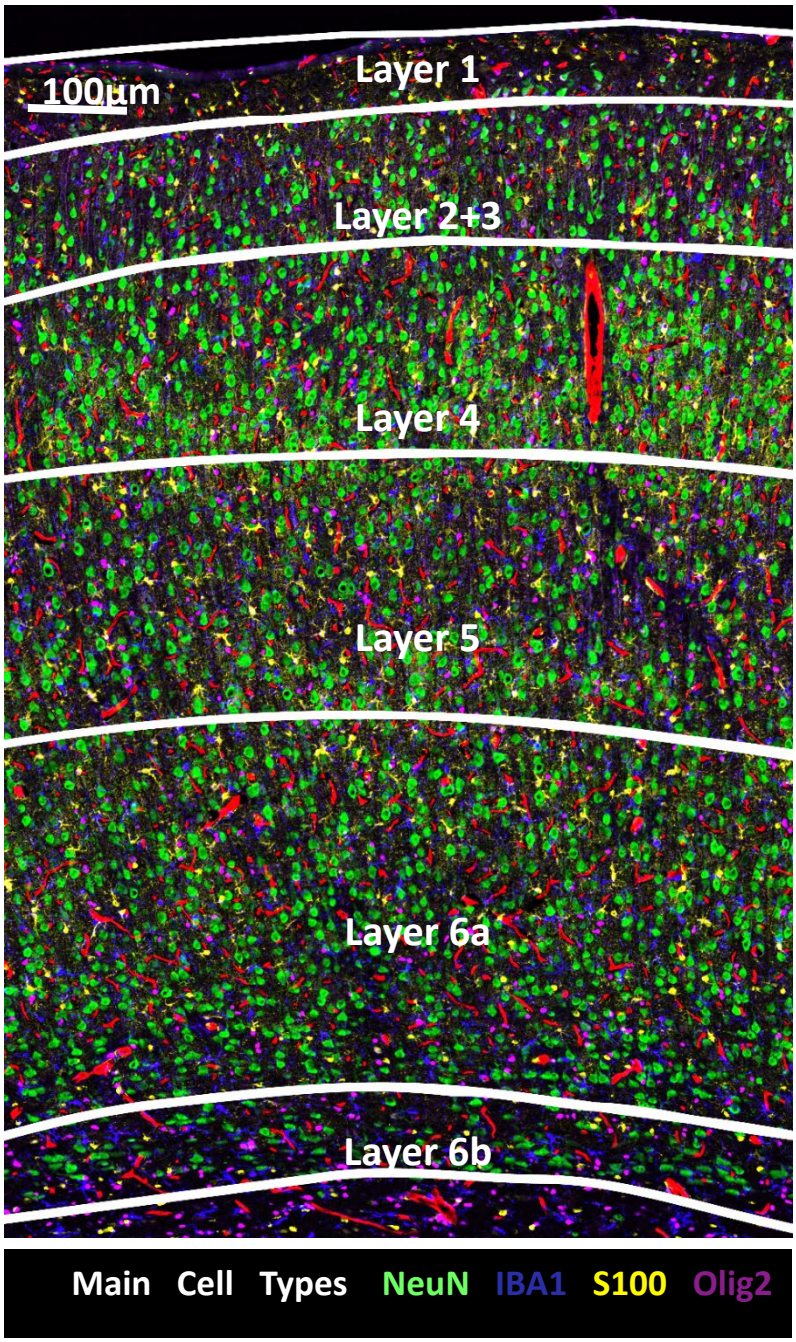


Figure 1-14. Cortical Layers delineated manually by biologists as expert delineation.

## 1.5 Objectives

The objective of this thesis is to develop a method to delineate the laminar boundaries in the cortex of the brain based on the characteristics of the neurons belonging to these cortical layers. Specifically, this thesis focuses on three goals. The first goal is to develop an objective and automated multiplex imaging-based method for delineation of cortical layers in the whole brain sections even without the benefit of layer-specific molecular markers. This is an advance over labor-intensive current methods where layers are visually delineated by biologists. The second goal is to perform a comprehensive multiplex method for data-driven spatial statistical comparison of brain regions of healthy and injured brains advance over the current approach of visual qualitative inspection from Nissl stained images. The final goal is to conduct comprehensive glio-vascular and neuronal profiling of cytoarchitectonic layering of cortical neurons across multiple rat brains over the current methods that only profile the neurons.

We additionally develop active learning framework for implementing classification with Convolutional Neural Networks in the case where labels are difficult to obtain.

This dissertation is formulated as follows:

CHAPTER 2 discusses the challenges faced in cortical layer delineations and the motivation behind our algorithm.

CHAPTER 3 proposes an objective and automated approach for cortical layer delineation and validation strategies.

CHAPTER 4 discusses cortical layer profiling approaches for the three datasets.

CHAPTER 5 proposes whole cell morphological segmentation methods for cytoarchitectonic layering.

CHAPTER 6 processes the active learning approach for breast cancer classification using convolutional neural networks.

# CHAPTER 2 CHALLENGES IN CORTICAL LAYER DELINEATION

## 2.1 Data Heterogeneity Challenges

The brain cortex is heterogeneous at multiple levels making cortical layer delineation a very complex problem. As seen in Figure 2-1, the close-up of different cortical layers show that the distribution of major cell-types looks very similar in most layers. Layer 6b visually looks like layer 1 in terms of neuron size and density, while the other four layers look very similar to each other. Thus, cortical delineation using visual cellular distribution is a challenging problem to deal with.

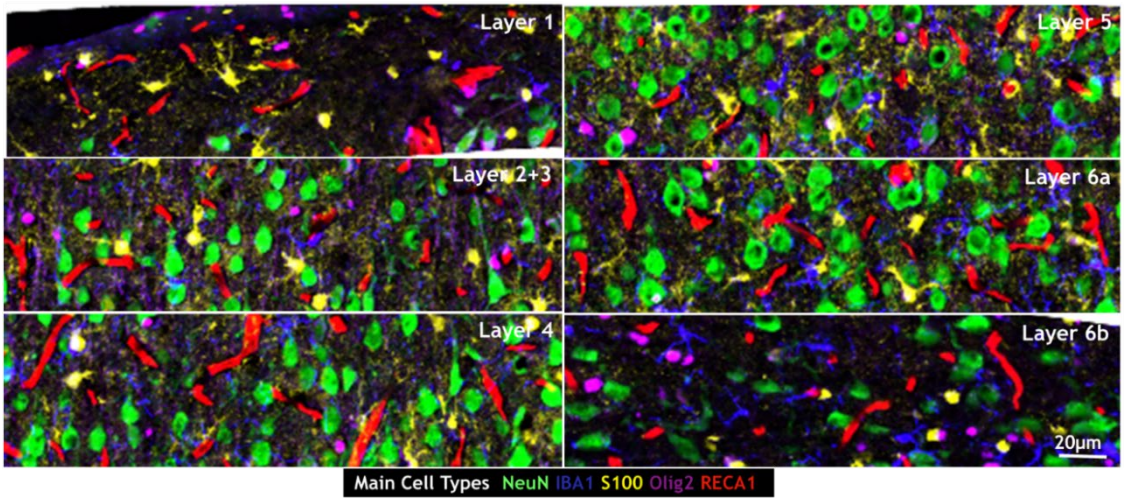


Figure 2-1. Sample close-up highlighting different cortical layers.

Secondly, for the multiplex imaging, the traditionally used molecular markers are not differently expressed in any cortical layer, or layer-specific markers (as seen in Figure 2-2). Layer-specific markers are the molecular markers are expressed in specific cortical layer neurons.

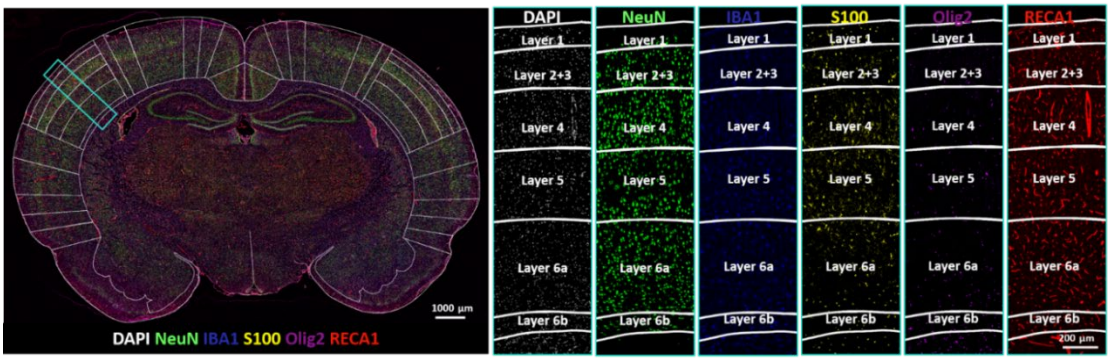


Figure 2-2. Major cell phenotype channels with cortical layer delineation.

Thirdly, there is high variability throughout the cortex, within and between different cortical regions. Visual analysis of two regions in primary somatosensory cortex barrel field (S1BF) in Figure 2-3, we see that layer thickness for layer 1 and layer 4. The cellular distribution for layers 4, 5, and 6A indicates high heterogeneity. The cell morphology in layer 6a asymmetric, the cells are pyramidal shaped in Figure 2-3 (B1) and rounded in Figure 2-3 (B2).

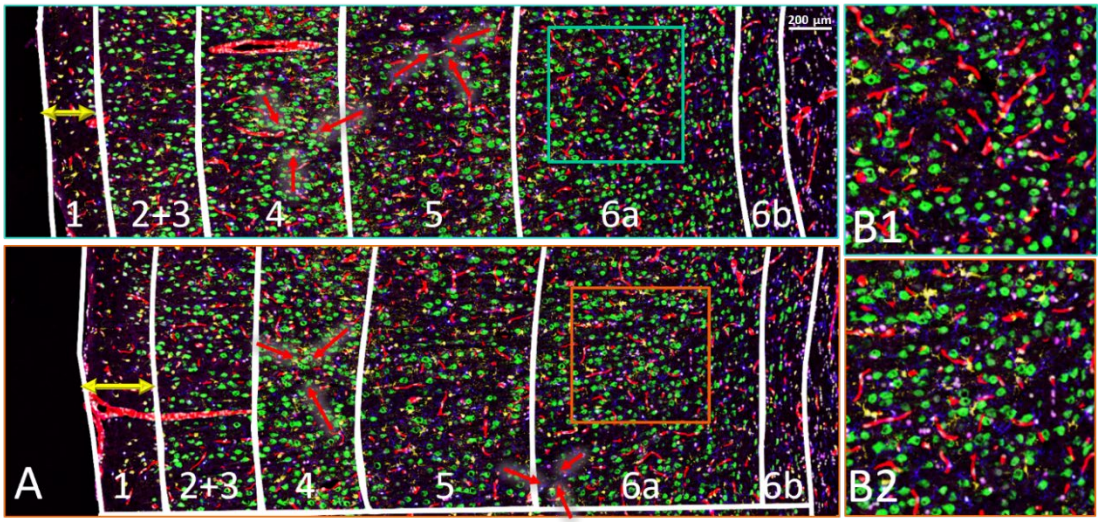


Figure 2-3. (A) Two regions from cortical layer 6a of primary somatosensory cortex barrel field. (B1) Magnified region of layer 6 A from region 1. (B2) Magnified region of layer 6A from region 2.

Fourthly, the thickness of layers varies throughout the cortex (see Figure 2-4). Each layer in the cortex delineated has thickness varying with the spatial location. The morphology and spatial distribution of the cells is inconsistent across different regions in the cortex (see Figure 2-5). High neuronal density regions in primary motor cortex at higher cortical depth compared for that in secondary somatosensory cortex, while no comparative density region is found in perihinial cortex.

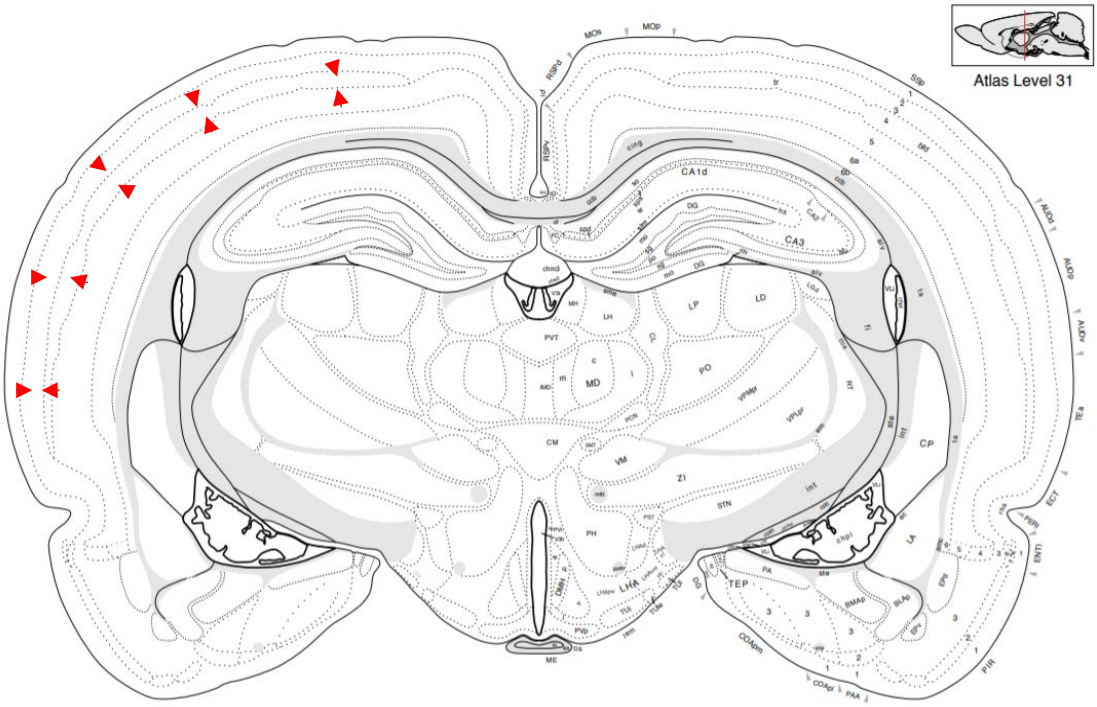


Figure 2-4. The thickness of layers varies throughout the cortex. Layer 4 highlighted from the Swanson's Atlas.

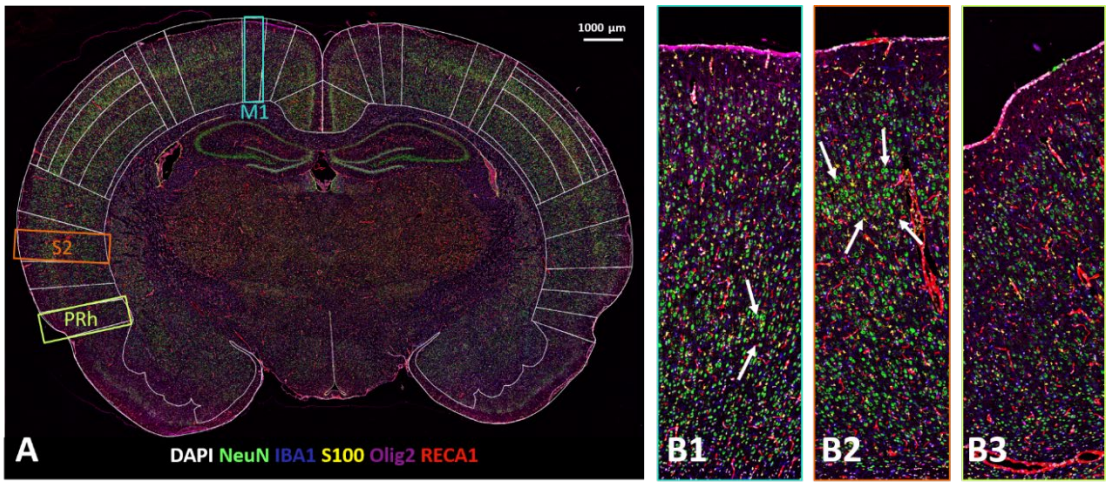


Figure 2-5. (A) The cellular distribution for different cortical regions, namely primary motor cortex (M1), secondary somatosensory cortex (S2), perihinial cortex (PRh) in B1, B2 and B3 respectively. High neuronal density regions illustrated by arrows.

Finally, since brain is a very complex organ, the relative location and composition of structures varies with age, gender, and other development factors. Hence for different animals the cortical structure will be unique to it. Our algorithm should be able to handle these challenges in order to ensure its success on multiple datasets.

## 2.2 Literature Survey

Henver et al. [9] studied neonatal mouse brain during development by analyzing layer-specific markers in the parietal cortex for neonatal, embryonic, and post-natal cortex. This work was later extended to studying malformations of cortical development in human neocortex [10]. Tosun et al. [11] used fuzzy segmentation based automatic reconstruction of inner, central and pial surface for human brain MRI images. Eickhoff et al. [12] developed a toolbox for probabilistic cytoarchitectonic brain mapping of the human brain into cortical areas using functional imaging and histological staining. Layer-specific molecular markers have been used to analyze interneurons and projection neurons in cortical layers of rat neocortex in Molyneaux et al. [13]. This work was later extended to

neonatal mouse to study the subpopulations of projection neurons for different cortical layers and areas [14]. Yu et al. [15] analyzed the barrel cortex layers to study mechanism of plasticity in a model of peripheral deprivation of sensory input from the whiskers in 4- to 6-week-old rats using manual delineation. Kurth et al. [16] performed delineation for cortical layers for human brain using co-registered histological and MRI imaging. Narayana et al. [17] used inhibitory and exhibitory neurons-based density profiles for manually delineating rat brain primary somatosensory cortex. Swanson et al. [4] delineated the cortical layers for 71 coronal sections using Nissl stains. Zilles and Palomero visually delineated cortical layers for multiple regions in the human brain using autoradiography images [18].

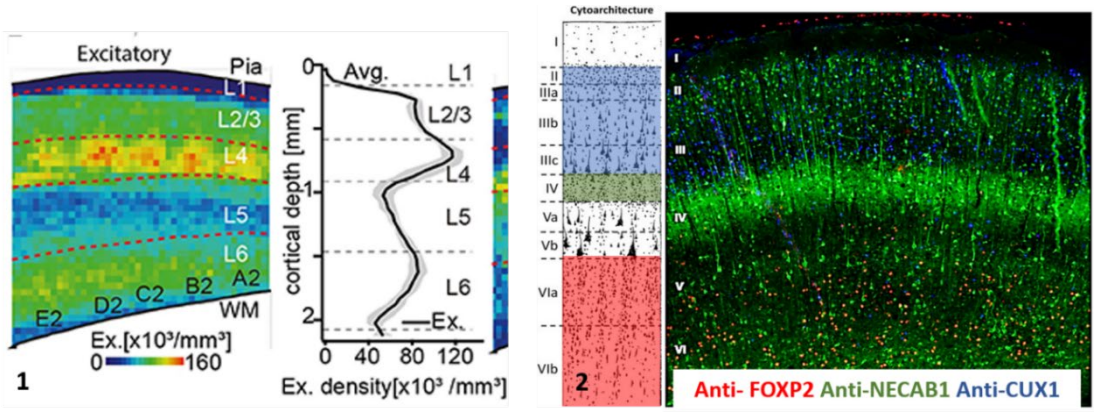


Figure 2-6. (1) Manual delineation method using excitatory neuronal density profile [17]. (2) Laminar structure of cerebral cortex of rat shown by layer-specific markers [19].

As discussed above, currently cortical layer delineation is mostly done by two methods (see Figure 2-6) mentioned below:

1. Manual Delineation: Biologists visually analyze the morphological and spatial properties of cortical neurons and manually delineate the cortical layers. This is a very

labor-intensive approach and hence is generally performed for specific regions as per the need of the study.

2. Layer-specific Markers: Markers expressed in neurons belonging to a specific cortical layer are used to delineate. Layer-specific sometimes bleed through into the other layers, making layer delineation difficult. Layer-specific molecular markers for rat brains is a fairly new subject.

Both of these methods do not provide any kind of validation or profiling for the layer delineation and are purely up to biologist's discretion.

### 2.3 Performance Evaluation Challenges

Most available atlases do not delineate cortical layers throughout the cortex. Atlas is unique to every brain; hence no objective ground truth is easily available for cortical layers.

Our proposed algorithm works on large whole-brain multiplex images which are 16-bit images of size 43054×29398 pixels, approximate size 2.5 gigabytes. The cortex consists of around 80,000 cells out of which around 40,000 are neurons. Evaluating the performance for the whole cortex will require a manual delineation for the whole dataset, which will be labor intensive.

Lastly, in order to validate the accuracy of the cluster analysis delineation of the laminar structure of the cortex, two immunohistopathological cellular markers were chosen that have been found to be highly localized to different cortical layers. For layer 4, neuronal calcium-binding protein 1 (NECAB1) was selected because it is highly and uniformly expressed in layer 4 pyramidal neurons in the cerebral cortex [20, 21]. Forkhead box

protein PE (Foxp2) was selected for its high specificity to glutamatergic neurons with robust expression predominantly in layer 6 [22, 23].

FOXP-1 marks layer 6 neurons and NECAB-1 marks mainly layer 4 neurons along with layer 2 and 3 neurons. We will be hence proposing validation methods to successfully establish the superiority of our algorithm to the current state of the art.

# CHAPTER 3 AUTOMATED CORTICAL LAYER DELINEATION

## 3.1 Feature Engineering and Extraction

Neuronal density, cortical depth, shape, and diameter of neuronal somata are the most common features which vary across different layers in the cortex. We use the NeuN channel after registration and image correction [7]. Neurons are detected using multiplex classification [7]. Given $N$ neurons in the whole brain cortex, we extract the features as $\boldsymbol{x}$ as

$$x = \{x_1, x_2, .. x_N\} \tag{1}$$

$$\text{where } x_i = \begin{bmatrix} x_{i1} \\ x_{i2} \\ x_{i3} \\ x_{i4} \\ x_{i5} \end{bmatrix} \text{ for } i \in \{1,2, \dots, N\}. \tag{2}$$

The features are described as below.

$x_{i1}$: Neuronal density for neuron $i$.

$x_{i2}$ : Cortical depth for neuron $i$.

$x_{i3}$: Orientation of neuron $i$ relative to the pial surface.

$x_{i4}$: Diameter of neuron $i$.

$x_{i5}$: Area of neuron $i$.

These features (see Figure 3-1) for the neuronal soma are extracted using morphological segmentation which will be discussed in chapter 5.

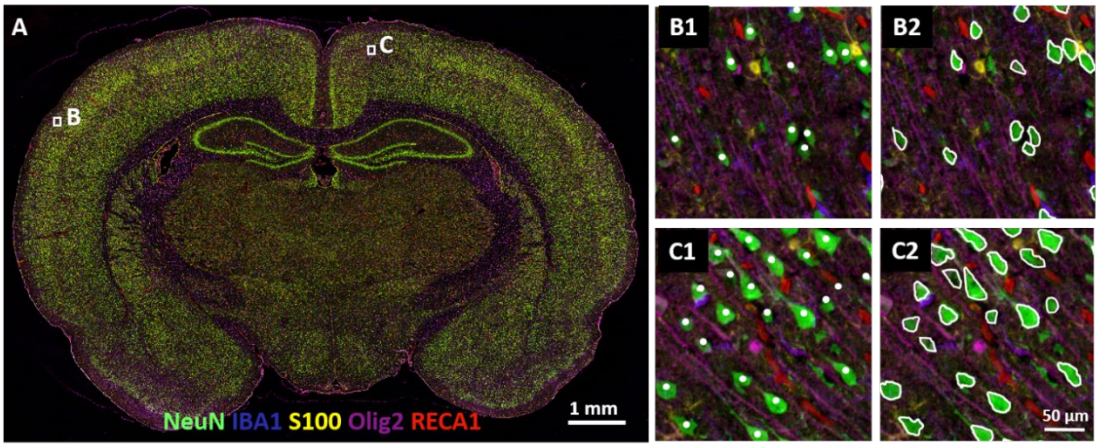


Figure 3-1. The neuronal feature extraction pipeline uses (A) NeuN channel after registration and image correction. (B1-B2) Neurons are detected using multiplex classification. (C1-C2) Somata marked for these neurons using morphological masking.

## 3.2 Neuronal Clustering

Using the features discussed earlier, we perform soft assignment of neurons into clusters. We perform clustering only on the subset of neurons with high quality features and allocate clusters to the remaining neurons later.

### 3.2.1. Dirichlet Process Mixture Model (DPMM) based Clustering

Dirichlet Process Mixture Model [24] is a non-parametric model for clustering, where the number of clusters is learned from the data. The parameters of each mixture component are generated by a Dirichlet Process (DP) parameterized by a base measure $G_o$ and concentration parameter $\alpha$ as

$$G \sim DP(\alpha, G_o). \quad (3)$$

The component with label $z_i$ from the Dirichlet process can be represented as

$$\theta_{z_i} \sim G. \tag{4}$$

Considering a data point $x_i$, drawn independently from component with label $z_i$ as

$$x_i|\theta_{z_i} \sim p\left(x_i\middle|\theta_{z_i}\right). \tag{5}$$

And the DPMM can be represented as

$$G = \sum_{k=1}^{\infty} \pi_k \delta_{\theta_k}, \tag{6}$$

where $\theta_k$ are parameters of the $k^{th}$ component, and $\delta_{\theta_k}$ is an indicator function centered at $\theta_k$. $\pi_k \epsilon [0,1]$ are the mixing proportions of the k$^{th}$ component, which are produced as

$$v_k \sim B(1, \alpha) \tag{7}$$

and

$$\pi_k = v_k \prod_{l=1}^{k-1}(1 - v_l), k = 1, 2, \ldots \infty, \tag{8}$$

where $B$ is the Beta distribution. The component parameters are represented as

$$\theta_k = \{\mu_k, R_k\}, \tag{9}$$

where $\mu_k$ and $R_k$ are the mean vector and precision matrix for the $k^{th}$ component. Using DPMM with Gaussian mixtures, the likelihood function for sample $x$ belonging to component k is evaluated as

$$p(x|\pi_k, \mu_k, R_k) = \sum_{k=1}^{\infty} \pi_k \, N(x|\mu_k, R_k^{-1}). \tag{10}$$

DPMM is a generative model that generates observations according to the following steps.

1. For k=1, 2, …, ∞
    a. Draw $v_k \sim B(1, \alpha)$.
    b. Compute $\pi_k = v_k \prod_{l=1}^{k-1}(1 - v_l)$.
2. For each component k=1, 2, …, ∞
    a. Draw precision $R_k \sim W(B_o, v_o)$.
    b. Draw mean $\mu_k \sim N(\mu_o, (r_o, R_k)^{-1})$.
3. For each observation $i = 1, 2, \ldots, N$
    a. Draw component assignment $z_i \sim Cat(\pi)$.
    b. Draw $x_i \sim N(\mu_{z_i}, R_{z_i})$.

During inference given data $X$, the goal is to infer the latent variables $Z = \{z_1, z_2, .., z_N\}$ and parameters $V = \{v_1, v_2, \ldots\}$ and $\theta = \{\theta_1, \theta_2, \ldots\}$. Variational inference methods [25, 26] are used inference by approximating the posterior $p(V, \theta, Z|X)$ by $q(V, \theta, Z)$ by minimizing the KL (Kullback-Leiber) divergence between them. The latent variables and parameters of the variational distribution are assumed to be mutually independent and the upper limit on number of components is set to $T$ as

$$q(V, \theta, Z) = [\prod_t^T q(v_t)][\prod_k^T q(\theta_k)][\prod_i^N q(z_i)]. \quad (11)$$

The objective function is the KL divergence between posterior and variational distribution and is calculated as

$$D_{KL}[q(V, \theta, Z)||p(V, \theta, Z|X)]$$

$$= \sum_z \iint q(V, \theta, Z) \log \frac{q(V, \theta, Z)}{p(V, \theta, Z|X)} dV\, d\theta$$

$$= -\sum_z \iint q(V, \theta, Z) \log \frac{p(V, \theta, Z)/p(X)}{q(V, \theta, Z)} dV\, d\theta$$

$$= -\sum_z \iint q(V,\theta,Z) \log \frac{p(V,\theta,Z)}{q(V,\theta,Z)} dV\, d\theta + \log p(X) = F + \log p(X). \quad (12)$$

To minimize the KL divergence, we need to minimize the free energy term, $F$ which can be simplified as

$$F = -\sum_z \iint q(V,\theta,Z) \log \frac{p(V,\theta,Z)}{q(V,\theta,Z)} dV\, d\theta = E\left[\log \frac{q(V,\theta,Z)}{p(V,\theta,Z)}\right]_{q(V,\theta,Z)}$$

$$= \sum_{k=1}^{T} E\left[\log \frac{q(\theta_k)}{p(\theta_k)}\right]_{q(\theta_k)} + \sum_{k=1}^{T} E\left[\log \frac{q(v_k)}{p(v_k)}\right]_{q(v_k)} +$$

$$\sum_{i=1}^{N} E\left[\log \frac{q(z_i)}{p(x_i|z_i,\theta)p(z_i|V)}\right]_{q(z_i,V,\theta)}. \quad (13)$$

F can be minimized using coordinate ascent variational inference (CAVI) algorithm [20].

### 3.2.2. Active Informed DPMM (AIDPMM) based Clustering

We propose an active learning-based clustering framework for cortical delineation problem since the cortex is very heterogeneous within and across different layers. The idea is to improve the clustering by integrating known spatial information from the cortex since the cortex is very heterogeneous within and across different layers. There has been work done using DPMM [27] to impose constraints on clustering if two data points in the cluster should belong to same or different clusters. AIDPMM similarly uses two types of grouping information, must-link, $ML$ and cannot-link, $CL$ for the neuronal data. The neurons with must-link should be belong to the same clusters, while neurons with cannot-link should belong to different clusters.

Given, $L$ total number of groups as per the must-link, ML and cannot-link information, CL, $X_l$ are the neurons on which any linking is imposed, $Z_l$ is the corresponding component assignment for the $l^{th}$ linked group. The modified variational distribution is as

$$q(V, \theta, Z) = [\prod_t^T q(v_t)][\prod_k^T q(\theta_k)][\prod_{l=1}^L q(Z_l|ML, CL)]. \quad (14)$$

The objective function for C-DPMM is

$$F = \sum_{k=1}^T E\left[\log \frac{q(\theta_k)}{p(\theta_k)}\right]_{q(\theta_k)} + \sum_{k=1}^T E\left[\log \frac{q(v_k)}{p(v_k)}\right]_{q(v_k)} + \sum_{l=1}^L E\left[\log \frac{q(Z_l)}{p(X_l|Z_l, \theta)p(Z_l|V)}\right]_{q(Z_l, V, \theta)}. \quad (15)$$

This objective function can be simplified as

$$F = \sum_{k=1}^T E\left[\log \frac{q(\theta_k)}{p(\theta_k)}\right]_{q(\theta_k)} + \sum_{k=1}^T E\left[\log \frac{q(v_k)}{p(v_k)}\right]_{q(v_k)} + \sum_{l=1}^L \log \sum_{k=1}^T \exp(S_{l,k}) \quad (16)$$

where

$$S_{l,k} = E[\log\ p(X_l|\theta_k)]_{q(\theta_k)} + E[\log p(Z_l = k|V)]_{q(V)}, \quad (17)$$

$$p(X_l|\theta_k) = \prod_{i=1}^{N_l} p(x_i|\mu_k, R_k), \quad (18)$$

and

$$p(Z_l = k|V) = \prod_{i=1}^{N_l} p(z_i = k|V) = (v_k \prod_{j=1}^{k-1}(1 - v_j))^{N_l}. \quad (19)$$

The free energy, F is minimized using the CAVI algorithm [28] until it converges. The final clustering label obtained for each neuron $x_k$ is given by $argmax_k(q(Z = k))$.

AIDPMM clustering initially performs DPMM clustering in the absence of any grouping information. Based on the clusters determined initially (Figure 3-2), the user examines the obtained neuron clusters and decided action, namely “freeze”, “keep” or

"split" for each cluster. This allows us to organically capture intra-layer heterogeneity. Hence, there might be clusters that need to be split down to get meaningful "sublayers". A sublayer being a cluster which consists of neurons belonging exclusively to one layer. Based on the action chosen for every cluster by the user, additional information is obtained from the user. The clusters allocated freeze are separated from the active clustering dataset for the following iterations so that the cluster labels stay the same. In the example shown in Figure 3-2, clusters B2 and B4 are sublayers for layer 6 and layer 2+3 respectively, hence these are kept. This means they are removed from the training neuron dataset. The clusters B1 and B3 are selected for splitting. We calculate uncertainty scores for neurons from these clusters similar to in [29] as

$$U(a) = H\big(nn(\mu)\big) + \frac{vl(ml(a))+vl\big(cl(a)\big)}{1+ml(a)+cl(a)}. \tag{20}$$

where $H(nn(\mu))$ is the entropy of cluster labels of $\mu$ neighboring neurons, $ml(a)$ and $cl(a)$ are the number of must-links and cannot-links associated with neuron $a$, $vl(ml(a))$ and $vl(cl(a))$ are the violated must-links and cannot-links associated with neuron $a$. Uncertainty score is high if either must-link and cannot-link grouping information is violated, or neighboring neurons belong to different clusters. We select the $r$ neurons with highest uncertainty scores from each cluster. We display the neurons with high uncertainty scores for cluster B1 in Figure 3-3. As we can see, most of the neurons on the boundaries of the cluster have high uncertainty, as the inner neurons in this cluster clearly belong to layer 5.

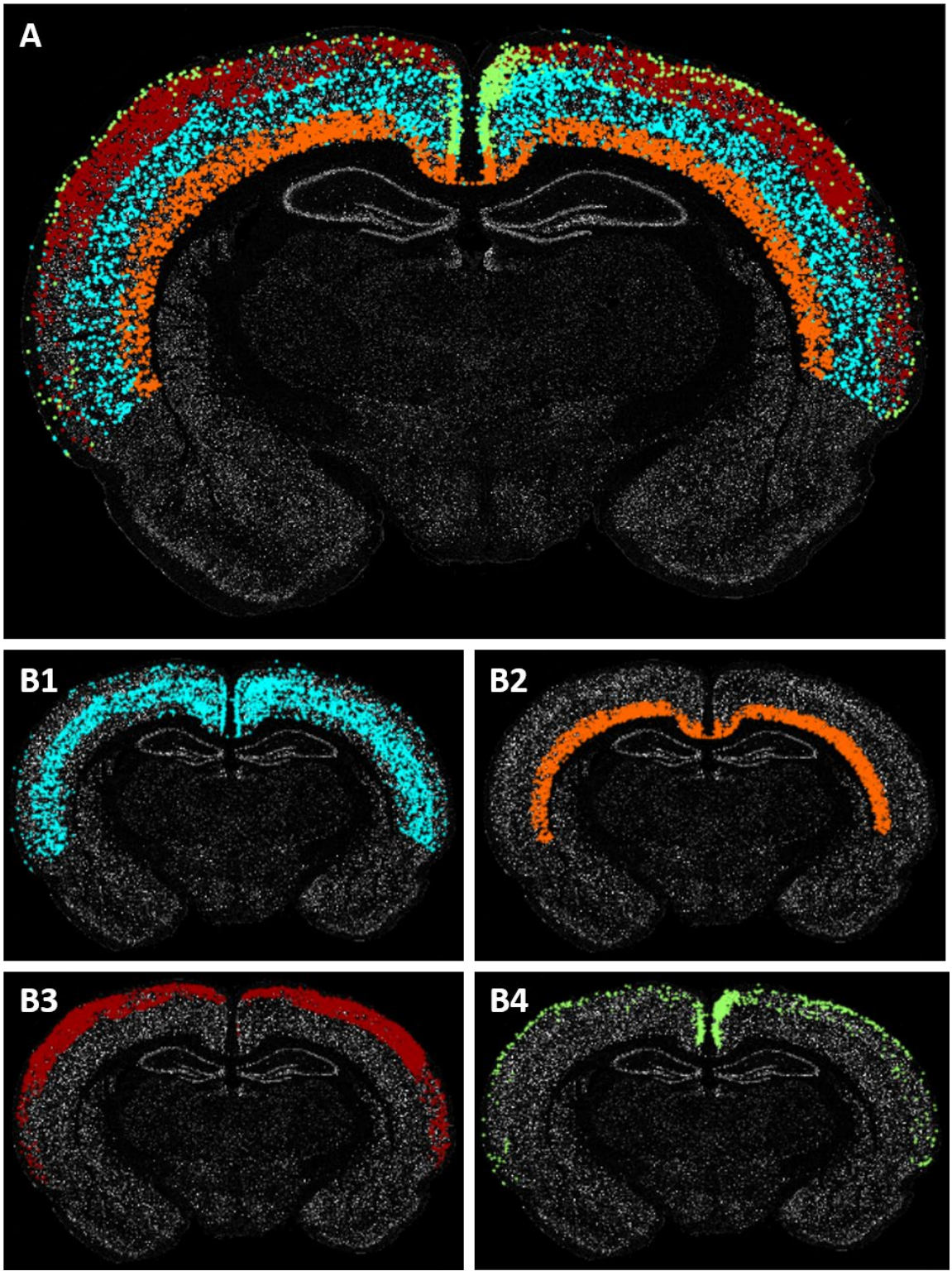


Figure 3-2. (A) Initially found clusters using AIDPMM (B1-B4) Individual clusters depicted.

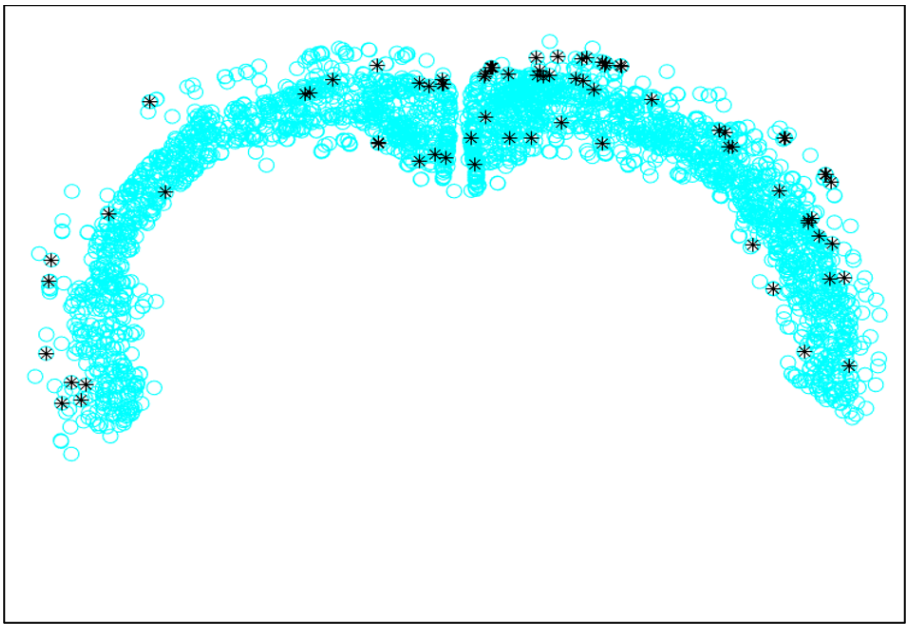

Figure 3-3. Neurons with high uncertainty scores from the cluster selected for splitting.

All the selected high uncertainty neurons from the clusters selected for splitting are divided into two sets, namely set $A$ and $B$. Set $A$ consists of neurons belonging to the same cluster, while set $B$ consists of neurons belonging to different clusters, as per the current clustering results. For a pair of neurons $(a, b) \in A : label(a) = label(b)$, we want to select it if they are located far apart and have high uncertainty. For a pair of neurons $(a, b) \in B: label(a) \neq label(b)$, we want to select the pair if they have high uncertainty and they are close to each other. This is because most neurons close to each other belong to the same cortical layer. Hence, we define a label value term, $w$ for each pair $(a, b)$ belonging to set $A$ and $B$ as

$$(a, b) \in A: w(a, b) = \frac{d_{ab}(1+U(a))(1+U(b))}{(1+ml(a)+cl(a))(1+ml(b)+cl(b))} \tag{21}$$

and

$$(a, b) \in B: w(a, b) = \frac{d_{ab}(1+ml(a)+cl(a))(1+ml(b)+cl(b))}{(1+U(a))(1+U(b))} \tag{22}$$

where $d_{ab}$ is the Euclidean distance between neurons $a$and $b$, $ml(a)$ and $cl(a)$ are the number of must-links and cannot-links associated with neuron $a$, $U(a)$ is the uncertainty score for neuron $a$.

Hence, for set $A$, we query the user for the neuron pairs with high label values and for set $B$, we query the user for neurons pairs with low label values. We use top $Q/2$ highest label value pairs from $A$ and bottom $Q/2$ lowest label value pairs from $B$. These pairs should be non-overlapping to get more information diversity. The pairs selected are shown to the user (Figure 3-4), who provide the linking type (1: for must link, 0: for cannot-link, -1: not sure) for that pair.

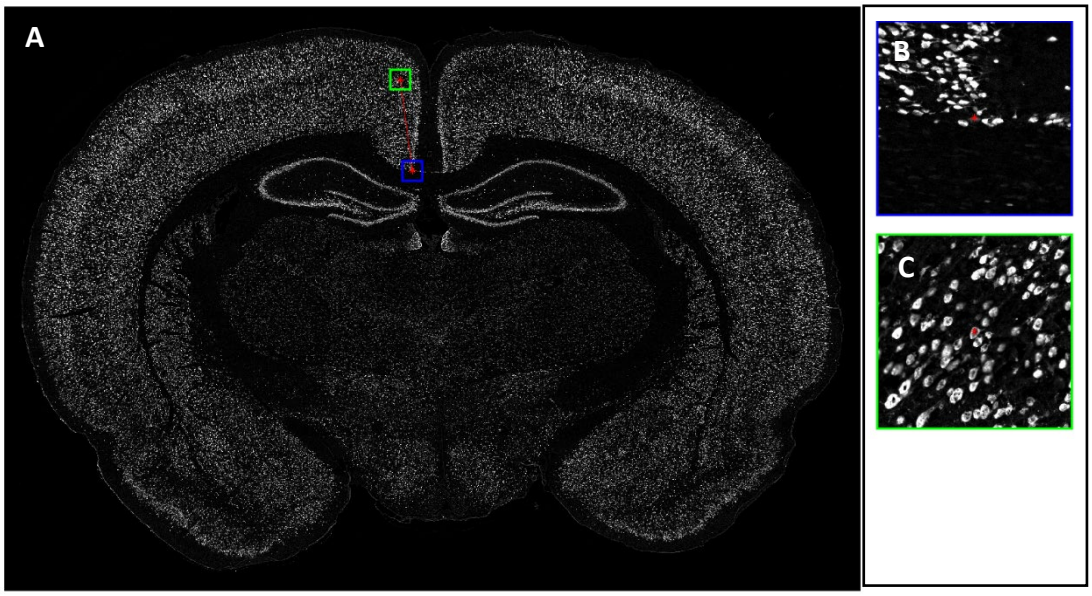


Figure 3-4. (A)Pair selected for query as per active learning, (B) Zoomed in version for neuron 1, (C) Zoomed in version for neuron 2.

These query inputs (Figure 3-5) are used to update $ML$ and $CL$ every iteration for subsequent clustering. We perform clustering until we exhaust the information budget or there are no clusters to be split further.

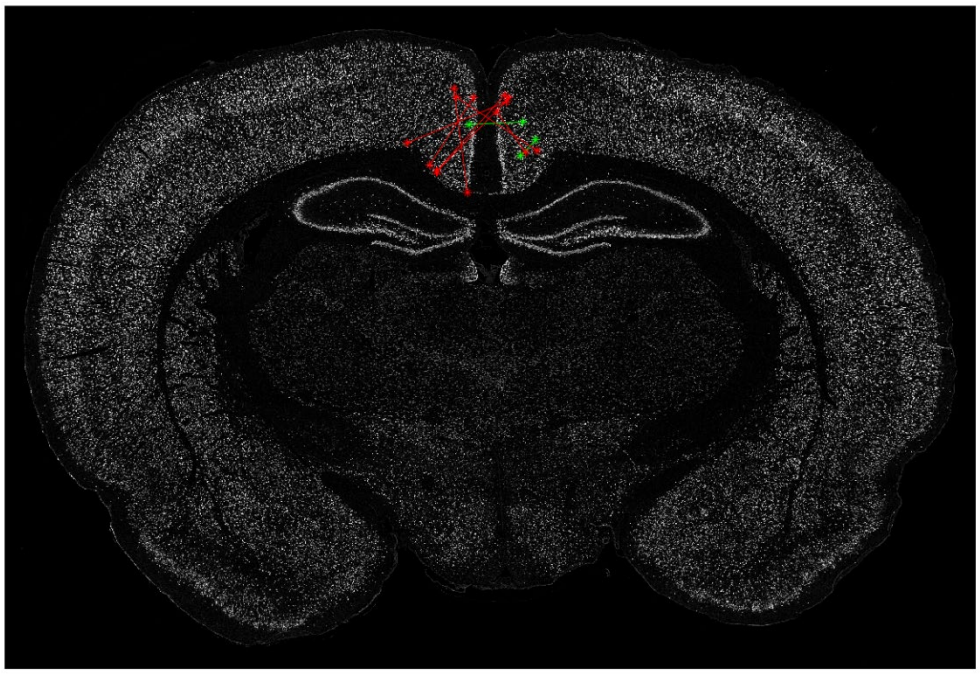

Figure 3-5. Must-links neuronal pairs (green) and cannot-link neuronal pairs (red) marked.

Once we finish the clustering, we merge the clusters (Figure 3-6) into meaningful layers as per user's supervision (Figure 3-7). The AIDPMM algorithm is summarized in (Algorithm 1).

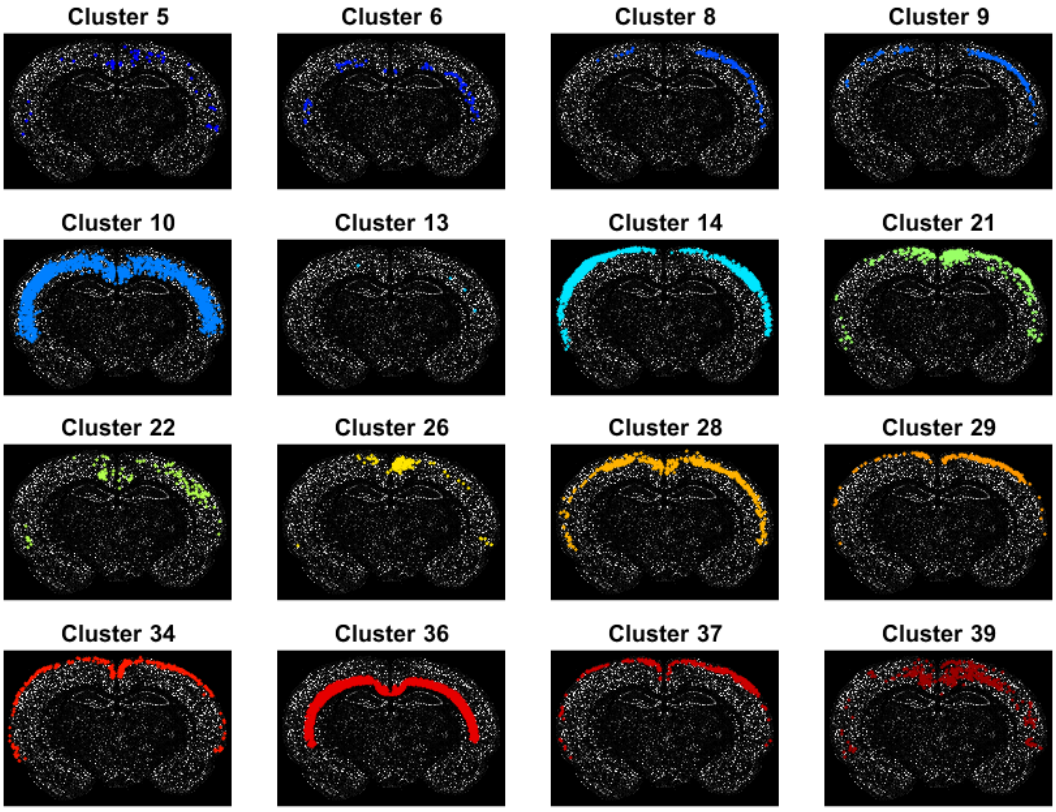


Figure 3-6. Final clusters obtained through AIDPMM.

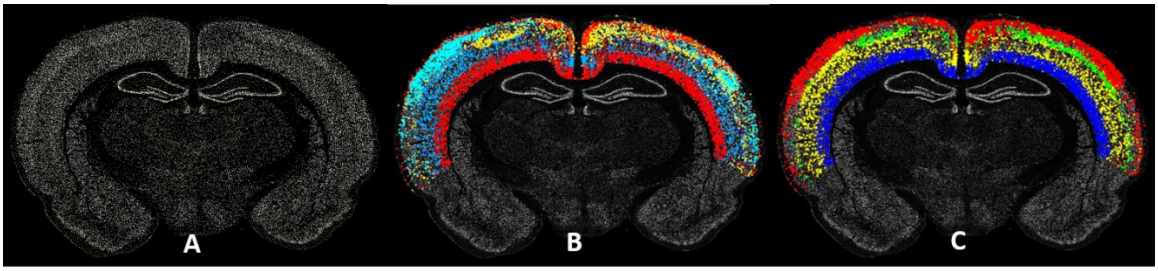


Figure 3-7. (A) NeuN channel input used for feature extraction, (B) 16 clusters obtained from AIDPMM, (C) Cluster merging to layer result (Layer 2+3 in red, Layer 4 in green, Layer 5 in yellow, Layer 6 in blue).

Algorithm 1: Active Informed DPMM (AIDPMM) based Clustering

Input: Neurons, $(c_i, x_i)\ for\ i = 1, 2, \ldots N$

Output: Variational distribution, $q(Z)$

1. $\boldsymbol{ML} = \emptyset$ , $\boldsymbol{CL} = \emptyset$
2. $\boldsymbol{q(Z) = AIDPMM(x, ML, CL)}$
3. Cluster label for $\boldsymbol{x_i}$, $\boldsymbol{l(x_i) = argmax\ q(Z_i = k|x_i)}$
4. Select clusters $\boldsymbol{K}$ for freezing
5. $\boldsymbol{x_i \leftarrow x_i - x_j \forall\ l(x_j) \in K}$
6. Select clusters $\boldsymbol{S}$ for splitting
7. Evaluate $\boldsymbol{U}$ for all the neurons from the clusters $\boldsymbol{S}$
8. Create all possible pairs $(\boldsymbol{a, b})$ with top-$\alpha$ neurons from each split cluster and divide it into set $\boldsymbol{A}$ and $\boldsymbol{B}$ such that

$$(\boldsymbol{a, b}) \in \boldsymbol{A}: \boldsymbol{l(a) = l(b)}$$

$$(\boldsymbol{a, b}) \in \boldsymbol{B}: \boldsymbol{l(a) \neq l(b)}$$

9. Calculate label value, $\boldsymbol{w}$ as

$$\forall(\boldsymbol{a, b}) \in \boldsymbol{A}: \boldsymbol{w(a, b)} = \frac{\boldsymbol{d_{ab}}\big(\boldsymbol{1 + U(a)}\big)\big(\boldsymbol{1 + U(b)}\big)}{\big(\boldsymbol{1 + ml(a) + cl(a)}\big)\big(\boldsymbol{1 + ml(b) + cl(b)}\big)}$$

$$\forall(\boldsymbol{a, b}) \in \boldsymbol{B}: \boldsymbol{w(a, b)} = \frac{\boldsymbol{d_{ab}(1 + ml(a) + cl(a))(1 + ml(b) + cl(b))}}{\boldsymbol{(1 + U(a))(1 + U(b))}}$$

10. Highest $\boldsymbol{Q/2}$ label value pairs selected from A and lowest $\boldsymbol{Q/2}$ label value pairs selected from $\boldsymbol{B}$ for user annotation
11. Update $\boldsymbol{ML, CL}$ as per 10
12. Repeat 2 to 12 until performance convergence or $\{\boldsymbol{x}\} = \emptyset$

AIDPMM algorithm only analyzes the neurons with high quality features available in order to generate a reliable initial layer delineation. This creates the need to account for the remaining neurons. We additionally allocate layers to the remaining neurons by interpolation for visualization (Figure 3-8). The idea is to allocate same layers to neurons close to each other and at similar cortical depth. This is done by weighted voting of the training dataset layer labels, as mentioned in algorithm 1.

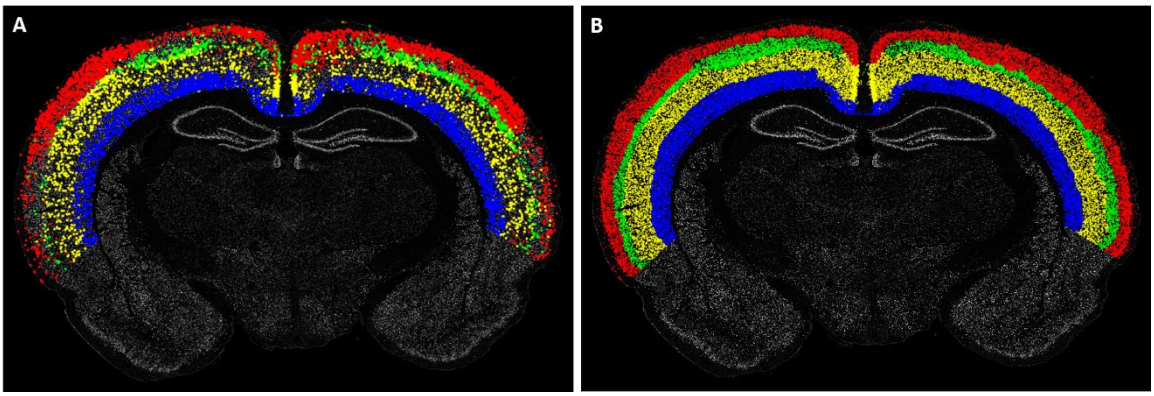


Figure 3-8. (A) Cortical Layer Delineation on the training dataset, (B) Cortical Layer Delineation extended to all detected neurons through interpolation.

For each unlabeled neuron, find $m$ nearest neighboring neurons$(m = 20)$ . The layer labels of these neurons are counted with weights inverse to the difference in the cortical depth from that of unlabeled neuron. This voting approach helps in the cases where neighboring neurons belong to different layers. The unlabeled neuron hence is allocated to the layer with maximum votes.

Algorithm 2: Layer Interpolation Algorithm

**Input**: Labeled Neuron Set, $\mathbf{A} = \{\boldsymbol{x_i}\}_{\boldsymbol{i=1}}^{\boldsymbol{N}}$;

Layer Labels, $\boldsymbol{L_A} = \{\boldsymbol{l_{x_i}}\}_{\boldsymbol{i=1}}^{\boldsymbol{N}}\ \boldsymbol{l} \in \{\mathbf{0}, \mathbf{1}, \mathbf{2}, \mathbf{3}\}$ ;

Cortical depth, $\boldsymbol{D} = \{\boldsymbol{d_i}\}_{\boldsymbol{i=1}}^{\boldsymbol{M}}$; Remaining Neuron Set , $\boldsymbol{B} = \{\boldsymbol{x_i}\}_{\boldsymbol{i=N+1}}^{\boldsymbol{M}}$

**Output**: Layer Labels, $\boldsymbol{L_B} = \{\boldsymbol{l_{x_i}}\}_{\boldsymbol{i=N+1}}^{\boldsymbol{M}}$

1. For every neuron $\mathbf{x_i} \in \mathbf{B}$, find $\mathbf{k}$ nearest neighbors, $\mathbf{nn_k}$ from set $\mathbf{A}$
2. Layer labels of the neighbors: $\left\{\boldsymbol{l_{x_j}}\right\}\ \forall \boldsymbol{j} \in \boldsymbol{nn_k}$
3. Votes for each neighbor: $\boldsymbol{v_j} = \frac{\mathbf{1}}{|\boldsymbol{d_i} - \boldsymbol{d_j}|}\ \forall\ \boldsymbol{j} \in \boldsymbol{nn_k}$
4. Votes for each layer, $\boldsymbol{l}$:

$$\boldsymbol{V(l)} = \sum_{\boldsymbol{j} \in \boldsymbol{nn_k}} \boldsymbol{v_j I(\ l_{x_j})}\ \forall \boldsymbol{l} \in \{\mathbf{0}, \mathbf{1}, \mathbf{2}, \mathbf{3}\}$$

5. Label for neuron $\boldsymbol{x_i}$, $\boldsymbol{l(x_i)} = \boldsymbol{argmax(V(l))}$

## 3.3 Results and Analysis

We implement the previously discussed AIDPMM algorithm on 15 brains. Below is layer delineation shown for 50-plex healthy serial section brains (Figure 3-9) and mTBI brains (Figure 3-10).

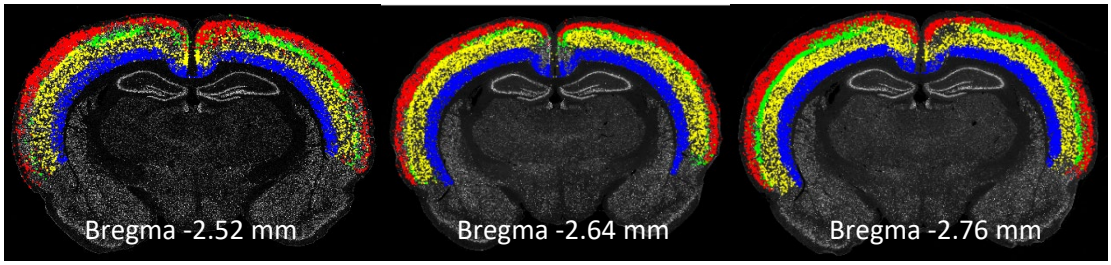


Figure 3-9. Layers (2+3 in red, 4 in green, 5 in yellow, 6 in blue) delineated using AIDPMM for 50-plex serial brain sections.

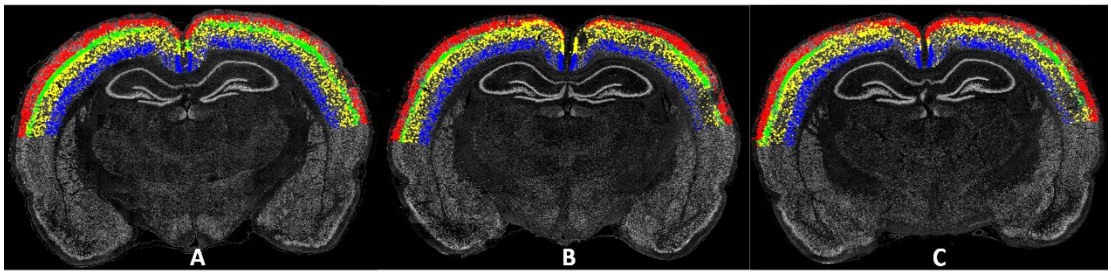


Figure 3-10. Layers (2+3 in red, 4 in green, 5 in yellow, 6 in blue) delineated using AIDPMM for (A) Healthy, (B) Injured and (C) Drug-treated brain sections.

### 3.3.1. Confidence Score Maps

We illustrate the confidence score maps for each of the layers. Layer confidence for a neuron belonging to a layer is calculated using the maximum likelihood of the clusters merged into that layer for that neuron. The layer confidence score for neuron $x$ belonging to layer $l$ can be evaluated as

$$LC(x|l) = \max\left(P(x|c_i)\right)_{\{c_i\}\in l}, \tag{23}$$

where $\{c_i\}$ are the clusters merged into layer $l$ and $P(x|c_i)$ is the likelihood probability for neuronal data point $x$ belonging to $c_i$. Its values lies between 0 and 1.

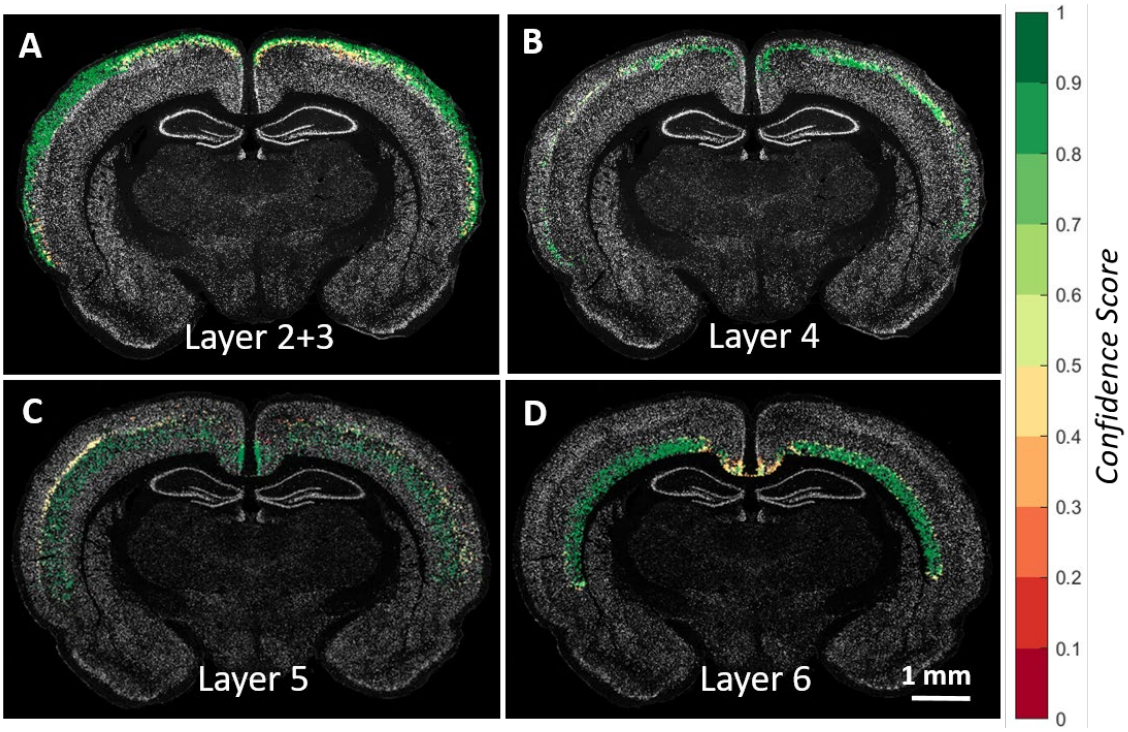


Figure 3-11. Layer Confidence Maps illustrated for (B) Layer 2+3 (C) Layer 4 (D) Layer 5 and (E) Layer 6.

As seen in Figure 3-11, our algorithm has high confidence scores for each of the layers.

### 3.3.2. Boundary Score Maps

We illustrate boundary score maps i.e. probabilistic maps of the second highest likelihood for each neuron in the layer as shown in Figure 3-12. The boundary score for neuron $x$ belonging to layer $l$ can be evaluated as

$$B(x|l) = \text{second highest } \left(P(x|c_i)\right)_{\{c_i\}\in l}, \tag{24}$$

where $\{c_i\}$ are the clusters merged into layer $l$ and $P(x|c_i)$ is the likelihood probability for neuronal data point $x$ belonging to $c_i$. Its values lies between 0 and 0.5.

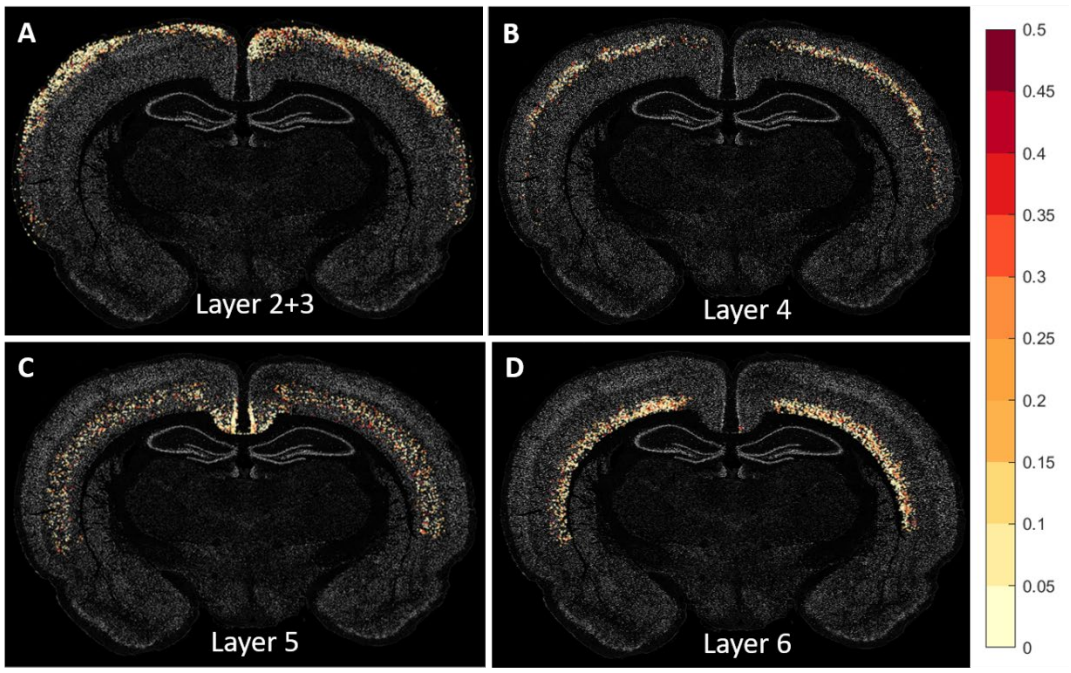


Figure 3-12. Boundary Maps illustrated for (B) Layer 2+3 (C) Layer 4 (D) Layer 5 and (E) Layer 6.

As seen in Figure 3-12, there is higher probability for the neurons at the boundary of two layers. This is normal since differentiating between neurons at boundary of two layers is a difficult task. For most of the neurons, the boundary map value stays small, indicating good clustering.

## 3.4 Performance Evaluation

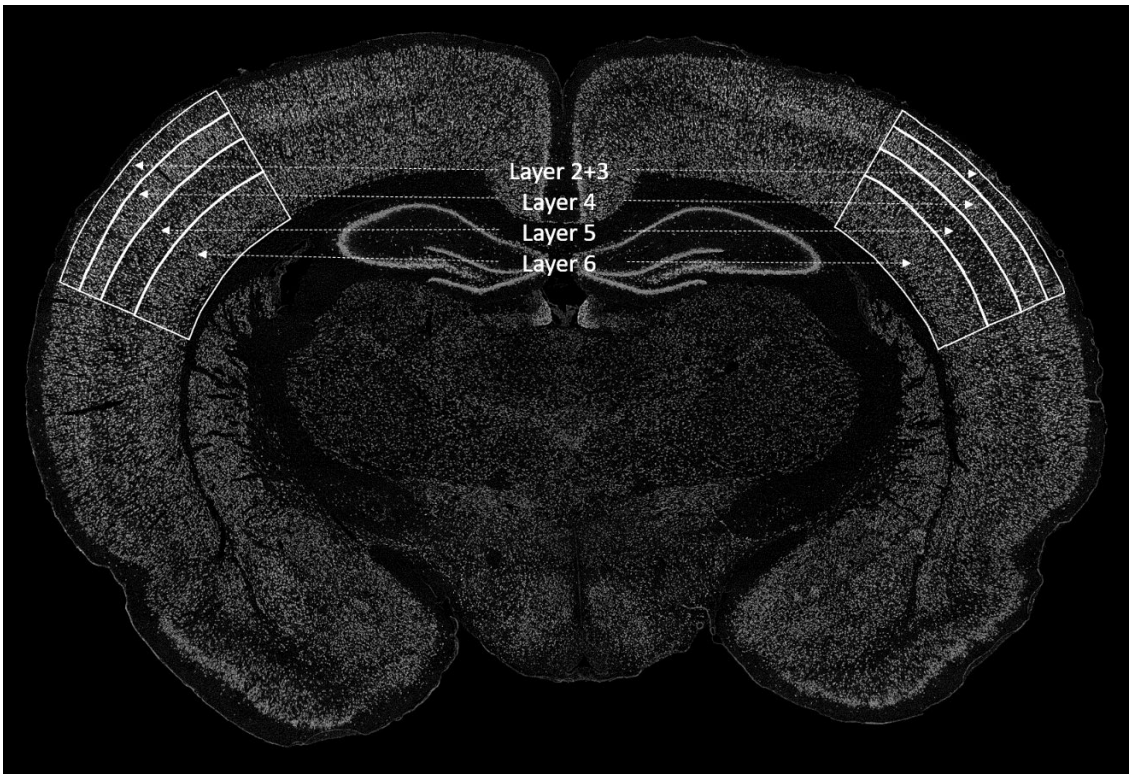


Figure 3-13. Manually delineated cortical layers (highlighted in white) in primary somatosensory barrel field for 50-plex healthy rat brain.

As discussed earlier the performance evaluation of layer delineation is challenging due to large image size and absence of an objective ground truth. We validate the cortical layer delineation in the primary somatosensory barrel field (S1BF) region (see Figure 3-13) manually delineated by Dr. Dragan Maric. This is not an objective ground truth, but it can be considered a guideline. Thickness of layers is not constant throughout the region as shown in expert delineation. The expert delineation resembles fitting lines to the region, instead of capturing the laminar flow of neurons. Hence, there are limitations to using it, but can be considered an alternative to ground truth.

We offer two supervised methods to evaluate the performance of our delineated layers, namely Intersection over Union and $R^2$-Midline distance which will be discussed later in this section. For easier analysis, we convert the point cloud of neurons belonging to each layer into corresponding binary masks (Figure 3-14) using concave hull [24].

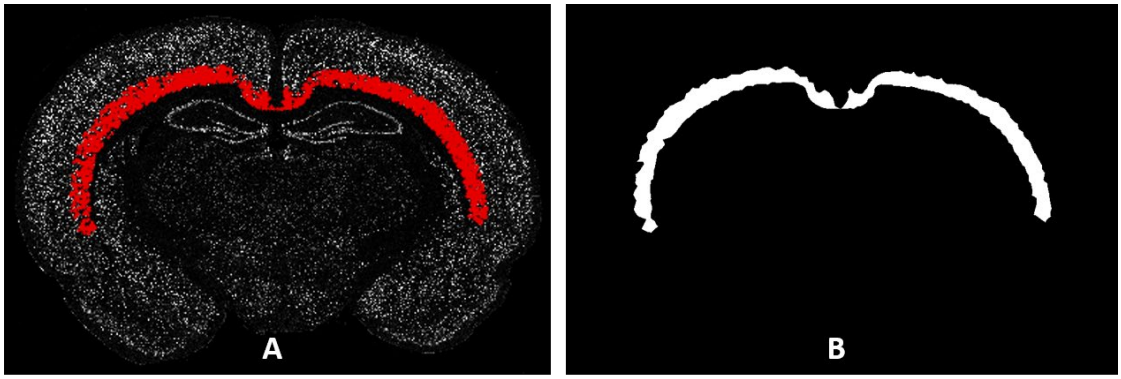


Figure 3-14. (A) Neuron point cloud for layer 6 (B) Mask created for layer 6 using concave hull.

### 3.4.1. Intersection over Union

Intersection over Union (IoU score) (Figure 3-15) for a segmentation problem is defined as

$$IoU = \frac{groundtruth \cap prediction}{groundtruth \cup prediction}. \quad (25)$$

Generally, IoU>0.5 is considered a good prediction.

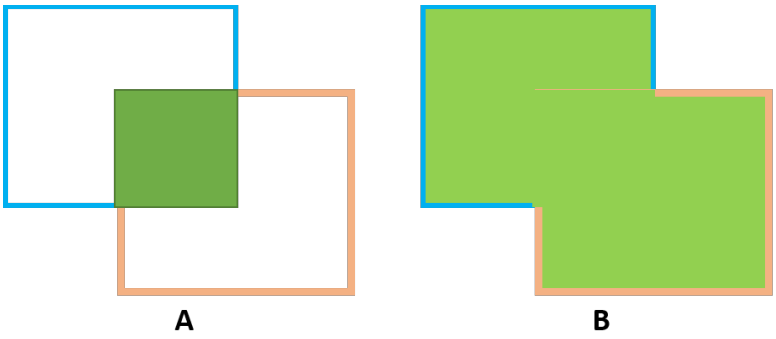


Figure 3-15. Ground truth (blue) and prediction (orange), (A) Intersection of masks (in green), (B) Union of masks (in green).

We measure the performance using IoU scores of ground truth masks ($M_{gt}$) and prediction masks ($M_{pred}$) for each layer. Below are IoU scores (Table 3-1) for the regions of interest.

Table 3-1. Table of IoU scores of ground truth and detected layer masks.

| IoU Values | Layer 2+3 | Layer 4 | Layer 5 | Layer 6 |
|---|---|---|---|---|
| **S1Bf Left** | 0.89 | 0.92 | 0.92 | 0.97 |
| **S1Bf Right** | 0.89 | 0.88 | 0.87 | 0.94 |

We observe high IoU scores for all layers on either side of S1BF region indicating good overlap with the ground truth.

### 3.4.2. Point to Layer Distance Matching

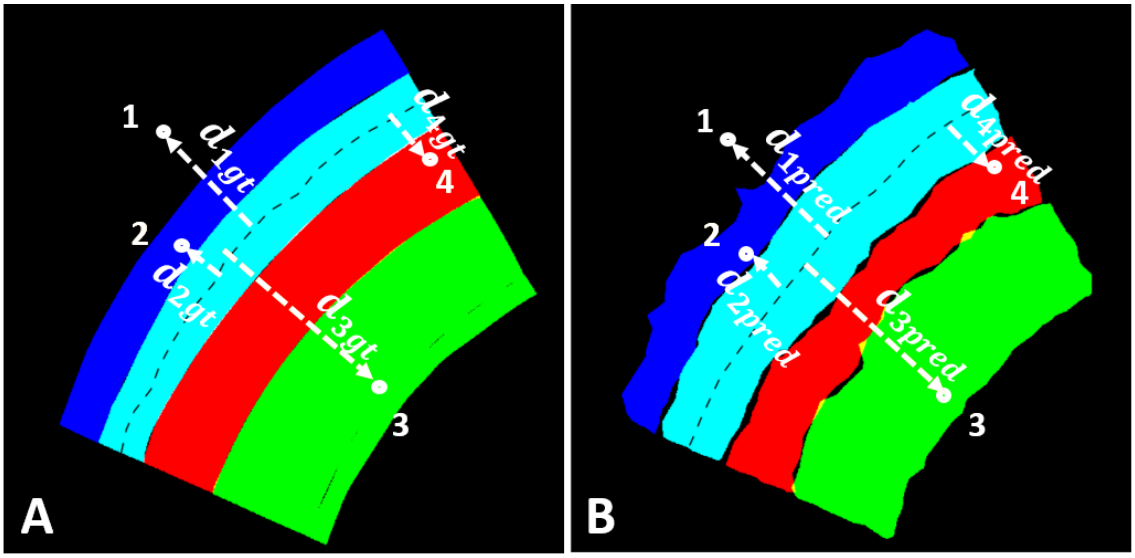


Figure 3-16. Layers 2+3 (blue), 4 (cyan), 5 (red), 6 (green) shown for S1Bf left side in (A) ground-truth masks and (B) prediction masks with mid-surface line illustrated for layer 4.

We randomly choose N points in the primary somatosensory barrel field (S1Bf) region. Next, we calculate distance of these points from mid-surface lines of ground truth masks ($M_{gt}$) and prediction masks ($M_{pred}$) for each layer (see Figure 3-16). We evaluate the R-squared values for the distances for each of the layers for N =1000 points and these are mentioned below (Table 3-2).

Table 3-2. Table of the R-squared values for the distances from each of the layers.

| **Distance R-squared** | **Layer 2+3** | **Layer 4** | **Layer 5** | **Layer 6** |
|---|---|---|---|---|
| **S1Bf Left** | 0.983 | 0.988 | 0.964 | 0.988 |
| **S1Bf Right** | 0.973 | 0.889 | 0.767 | 0.935 |

High R-squared values for all layers indicate good concordance between the computational and human-delineated cortical layer midlines.

### 3.5 Layer-Specific Dataset

We use layer specific molecular markers NECAB1 [21, 20] (mainly found in layer 4 neurons, additionally found in layer 2+3) and FOXP1 [23, 22] (found in layer 6 neurons) for validation of our algorithm (Figure 3-17 and Figure 3-18). NECAB1 marks the neuronal membrane, while FOXP1 marks the neuronal somata. We use the whole brain pipeline to process the channels and extract the required neuronal features. The detection of NECAB1 and FOXP1 positive neurons is performed by intensity-based thresholding using whole cell morphological masks, described in Chapter 5. We use the cortical layer delineation and count the percentages of positive NECAB1 and FOXP2 neurons found in the layers to evaluate the performance.

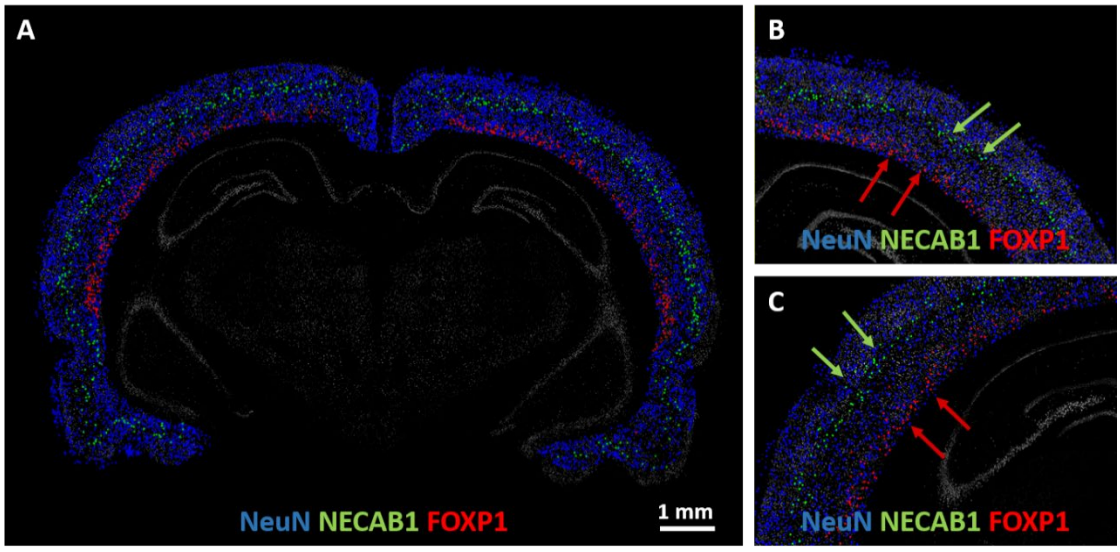


Figure 3-17. (A) The whole brain slice with NeuN, NECAB1 and FOXP2 channels. (B) Magnified version for the left side of the brain slice. (C) Magnified version for the right side of the brain slice.

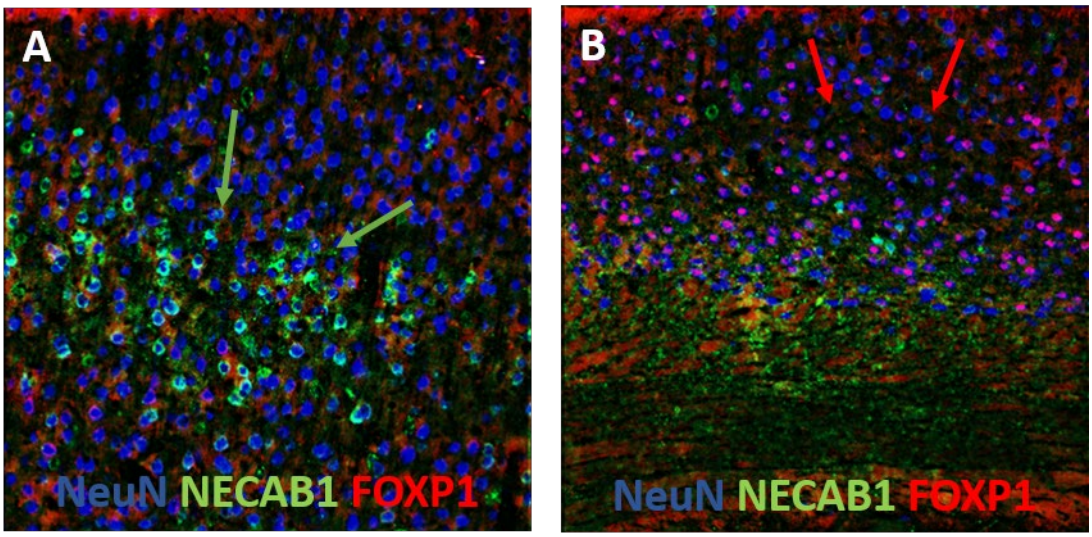


Figure 3-18. (A) NECAB1 marks the neuron membrane, (B) FOXP1 marks the somata.

The results of our cortical layer delineation are illustrated in Figure 3-19. The concave hulls extracted are used for validation. We calculate the percentage of positive NECAB1 and FOXP1 neurons detected in layer masks respectively.

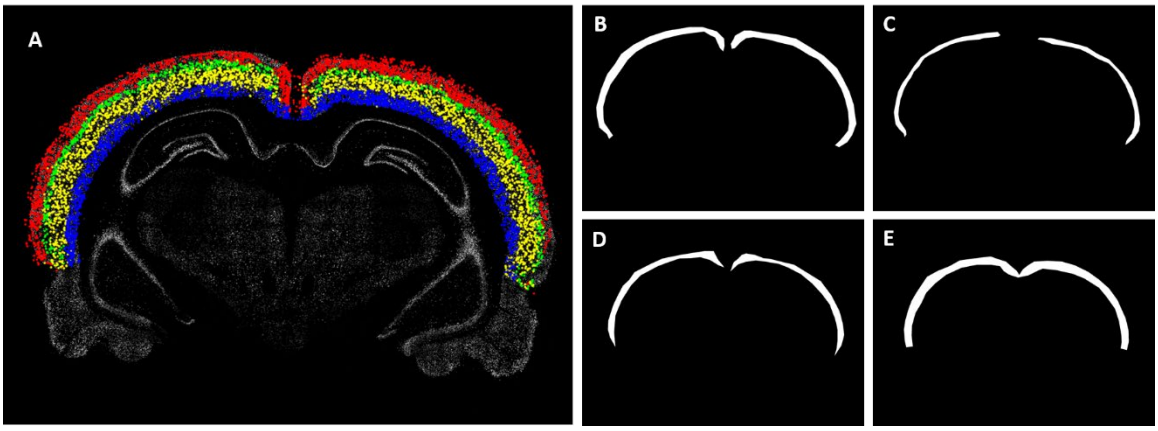


Figure 3-19. (A) Cortical layers delineated shown on top on NeuN channel for layer-specific dataset. (B)-(E) depict layer masks for layers 2+3, 4, 5 and 6.

The layer 4 and layer 6 masks generated from our proposed cortical layer delineation algorithm capture 83.9% and 99.1% of the respective layer-specific molecular markers. NECAB1 positive neurons are lower because NECAB1 also marks layer 2+3. This indicates that our algorithm is effective at cortical layer delineation.

# CHAPTER 4 CORTICAL LAYER PROFILING

We perform comprehensive and quantitative profiling of the cortical layers with respect to their composition (presence of neuronal and glial cell types and sub-types), cell-phenotypic status, and the spatial arrangement of cells. This data can be compared using both conventional and spatial statistical methods across layers within the same brain, or across different brains, for example, a normal brain vs. injured vs. drug-treated brain, allowing investigators to analyze the effects of experimental manipulations in a sensitive manner with cell-layer specificity.

## 4.1 Spatial Statistical Profiling Methods

We use comprehensive statistical methods [30, 31] for analyzing spatial point patterns of neurons allocated into different layers as per our algorithm. These exploratory methods include Empty Space function, Nearest Neighbor Distance Distribution function, Van Lieshout-Baddeley function, Ripley's function, and Pair Correlation Function. For our analysis we use pair correlation function alone, though we offer the implementation of all other exploratory methods.

Pair correlation function, $g(r)$ is a second order analysis of spatial point process that estimates the likelihood of a neuron existing at a distance $r$ from a typical neuron in layer relative to that of a random arrangement of neurons. The pair correlation function of a stationary point process is calculated as

$$g(r) = \frac{K'(r)}{2\pi r} \tag{26}$$

where $K'(r)$ is the derivative of Ripley's $K$-function $K(r)$ of the point process.

Ripley's K-function $K(r)$ of a stationary point process $X$ is defined so that $\lambda K(r)$ equals the expected number of additional random points within a distance $r$ of a typical random point of $X$. Here $\lambda$ is the expected number of points of $X$ per unit area.

For a stationary Poisson process, the pair correlation function is identically equal to 1. Values $g(r) < 1$ suggest inhibition between points; values greater than 1 suggest clustering. Figure 4-1 shows plots of pair correlation function against theoretical value for a random point pattern. Below in Table 4-1 we compare Pair Correlation Function values for neurons in delineated layers at different distances from it.

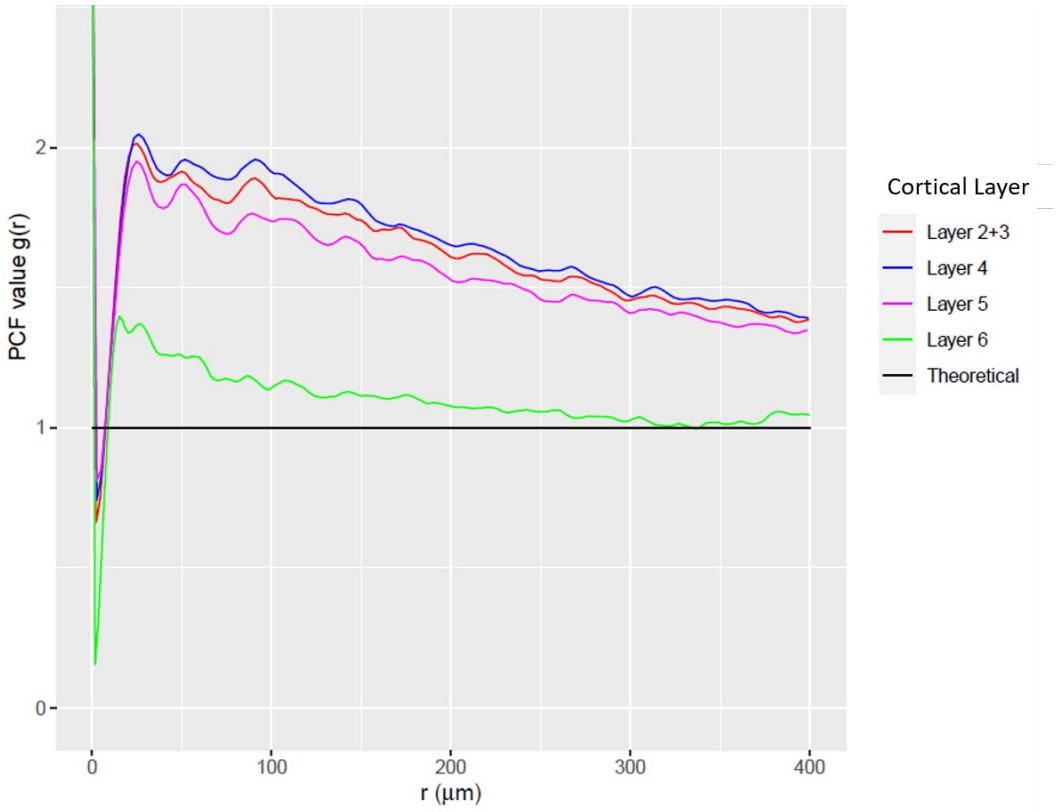


Figure 4-1. Pair Correlation Function (PCF) for neuronal point patterns in cortical layers against a theoretical random point pattern.

Table 4-1. Pair Correlation Function for Neuronal Point Patterns in Cortical Layers at radii 50 μm, 100 μm and 250 μm.

| | | Layer 2+3 | Layer 4 | Layer 5 | Layer 6 |
|---|---|---|---|---|---|
| **Pair Correlation Function Value, $g(r)$** | $r = 50$ μm | 1.9 | 1.9 | 1.8 | 1.2 |
| | $r = 100$ μm | 1.8 | 1.9 | 1.7 | 1.1 |
| | $r = 250$ μm | 1.5 | 1.5 | 1.4 | 1.0 |

We observe that all the PCF values are greater than 1 indicating clustering. We analyze PCF values for radii under 250 μm, since thickness of a cortical layer is around 250 μm on an average. We observe that neurons in layer 6, seem less clustered compared to neurons in layers 2+3, 4 and 5. This might be possible because layer 6 consists of sublayers 6a and 6b which differ in terms of the spatial arrangement of neurons.

## 4.2 Cellular Profiling

Table 4-2 shows profiling of neurons (and subtypes), astrocytes, microglia, oligodendrocytes and endothelials for healthy 50-plex rat brain across cortical layers. We additionally quantify ratio of exhibitory and inhibitory neurons across the layers.

Table 4-2. Cellular profiling for healthy 50-plex rat brain. All cellular densities are reported per $mm^2$.

| | | Layer 2+3 | Layer 4 | Layer 5 | Layer 6 |
|---|---|---|---|---|---|
| **Neuronal density** | **All** | 985.7 | 1093.7 | 1080.1 | 1464.1 |
| | **Glutamergic** | 873.2 | 916.6 | 935.3 | 1255.4 |
| | **GABAergic** | 53.9 | 58.9 | 66.6 | 38.1 |
| **Exh./Inh. Neuron Ratio** | | 16.2 | 15.5 | 14.0 | 32.9 |
| **Astrocyte density** | | 190.8 | 192.6 | 207.4 | 257.8 |
| **Microglia density** | | 93.9 | 88.8 | 98.1 | 111.3 |
| **Oligodendrocyte density** | | 99.0 | 99.3 | 160.4 | 227.9 |
| **Endothelial density** | | 302.9 | 326.4 | 349.5 | 350.5 |

Cellular profiling can be used quantify and study drug treatment experiments specific to the cortical layers. We study the astrocyte and microglial response to mild traumatic brain injury (mTBI) for the cortical layers.

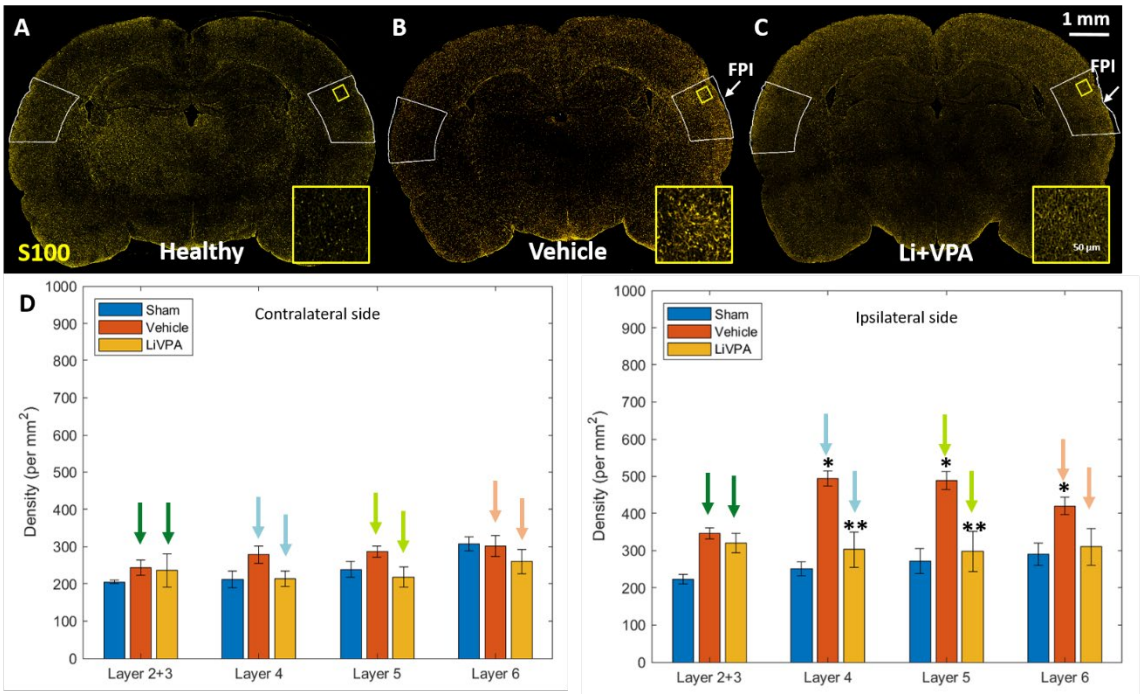


Figure 4-2. Astrocyte response to mTBI across (A) healthy, (B) vehicle and (C) Li+VPA across cortical layers between (D) contralateral and (E) ipsilateral side. Magnified regions from layer 4 shown for A, B and C on bottom right of each brain.

There is significant recruitment of astrocytes and microglia at the injury site in the cortical layers 4 and 5 for the injured animal as expected for the injured site to enhance neuronal repair and regeneration. There is significant increase in the astrocytes (see Figure 4-2) in layer 4, 5 and 6 in the injured (Vehicle) animal group. There is significant difference in the astrocyte density between injured and drug-treated (Li+VPA) animal group in layer 4 and 5, indicating that there is less inflammation in these layers in comparison to injury and the drug is helping in the injury.

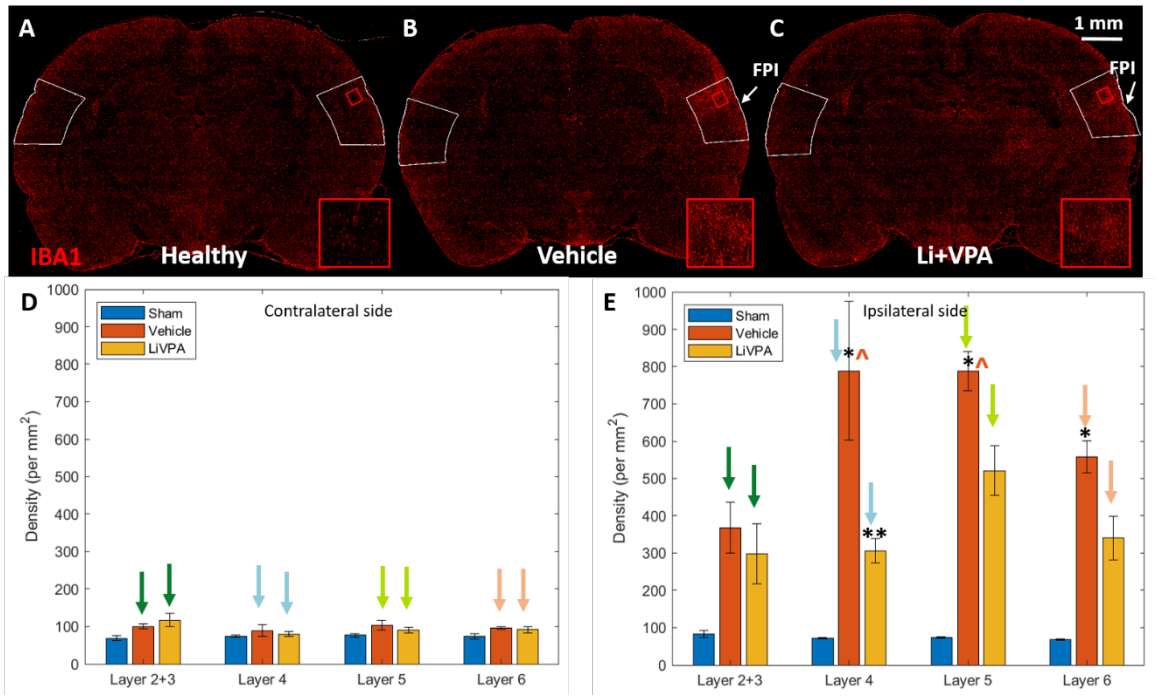


Figure 4-3. Microglial response to mTBI across (A) healthy, (B) vehicle and (C) Li+VPA across cortical layers between (D) contralateral and (E) ipsilateral side. Magnified regions from layer 4 shown for A, B and C on bottom right of each brain.

In the case of microglia (see Figure 4-3), there is significant increase in microglial density in layers 4, 5 and 6 in the injury (Vehicle) case. There is significant decrease in the microglial density in layer 4 for drug treatment animal group compared to injury group, indicating that the drug is helping in treating the injury. Also, in the vehicle brain, the microglia density is higher in deeper layers 4 and 5, compared to layer 2+3.

## 4.3 Morphological Profiling

Table 4-3 shows morphological profiling of neurons for healthy 50-plex rat brain across the delineated cortical layers. The orientation reported is with the pial surface.

Table 4-3. Morphological profiling for healthy 50-plex rat brain.

| | **Layer 2+3** | **Layer 4** | **Layer 5** | **Layer 6** |
|---|---|---|---|---|
| **Average Neuron Diameter, µm** | 19.6 ± 0.1 | 20.2 ± 0.1 | 19.4 ± 0.09 | 18.3 ± 0.1 |
| **Average Neuron Area, µm$^2$** | 162.6 ± 3.1 | 176.2 ± 4.3 | 167.9 ± 3.4 | 148.7 ± 3.3 |
| **Average Neuron orientation, °** | 71.5 ± 0.3 | 69.9 ± 0.6 | 58.5 ± 0.4 | 37.8 ± 0.5 |

Below in Figure 4-4, we show the morphological profiling for the primary somatosensory cortex barrel field. We analyze this region because it has been well studied in literature. Comparison of neurons across cortical layers reveals that neurons in layer 4 are observed to be largest in size. Neurons in layer 6 are observed to be the smallest in size in terms of both area and diameter. Neurons in layer 6 are aligned along the pial surface. The relative density is lowest of layer 2+3 and highest for layer 6, followed by layer 4.

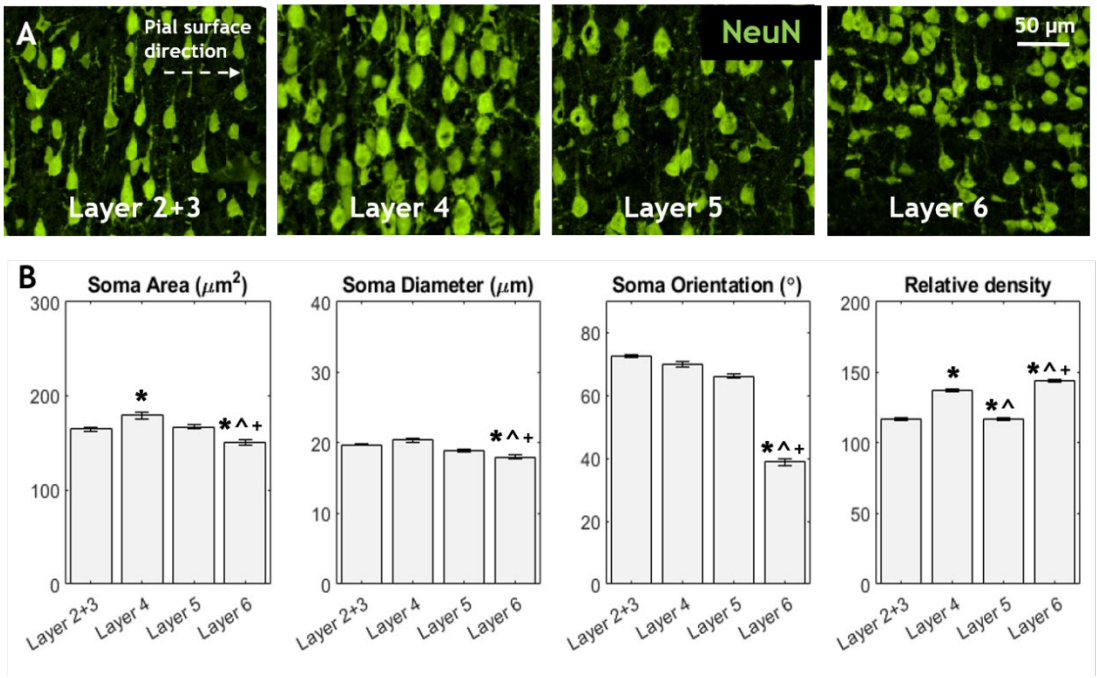


Figure 4-4. (A) Neurons from layers shown for S1BF region in a healthy rat brain. (B)The neurons compared against each other in terms of area, diameter, orientation, and relative density in a bar chart.

We extend morphological profiling to the injured animal (in Figure 4-5). We can see that the size of neurons decreases in the case on the ipsilateral side. Also, there is a significant recruitment of CC3, the cell death marker on the ipsilateral side.

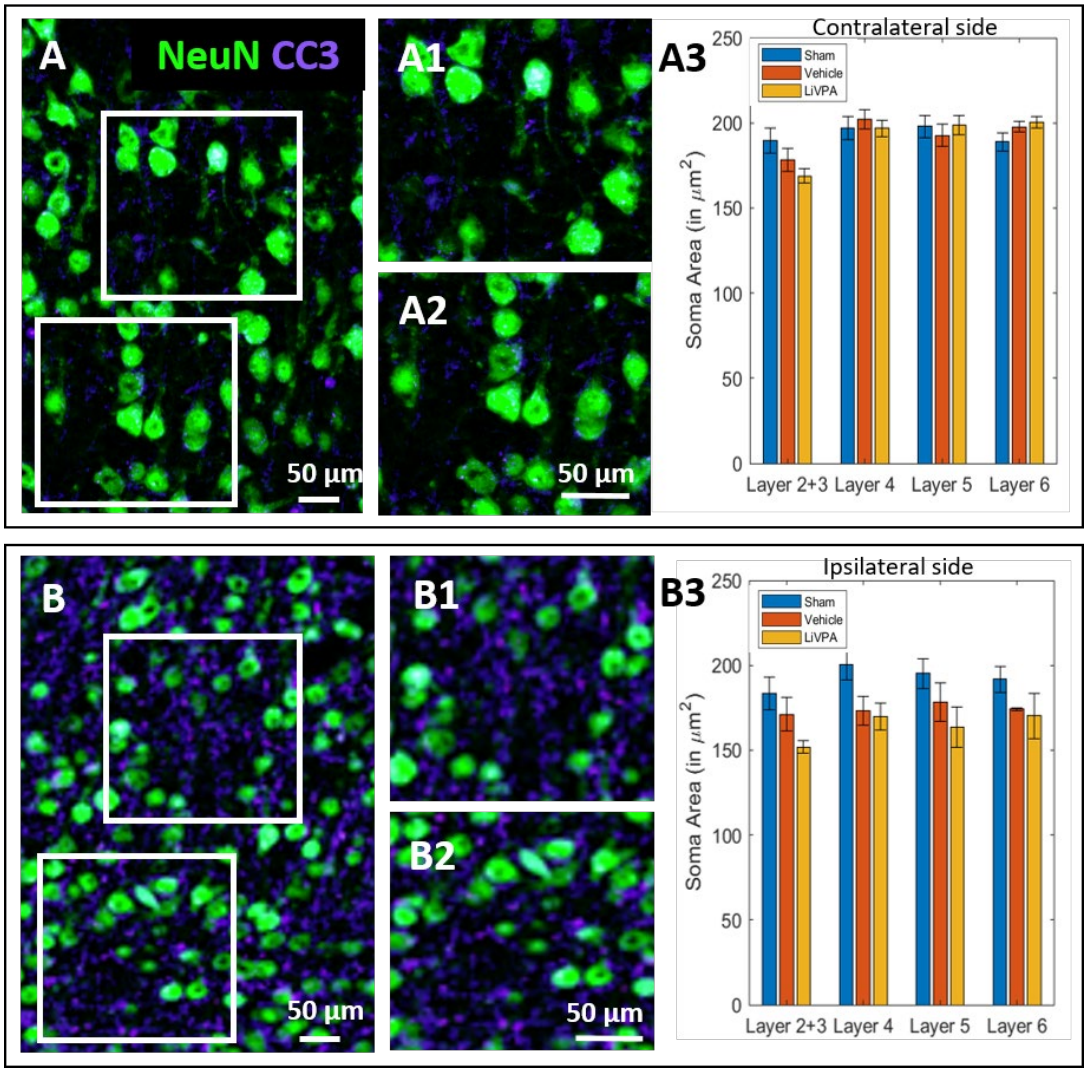


Figure 4-5. Comparing neurons from layer 6 in the injured brain across (A) contralateral side and (B) ipsilateral side. (A3) and (B3) compare soma area across both sides.

# CHAPTER 5 MORPHOLOGICAL SEGMENTATION

For an in-depth analysis of cell function and spatial distribution, it is important to characterize the morphologies of cells in the rat brain. This would help in studying patterns of tissue perturbations and quantifying cellular heterogeneity. We develop robust algorithms to automate the segmentation and reconstruction of cells across the whole rat brain. Presence of proteins like Nestin, Vimentin, Myelin Basic Protein, Neurofilaments in the processes can provide information about cell motility, neuronal signaling. Similarly, existence of Cleaved Caspase-3 in the cytoplasm can confirm cell death. In the case of neurons, GAD67, Choline Acetyltransferase, Glutaminase, Tyosine Hydroxylase (TH) biomarkers in the soma and processes can reveal neurotransmitters used for neuronal signaling. For quantifying the soma properties for cortical delineation, soma segmentation is important. Thus, it becomes necessary to morphologically mask the cytoarchitecture of cells.

There has been work by Megjhani et al. [32] for microglial arbor segmentation of around 3,310 microglia using supervised approach. Astrocytes process detection using unsupervised tracing algorithm has been mentioned in [33] implemented on around 20,000 astrocytes. Huang et al. [34] used weakly supervised learning of three-dimensional neural networks for neuron reconstruction. We propose robust unsupervised methods using unsupervised arbor seed point detection and reconstruction to segment molecular morphologies of around 200,000 cells of all major cell types including astrocytes, neurons, endothelial, microglia and oligodendrocytes.

The reconstruction is done for each cell in the order: Nucleus -> Soma -> Cytoplasm->Processes->Whole Cell. The molecular markers in Table 5-1 are being used for cell-type based morphological segmentation.

Table 5-1. Table of biomarkers used for morphological segmentation of different cell components for neurons, microglia, astrocytes, endothelial and oligodendrocytes.

| Cell Type | Nucleus | Soma | Processes | Cytoplasm | Membrane |
|---|---|---|---|---|---|
| Neurons | NeuN | NeuN | MAP2 | N/A | N/A |
| Microglia | N/A | IBA1 | IBA1 | N/A | N/A |
| Astrocytes | Sox2 | S100 | S100, GFAP | N/A | N/A |
| Endothelials | N/A | N/A | N/A | GFP | RECA1 |
| Oligodendrocytes | Nucleus | CNPase | CNPase | N/A | N/A |

## 5.1 Whole Cell Morphological Segmentation

We propose an unsupervised arbor seed point detection and reconstruction using molecular markers to characterize whole cell morphologies.

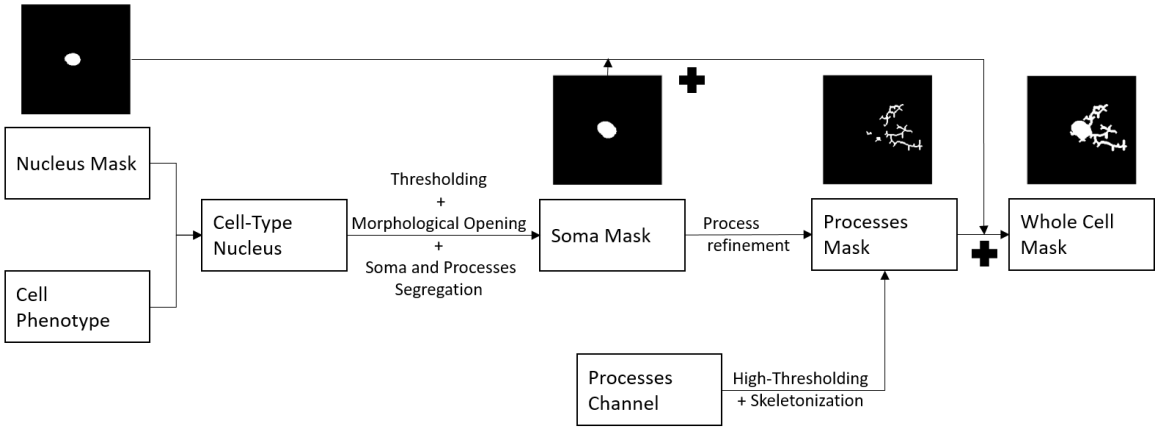


Figure 5-1. Basic pipeline for cell morphological segmentation.

The basic pipeline for morphological cell segmentation (Figure 5-3) can be used in all the five common cell types after making small changes. For every cell type, the morphological reconstruction is handled separately, due to different biomarkers and their staining nature. Sox2, S100 and GFAP channels are used to reconstruct astrocytes. We use GFP and RECA1 for endothelial reconstruction. IBA1 channel is used to reconstruct microglia. MAP2 and NeuN channels are used for neuron reconstruction. Olig2 and CNPase are used to reconstruct oligodendrocytes. We use nucleus segmentation from masked RCNN and cell phenotype from the Capsule Network [7].

### 5.1.1. Astrocyte Reconstruction

Sox2, S100 and GFAP channels are used to reconstruct astrocytes. Sox2 are neural precursors for astrocytes and mark astrocyte nuclei. S100 are astrocyte-pan specific markers which mark soma and processes. GFAP marks processes for astrocytes subset.

We use the nucleus segmentation from the masked RCNN and crop window of size 100×100 around it in the S100 channel. S100 channel marks soma and processes.

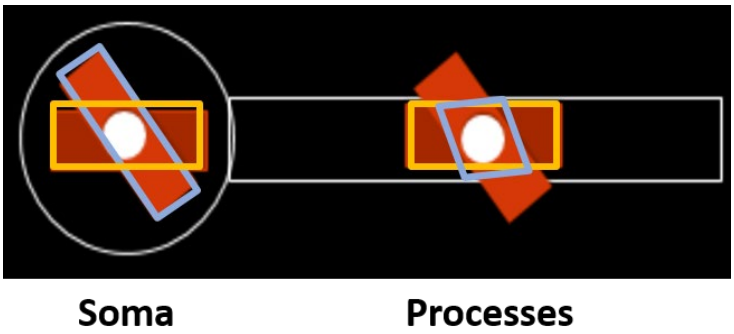


Figure 5-2. Area of rectangle centered at soma (left) remains constant for different orientations, while it varies highly in case of processes (right).

We use directional ratios [35] to measure local isotropy and anisotropy at multi-levels to segregate soma and processes (see Figure 5-4). Given collections of multiscale orientable filters $\{\varphi_{j,l}\}$ where the indices $j, l$ is associated with a range of scales and orientations, respectively, the Directional Ratio (DR) of an image $f$ at the $j^{th}$ scale and at point $p$ is the quantity is defined as

$$DR_j f(p) = \frac{(min_l\{|f * \varphi_{j,l}(p)|\})}{(max_l\{|f * \varphi_{j,l}(p)|\})}. \quad (27)$$

We use filter $\varphi_{j,l}(x) = S_{j,l}(x)$, where the sets $S_{j,l}$ are the scaled and rotated rectangles as

$$S_{j,l} = 2^j R_{\theta_l} S, \tag{28}$$

$$R_\theta = \begin{pmatrix} cos\theta & sin\theta \\ -sin\theta & cos\theta \end{pmatrix}, \tag{29}$$

and $S$ is a fixed rectangle of size 2×1 pixels. DR value ranges from 0 to 1 with low values around processes and high values around soma. The segregation procedure is as below:

We use $j$ = 3 to 5 and $\theta_l$ = 0° to 180° at locations of skeletonized version of earlier detected soma, and threshold (DR values) to distinguish soma from processes. This is followed by smoothing the image to smoothen the edges of detected soma to remove existing small processes.

In case of astrocyte, processes will be marked by S100 or GFAP depending on the cell activation state. We use a window size of 200×200 around the nucleus. To find which biomarker stains the processes, we use a disk of size 2 pixels around the soma. We calculate the sum of GFAP channel intensity and S100 channel intensity and consider the channel with higher intensity for processes reconstruction. We binarize the processes channel and perform skeletonization to get the processes structure. We get the endpoints of the arbor structures and remove endpoints which are part of the soma. We use get processes which contain the remaining endpoints.

Cytoplasm is obtained by subtracting nucleus mask from the soma mask. We get membrane by a 1-pixel dilation of the combined mask of soma, nucleus, and processes. The whole cell is acquired by the combined mask of soma, membrane, nucleus, and processes.

### 5.1.2. Endothelial Reconstruction

We use GFP and RECA1 for endothelial reconstruction. GFP marks the cytoplasm and is brightest in the soma, RECA1 marks the plasma membrane. We use the nucleus segmentation from the masked RCNN and crop window of size 200×200 around the nucleus position for plasma membrane and cytoplasm masking. We get the plasma membrane using RECA1 biomarker. This is done by Otsu based thresholding, followed by getting the connected component in the image center and filling the holes using flood-fill algorithm. The cytoplasm is extracted by binarizing the GFP, removing the small noisy objects in the image with median blur. This is proceeded by picking the largest connected and filling any possible holes. The whole cell is acquired by combining nucleus, soma, membrane, and cytoplasm masks.

### 5.1.3. Microglia Reconstruction

Microglia reconstruction is performed using IBA1 channel which marks the soma and processes of microglia. We use the nucleus segmentation from the masked RCNN and crop window of size 100×100 around it in IBA1 channel. Since IBA1 marks both soma and processes, we need to distinguish the potential processes from soma. This is done by blurring the image with Gaussian kernel of size 11×11 and binarizing to get soma mask. To get the processes, a window of size 200×200 is cropped around nucleus center in the IBA1 molecular marker. Potential processes are masked using complement of combined soma masks. We extract the brighter processes using high threshold values. Skeletonization of extracted processes is used to capture the structure. The endpoints of this structure are extracted, and all the endpoints which lie outside the soma are kept. The

final endpoints are used to get the microglia processes. Cytoplasm is obtained by subtracting nucleus mask from the soma mask. We get membrane by a 1-pixel dilation of the combined mask of soma, nucleus, and processes. The whole cell is acquired by the combined mask of soma, membrane, nucleus, and processes.

### 5.1.4. Neuron Reconstruction

We use NeuN and MAP2 channels to reconstruct neurons. NeuN marks soma and nucleus. MAP2 marks the dendrites of neurons. We use the nucleus segmentation from the masked RCNN and crop window of size 100×100 around it in the NeuN channel. We binarize this image by Otsu's thresholding and fill any holes. This provides soma mask for the neuron. MAP2 channel marks the dendrites. A window of size 200×200 is cropped nucleus center in this channel and masked with complement of soma mask. Then binarization using high threshold values is performed followed by skeletonization to get the internal structure of dendrites. The endpoints of this structure are extracted, and all the endpoints which lie outside the soma are kept. The final endpoints are used to get the dendrites. Cytoplasm is obtained by subtracting nucleus mask from the soma mask. We get membrane by a 1-pixel dilation of the combined mask of soma, nucleus and processes. The whole cell is acquired by the combined mask of soma, membrane, nucleus and processes.

### 5.1.5. Oligodendrocyte Reconstruction

We use Olig2 and CNPase biomarkers to reconstruct oligodendrocytes and capture its cytoarchitecture. Olig2 marks the nucleus of oligodendrocytes, CNPase is oligodendrocyte-pan specific marker which marks the soma and processes. The nucleus detected from masked RCNN is used along with the Olig2 channel. In case Olig2 channel

is present, nucleus is updated as intersection of detected nucleus and binarized Olig2. Otherwise the nucleus mask is directly used. Since it's difficult to separate soma and processes marked by CNPase channel, detected nucleus is dilated by 2-pixel to get the approximate soma. A window of size 200×200 is cropped around nucleus center in CNPase channel and it is binarized using high threshold value. Skeletonization is used to get the internal structure of processes. The endpoints of this structure are extracted, and all the endpoints which lie outside the soma are kept. The final endpoints are used to get the final processes. Cytoplasm is obtained by subtracting nucleus mask from the soma mask. We get membrane by a 1-pixel dilation of the combined mask of soma, nucleus, and processes. The whole cell is acquired by the combined mask of soma, membrane, nucleus, and processes.

## 5.2 Results

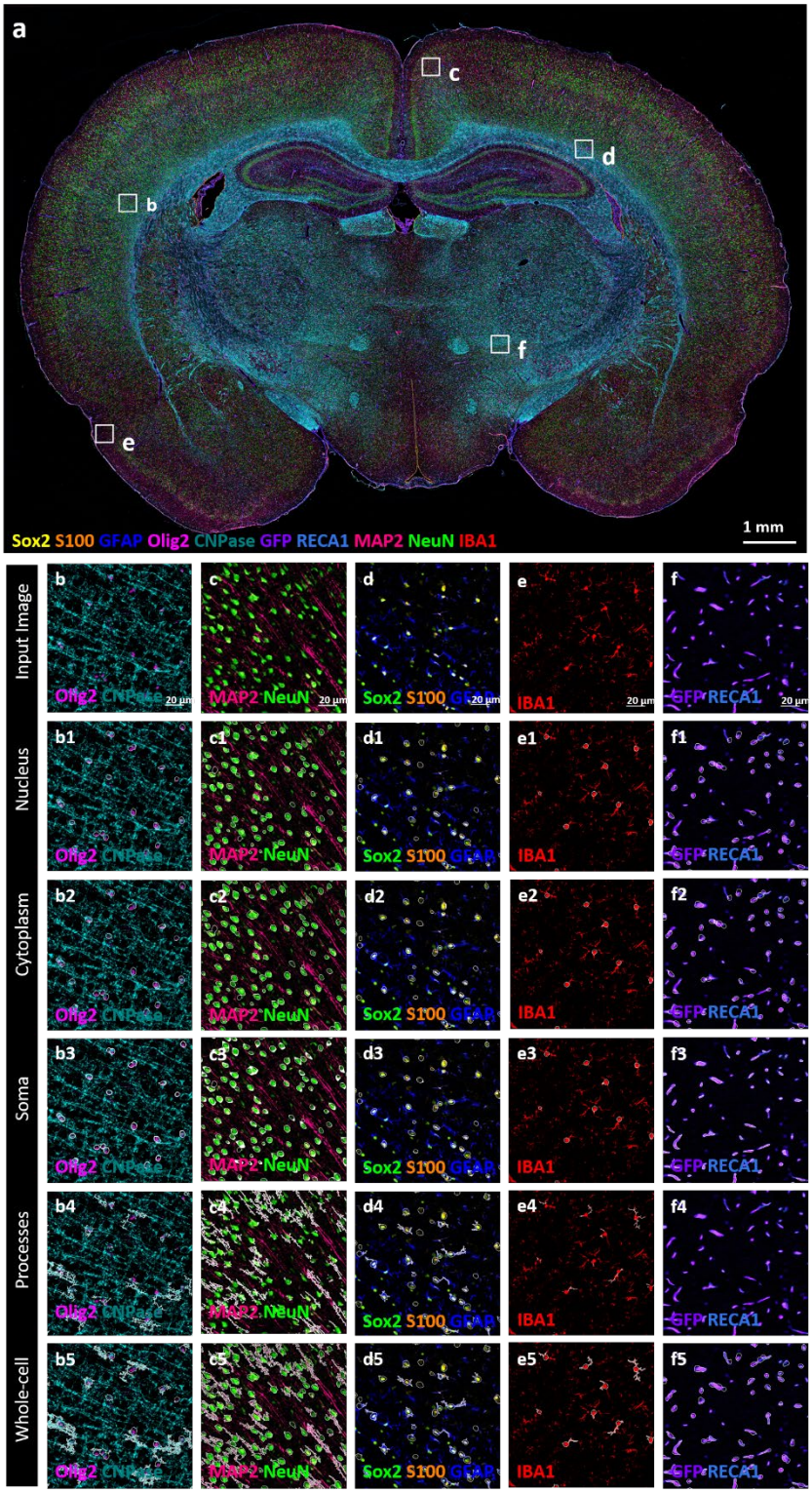


Figure 5-3. Large-scale morphological segmentation results for different cell types.

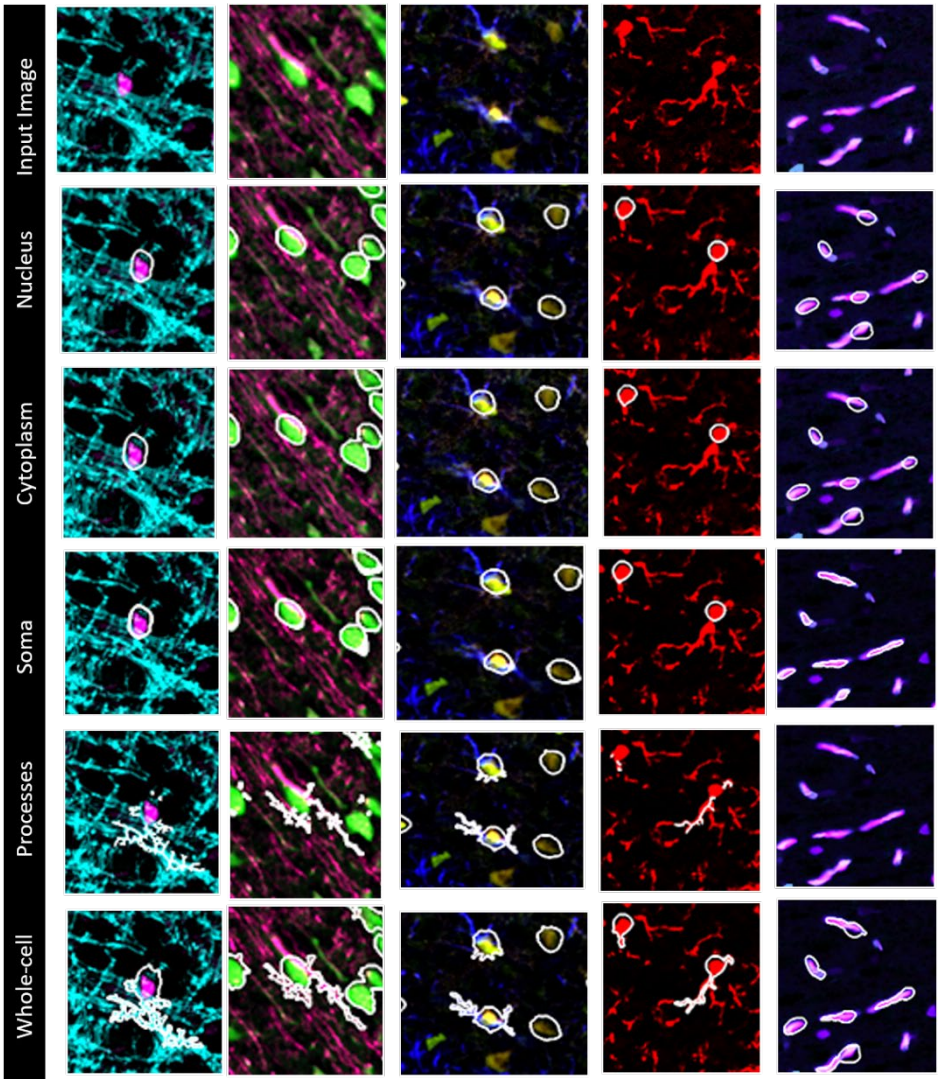


Figure 5-4. Cell-level morphological segmentation results for different cell types.

The morphological segmentation of oligodendrocytes, neurons, astrocytes, microglia and endothelials into neurons, cytoplasm, soma, processes, and whole cell (see Figure 5-5 and Figure 5-6). Morphological masking can be used in studying in-depth patterns of tissue perturbations and quantifying cellular heterogeneity as opposed to analyzing the cell only as per nuclei and cell body. It can be used for proof-reading cell phenotyping and improving the cell state activation.

# CHAPTER 6 LABEL EFFICIENT DEEP LEARNING FRAMEWORK

Breast cancer is the most common cancer in women worldwide [36]. The most widely used diagnostic method for breast cancer is visual inspection of histopathological images. In order to increase the speed and precision of classifying breast cancer histopathological images into benign or malignant tumor, it is important to implement an automated method. In solving image classification problems with such high intra-class variability, Convolutional Neural Networks (CNN) have outperformed traditional machine learning approaches. However, they require more annotated data for training compared with conventional methods. Such a requirement creates a major obstacle when using CNNs in the medical image domain. This paper explores active learning methods to train high-quality CNNs using fewer but more informative data samples. We investigate two active learning approaches, based on entropy and Bayesian criteria, to classify histopathological tumor images into benign and malignant. Our approach yields a competitive accuracy by using only half of the training data as opposed to random selection approach. This finding makes active learning an appealing framework for building deep networks for biomedical applications where labeled data is often scarce.

## 6.1 Introduction

As reported by the WHO [36], cancer is responsible for around 8.2 million deaths in 2012 and is expected to cause 27 million deaths by the year 2030. Breast cancer is the most common cancer occurring in women worldwide, with one of the highest mortality rates. There has been a tremendous amount of ongoing research regarding breast cancer diagnosis and treatment. Routinely administered screening such as mammography can detect breast cancer much earlier, before the development of symptoms. Improved treatment methods,

along with the benefits of early screening has decreased the mortality rates due to breast cancer. Most of the breast cancer tumors detected are benign or not cancerous. These tumors do not grow uncontrollably or metastasize and are not life-threatening. These are unlikely to recur once removed. On the other hand, malignant tumors are cancerous. They can spread to other cells and can invade nearby tissues. The cells in a malignant tumor have abnormal chromosomes and DNA which may require aggressive treatment such as surgery, radiation, chemotherapy, or immunotherapy-based medications. It might recur after removal, sometimes in areas other than the original cancer site.

When cancer is suspected in diagnostic tests or screening mammography, microscopic analysis of breast tissue is necessary for a definitive diagnosis, to determine the extent of spread, and characterize the type of the disease. When cancer is suspected in diagnostic tests or screening mammography, microscopic analysis of breast tissue is necessary for a definitive diagnosis, to determine the extent of spread, and characterize the type of the disease. The tissue for microscopic analysis is acquired via a biopsy, which consists of collecting samples of cells or tissue followed by staining and microscopic examination. Pathologists visually inspect stained breast biopsies to make the diagnosis by examining the textures, patterns, and morphology of these complex histopathological images (Figure 6-1) to categorize the tissues into cancerous (malignant) or non-cancerous (benign) tumors. This is considered the gold standard for diagnosis of breast cancer. Histopathological image analysis is a time-consuming, specialized task and depends highly on the experience and working conditions of pathologists. There has been a constant need for computer-assisted

diagnosis (CAD) to relieve the workload on pathologists [37], while improving the reliability and consistency of detection.

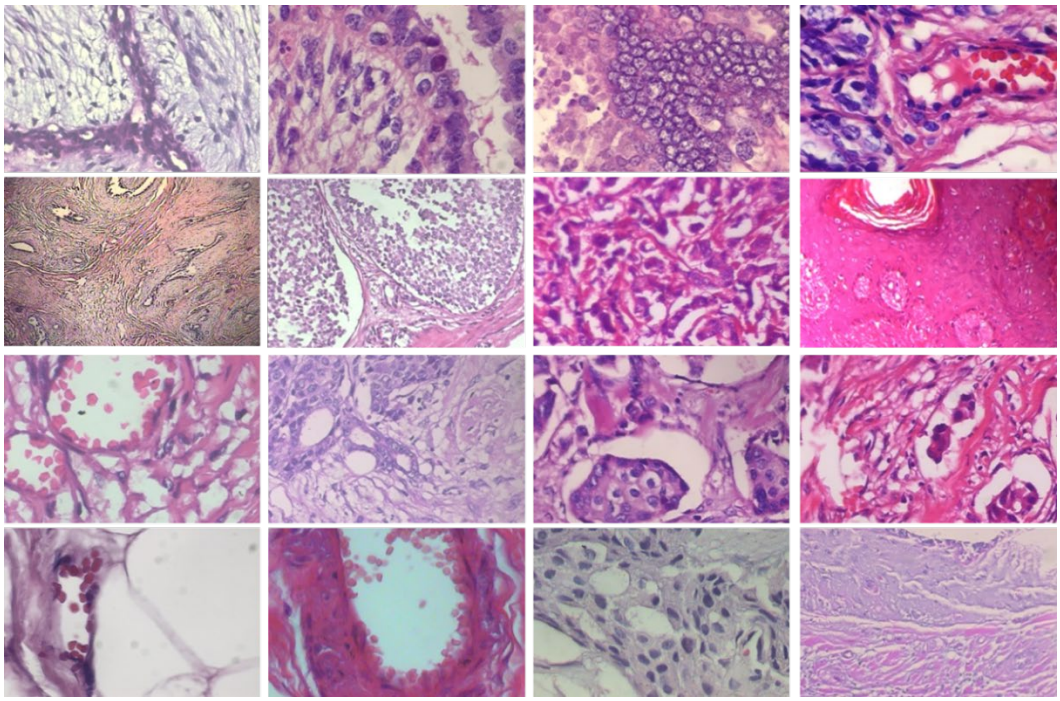

Figure 6-1. BreaKHis database consists of malignant and benign breast tumor images, at different magnification factors (MF): 40×, 100×, 200× and 400×. These images (H & E staining) vary widely in terms of the textures, patterns, and morphology.

The earliest published work on automatic imaging processing for cancer diagnosis dates back to more than forty years [38]. Amidst the extensive ongoing research in the field, due to the complexity of images needed for diagnostic analysis, the problem of classifying tumors remains challenging. Most of the earlier works used handcrafted features such as intensity information, textural patterns and object-level morphological information (size, shape, distribution of nuclei) individually or as a combination for classification of histopathology images of breast tissue. There was use of visual descriptor based handcrafted features such as Local Binary Pattern (LBP) [39], Completed LBP (CLBP) [40], Local Phase Quantization (LPQ) [41], Gray-Level Co-occurrence Matrix

(GLCM) [42], Threshold Adjacency Statistics (TAS), ORB and Scale-Invariant Feature Transform (SIFT), Histogram of Oriented Gaussians (HOG), color histogram for classification. Traditional machine learning classifiers such as Support Vector Machine (SVM), Random Forests, Naive Bayes, and K-Nearest Neighbors were commonly used with handcrafted features [43, 44, 45, 46]. Most of the breast cancer analysis was carried out on small, privately-owned datasets. In order to mitigate this gap, Spanhol [45] introduced the Breast Cancer Histopathological (BreaKHis) database, consisting of 7,909 breast histopathological images acquired on 82 patients. The authors also evaluated classification performance on six different textural descriptors and different classifiers, with accuracy rates ranging from 80% to 85%, depending on the image magnification factor. Based on the results presented in [45] , it can be said that the texture descriptors can offer an accurate representation to train classifiers.

The handcrafted features are based on the knowledge of an expert and are extracted using the information from the histopathological image. Representation learning [47] addresses this problem, by being able to extract and organize discriminative information from the data, without expert supervision. Breast cancer recognition based on Probabilistic Neural Networks and SVM was performed in [48]. Computer-assisted breast cancer classification system in [49] consisted of a cascade of SVM and Multi-Layer Perceptron (MLP) ensemble classifiers, with rejection option for difficult cases. With advancements in machine learning, computational power and an increase in data size and complexity, deep learning methods have shown significant improvements over state-of-the-art recognition and classification approaches. They are also actively used for histopathology image analysis [50, 51].

Spanhol et al. [52] performed a patch-based classification using CNNs on the BreaKHis [45] dataset, which is the dataset of interest for our work and displayed an improvement of 6% in terms of accuracy compared to the traditional approach. Bayramoglu et al. [53] proposed a CNN model that can learn and predict breast cancer regardless of the different magnifications of images in the dataset. Wei et al. proposed BiCNN model [54] based on the GoogLeNet [55] that outperformed other state of the art CNNs. [56] proposed a multi-classification model to identify subordinate classes of breast cancer using deep learning. [57, 56] proposed CNNs for breast cancer classification based on state of the art architectures in object recognition such as ResNet [58], RCNN [59], Inception-v4 [60], with fewer parameters to reduce the risk of model over-fitting. As discussed, deep learning methods have outperformed traditional machine learning approaches for classification in histopathology data, in general, but in turn, require large amounts of labeled training data. Labels are difficult to obtain in histopathological images, as image labeling requires significant clinical expertise.

In the case of medical images [50], due to a limited amount of data available, transfer learning has proven to be a commonly adopted strategy. Transfer learning [61] involves using a pre-trained model, which is already learned in a specific domain, to another knowledge domain. In most cases, this pre-trained network is used either as a feature extractor or for initialization of CNNs followed by fine-tuning for handling smaller medical image dataset. [62] demonstrated that features extracted for the BreaKHis dataset from a pre-trained network achieved comparable recognition rates to trained CNN. In this paper, we address the problem of using small labeled data from the breast histopathology images to achieve performance as close as training CNN with the whole dataset. There is related

work done in semi-supervised learning where a small amount of labeled data and remaining unlabeled data are used to get a higher performance compared to using labeled data alone. Active learning is a special case of semi-supervised learning where provided a small amount of labeled data and remaining unlabeled data, the algorithm obtains labels for a small number of unlabeled data to improve the performance. There are several criteria like uncertainty sampling, entropy, margin sampling, expected reduction in error, which choose the desired data points. The hypothesis is that these selected data points when labeled and used for training perform as good as training with all data points. This allows the classifier to work with smaller data to select informative samples for object recognition and classification tasks. The use of active learning in deep learning is relatively limited. Wang et al. [63], first used active learning to aid image classification using stacked restricted Boltzmann machines and stacked autoencoders. There has been an implementation of similar ideas in the case of hyperspectral images [64], and colonoscopy frame images [65] in recent years.

Most active learning methods discussed above are known to successfully learn and update classifiers when dealing with low-dimensional data. There has been the use of margin-based uncertainty for SVM classifier [66, 67]. Similarly, gaussian approaches with RBF kernels have been used to get model uncertainty [68, 69]. Entropy has outperformed several other active learning criteria [70]. The use of active learning for breast cancer classification [71, 72] using deep learning networks is fairly limited. We implement an entropy-based approach to measure the uncertainty of our CNN.

CNNs deal with high dimensional data and the representation of model uncertainty becomes extremely challenging. Thus, we implement Bayesian approaches to deep

learning, in parallel, and capture model uncertainty [73, 74, 75]. This uncertainty is used to develop a similar active learning framework, as when using entropy alone, for the classification of histopathological images.

Our work investigates several statistical criteria for performing active learning using deep networks. For example, one approach actively picks images with the highest entropy. High entropy indicates the images regarding which current classifier is most uncertain about. Entropy has outperformed several other traditional active learning criteria [70]. The classifier is retrained incrementally using this approach and there is a significant increase in classifier's performance with every retrain. We analyze the proposed active learning approaches on breast cancer classification and thoroughly compare against baseline methods. These can be used for actively training a deep neural network, in the absence of a large amount of labeled data, which is a prevalent challenge in biomedical domains. We also exhaustively analyze the behavior of active learning methods, which has not been done before to the best of our knowledge. Our paper will make the following contributions:

1. We formulate an active deep learning framework to train CNNs with less amount of labeled data. We implement two parallel active learning criteria for the same.
2. We provide extensive experimental results and in-depth analysis to demonstrate the effectiveness of our algorithm on the breast tumor classification problem.

## 6.2 Methods

### 6.2.1. Data Acquisition

Breast Cancer Histopathological (BreaKHis) database [45] contains microscopic biopsy images of benign and malignant breast tumors. Malignant tumors are locally invasive. They can invade and destroy tissues around it and spread around. Benign tumors are non-cancerous and remain localized. Thin sections from the breast tissue biopsy (surgical open biopsy) are stained with hematoxylin and eosin (H&E). Hematoxylin stains the nuclei, whereas eosin stains protein structures in the cells. BreaKHis database consists of 5,429 malignant and 2,480 benign breast tumor images (Figure 6-1) collected from 82 patients, at different magnification factors (Table 6-1) 40×, 100×, 200×, 400× zoomed-in area of interest selected by the pathologist. Benign tumors can be sub-categorized into Adenosis (A), Fibroadenoma (F), Phyllodes Tumor (PT) and Tubular Adenoma (TA). Malignant tumors can be sub-categorized into Carcinoma (C), Lobular Carcinoma (LC), Mucinous Carcinoma (MC) and Papillary Carcinoma (PC) (Table 6-2). These RGB images are of size 700×460 pixels each. We use these images without using their magnification factor information for classification into malignant and benign tumors.

### 6.2.2. Convolutional Neural Networks

Convolutional Neural Network (CNN) is a class of deep neural networks [76]\ which is most commonly used for image classification and recognition. They learn multiple levels of image representation to model the complex relationship between image and class labels. They consist of convolutional layers, activation function, pooling layers, fully connected layers, and normalization layers.

Table 6-1. BreaKHis Dataset in terms of tumor type and magnification factor.

| Magnification Factor | Benign | Malignant | Total Number of Images |
|---|---|---|---|
| 40 × | 652 | 1,370 | 1,995 |
| 100 × | 644 | 1,437 | 2,081 |
| 200 × | 623 | 1,390 | 2,013 |
| 400 × | 588 | 1,232 | 1,820 |
| Total Images | 2,480 | 5,429 | 7,909 |

Table 6-2. BreaKHis Dataset in terms of tumor category and tumor sub-category.

| Tumor Category | Tumor Sub-Category | Number of Images | Total Images |
|---|---|---|---|
| Benign | Adenosis | 444 | 2,480 |
| | Fibroadenoma | 1,014 | |
| | Phyllodes Tumor | 453 | |
| | Tubular Adenoma | 569 | |
| Malignant | Carcinoma | 3,451 | 5,429 |
| | Lobular Carcinoma | 626 | |
| | Mucinous Carcinoma | 792 | |
| | Papillary Carcinoma | 560 | |

We will be using AlexNet [77] as the base Convolutional Neural Network for our experiments. It comprises of 5 convolutional layers followed by 3 fully connected layers, and pooling layers to capture non-linearity (Figure 6-2). It consists of 60 million parameters, which are learned during training. There are several other deep neural networks discussed earlier that outperform AlexNet for BreaKHis cancer classification. Due to AlexNet's simple architecture, it can be trained much faster compared to other CNNs, making it our obvious choice for iterative training approach.

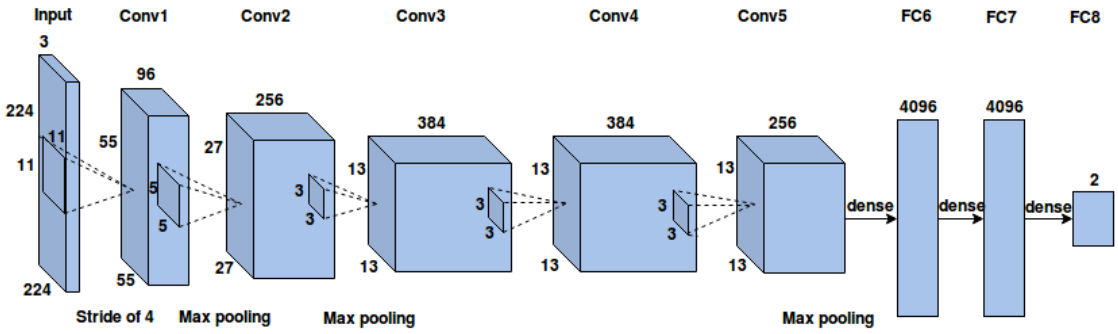


Figure 6-2. Architecture of AlexNet used the base CNN for breast cancer classification.

### 6.2.3. Data Pre-processing

The images from the BreaKHis dataset are downsized to 224×224 size, for faster training of the CNN. Before using images for training the CNN, they are standardized by subtracting the mean value and dividing by standard deviation value. This rescales all the images to a mean of 0 and unit variance, which helps in faster training of the CNN. Image data augmentation methods like random flipping, rotation by random angle, random shifting, blurring to add random noise are used to artificially expand the dataset while

training the CNN, which boosts the performance and provides a good generalization to the trained model.

### 6.2.4. Baseline Experiments

We use two experiments to define the baseline performance for the classification of breast tumor images. These will be used to quantitatively compare our proposed methods. In the first experiment, we use all the histopathological data to train an AlexNet from scratch. This will define the maximum performance for an ideal situation using all the training data. Comparing our active learning approach implemented on the same CNN with this experiment will show us how close and how fast we can reach the maximum attainable performance.

The second experiment is iterative CNN training, which involves randomly selecting and adding images to training data. We start with a small number of labeled images, around 100, to initially train the AlexNet. Out of the remaining unlabeled images, 50 images are randomly selected to be labeled at each iteration. The updated labeled images are used to retrain the AlexNet. This is continued until all the images are labeled. This experiment will serve as lower-bound for the comparison of the active learning method. Comparing the proposed method against the naive method of random selection for iterative CNN training will, in contrast, highlight how informative are the proposed selection criteria. These experiments can be used to provide an exhaustive comparison of the effectiveness of active learning strategies.

### 6.2.5. Proposed Methods

We aim to train CNNs for BreaKHis classification using less amount of labeled data. We implement this using entropy and Bayesian-based selection criteria. Algorithm 3 describes our active learning framework. A small set of labeled images (around 100) is used to train the CNN initially. We compare two active learning-based selection approaches, to pick 50 most informative images to be annotated for training the CNN. Specifically, our paper investigates the two image selection strategies based on entropy and Bayesian criteria. We obtain labels for the selected subset and add it to the training dataset. The modified training dataset is used to retrain the CNN. For experimental purposes, this is repeated until the whole unlabeled images have been labeled and added to the training set. Note that in practice, we only need to annotate a fraction of the entire dataset to achieve good classification accuracies. We compare these active learning strategies to train the same CNN (AlexNet here) from scratch and using random selection as the active learning criterion in Algorithm 3.

Algorithm 3: Active Learning Framework

**Input**: Unlabeled set of images $U = \{x_i\}_{i=1}^{N}$, Labeled set of images $A$, Active learning criterion $G$.

**Task:** Train classifier $f$ using active learning criterion $G$.

**Initialization:** Train classifier $f$ on dataset $A$.

1. **while U≠∅ do**
2. Compute active learning criterion value for unlabeled images $\{\boldsymbol{G(x_j)}\}_{\boldsymbol{j=1}}^{\boldsymbol{N}}$.
3. Select subset of size $\boldsymbol{k}$ from unlabeled images with highest criterion values.
4. Obtain labels for the selected subset, $\boldsymbol{A'}$.
5. Move selected subset from unlabeled image set to labeled image set:

$$\boldsymbol{U \leftarrow U - A', A \leftarrow A + A'.}$$

6. Retrain classifier $\boldsymbol{f}$ with updated labeled image set with $\boldsymbol{A}$.
7. **end while**

In our first method, the subset of images from the unlabeled set to retrain CNN is selected using Entropy. Entropy is one of the most popular methods used to measure uncertainty. It is defined for each data value as the negative logarithm of the probability mass function for that value as below

$$H = -\sum_i P_i \log_2 P_i. \tag{30}$$

Above is the entropy of a system consisting of $i$ data values, each occurring with a probability $P_i$. Its value lies between 0 and 1 with a higher value indicating more

uncertainty. While using entropy as the active learning criterion for measuring uncertainty in image classification, entropy is defined as

$$H(x, A) = -\sum_{c=1}^{C} p(c|x, A) \log_2 p(c|x, A) \tag{31}$$

where $x$ is an image from the unlabeled set of images, $p(c|x, A)$ is the probability that the image $x$ belongs to class $c$, calculated by the CNN trained on dataset $A$ and $C$ is the total number of classes. High entropy for an image indicates high uncertainty in its prediction using the CNN. Thus, this active learning criterion picks the examples from the unlabeled set of images with the highest predictive entropy for retraining purpose.

The second method uses probabilistic version of CNN, called Bayesian Neural Network (BNN). These use a prior distribution $w$ over network parameters. A neural network with any depth and non-linearities, with dropout applied before every weight layer, is mathematically equivalent to an approximated Bayesian Neural Network [74]. Dropout can be used to approximate the posterior on the weights $p(w|A)$ using Monte Carlo integration. This method has outperformed other approaches in capturing uncertainty in the case of deep learning models [75]. The predicted probability using a BNN, $p(c|x, A)$ is calculated as

$$p(c|x, A) = \int p(c|x, w)p(w|A)dw. \tag{32}$$

In the Bayesian active learning approach, we use the same criteria of entropy, but replace deterministic CNN to an approximated Bayesian CNN implemented using Monte-Carlo Dropout technique. We implement the above-discussed Entropy and Bayesian-based approach as active learning criteria, in parallel to perform classification of tumors into Malignant and Benign with less training data.

### 6.2.6. Statistical Analysis

Out of the collected dataset (7,909 images), 35% is used for validation (2,848 images), while rest is used for training (5,061 images). In the case of training with AlexNet from scratch, the entire training dataset of 5,061 images is used for the purpose. In the case of iterative selection approaches (entropy-based, Bayesian-based and random), 2% of the whole training set is used for initializing the CNN (100 images), and 98% is used for fine-tuning (4,961 images) as per the selection criteria. We use the accuracy on the above mentioned fixed validation set as a performance indicator to compare different approaches. Note that the validation set is constant for all training approaches, and it has no overlapping images with the training dataset. The validation accuracy is calculated after retraining the CNN each time with images picked using selection criteria in case of iterative selection approaches.

Accuracy can be a slightly misleading metric in case of an imbalanced dataset. Thus, we also compare the Area under Receiver Operating Characteristics (ROC) curve when the validation accuracy converges for each of the approaches. Area under curve (AUC) determines how well the model can distinguish between classes. The AUC ranges between 0 and 1, closer to 1 indicates good separability of the classifier.

## 6.3 Results

### 6.3.1. Accuracy based analysis

We first compare the performance of active learning methods and above-discussed baseline approaches using accuracy on the validation set (Figure 6-3). Training an AlexNet with all 5,061 training samples give 91.19% accuracy on the validation set. This is the maximum attainable accuracy with given training samples. Random selection converges to a similar accuracy using around 4,000 training samples. This means if we iteratively train CNN, selecting and adding training samples randomly, then with almost 4,000 training samples, we can achieve the maximum accuracy of 91.19%. Entropy and Bayesian-based active learning provide the same maximum accuracy (of 91.19%) using around 2,500 training samples. This implies that using these criteria for image selection, CNN can achieve the maximum accuracy much earlier. Analyzing the validation accuracy indicates that proposed active learning criteria use only 50% of the training dataset, to provide maximum performance in terms of accuracy.

We approximate the accuracy plots using least-square fitting as demonstrated in Figure 6-4 random selection accuracy is linear in nature, whereas entropy and Bayesian-based active learning accuracy curves are negatively exponential in nature. We further analyze the slopes of accuracy plots for different selection criteria. Slope here is the ratio between the increase in accuracy and an increase in the number of training samples. The slope of random selection (Figure 6-4) is almost constant throughout. This means if we randomly select training samples for fine-tuning, the accuracy will increase at a linear rate with the number of training samples. Active learning-based selection (both Entropy and Bayesian)

starts with a high slope, in the beginning, almost 10 times that in random selection. It decreases quickly at first and slowly later, saturating around 4,000 training samples. This indicates that for active learning selection criteria, accuracy quickly increases with an increasing number of training samples in the starting, implying they are highly effective with even a small amount of training data. Thus, we can conclude that in cases with a very large number of training samples, entropy and Bayesian active learning will outperform the random selection strategy much earlier.

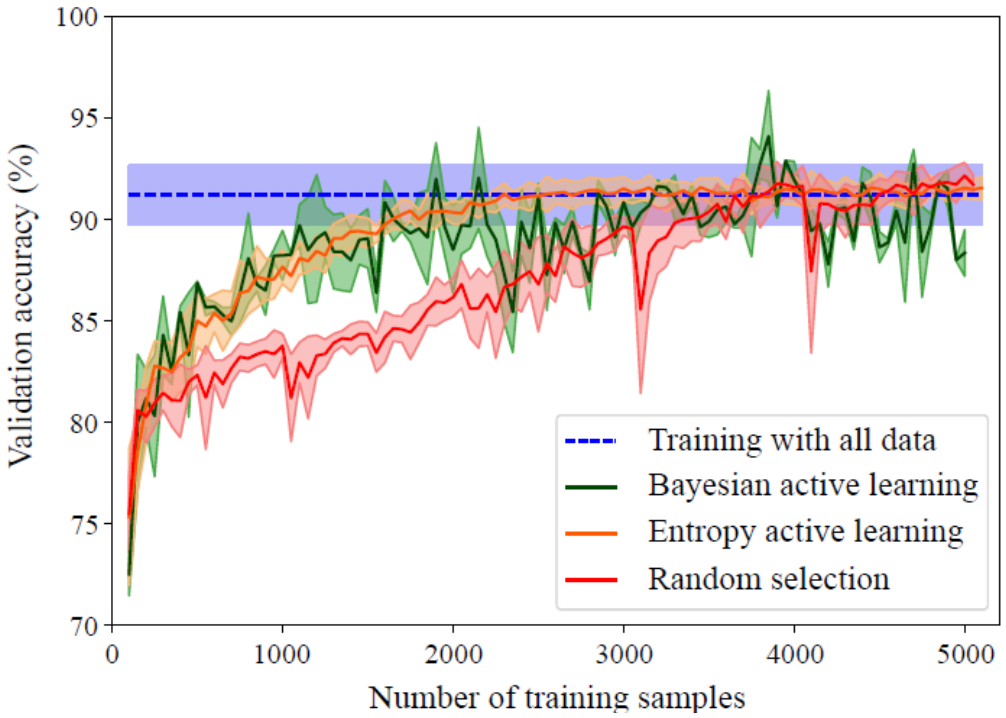


Figure 6-3. Comparing validation accuracy for comparative active learning approaches and baseline. The shaded area around each curve shows one standard deviation around the mean accuracy curve obtained through multiple repetitions.

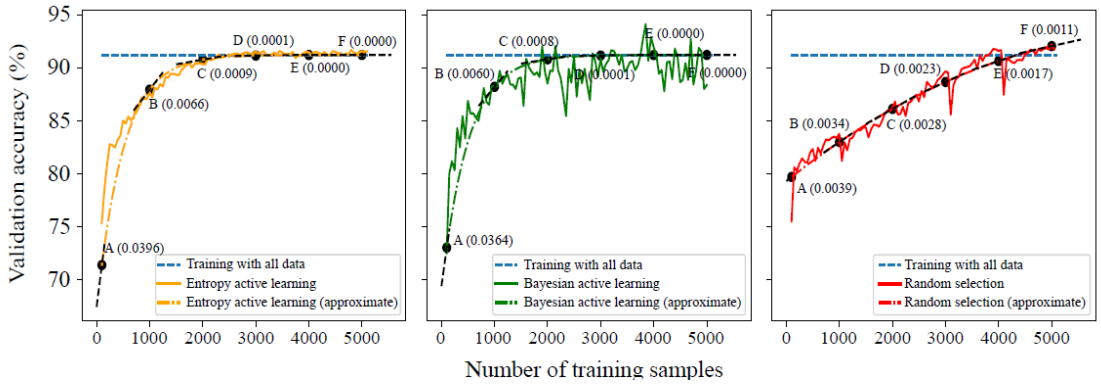


Figure 6-4. Curve fitting to validation accuracy plots of comparative active learning approaches, with slope values for A, B, C, D, E, F which correspond to selecting 100, 1000, 2000, 3000, 4000 and 5000 samples for training respectively.

Table 6-3. Comparison of breast cancer classification methods.

| Method | Classification Accuracy | Training Dataset Size |
|---|---|---|
| Handcrafted features [45] | 83.32 | 5,535 |
| Deep features [62] | 83.80 | 5,535 |
| AlexNet | 91.19 | 5,061 |
| Random Selection | 91.20 | 4,000 |
| CSDCNN [56] | 93.32 | 5,880 |
| IRRCNN [57] | 97.29 | 5,535 |
| Bayesian Active Learning Selection | 90.91 | 2,000 |
| Entropy Active Learning Selection | 91.20 | 2,400 |

Table 6-3 presents the classification accuracy and training dataset size of the state-of-the-art models proposed in other studies. This shows that our proposed active learning methods deliver comparable performance using minimal amount of training data.

### 6.3.2. Area under ROC curve analysis

Here (Figure 6-5) are the Receiver Operating Characteristics curves for training with all data, random selection, entropy-based active learning and Bayesian-based active learning with 2,500 training samples. We can observe that the entropy-based approach using 2,500 samples performs as good as training with all data, in terms of class separability. The Bayesian-based approach using 2,500 samples provides good class separability, but not as good as other methods. This can be due to its noisy nature compared to other approaches. We observe that using the proposed active learning approach, with 2,500 samples yields performance as good as training with all samples, in terms of both accuracy and class separability. Comparison with random selection provides us stronger evidence of the active learning selection criteria being superior. Thus, we can conclude that entropy and Bayesian-based active learning offers an advantage in training CNN with less training data.

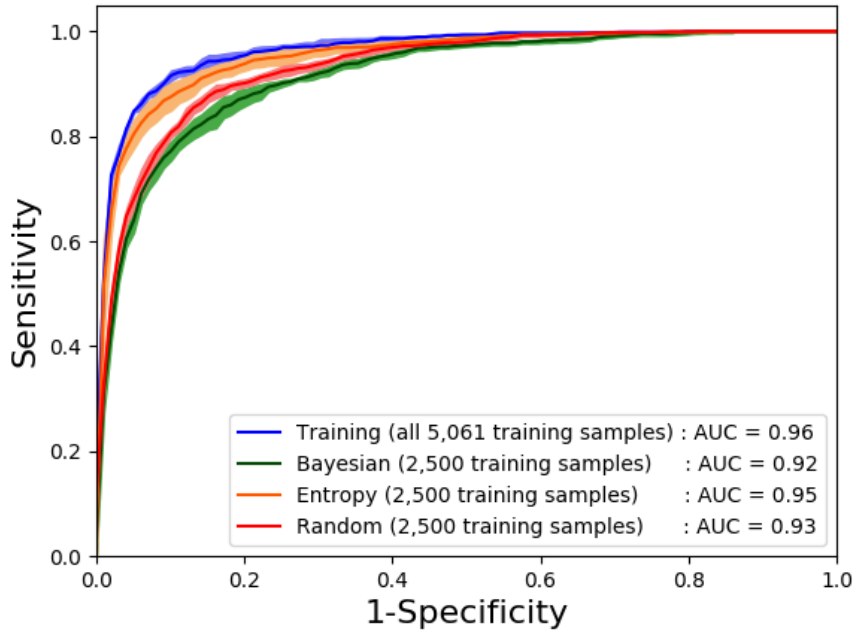


Figure 6-5. ROC curves for comparative active learning approaches. The shaded area around each curve shows one standard deviation around the mean ROC curve through multiple repetitions of each experiment.

## 6.4 Discussion

The above performance analysis indicates the superiority of proposed active learning selection over the random selection and conventional training, in delivering better performance using a minimal amount of training data. An important point to note here is that the actual sample size selected every iteration as per algorithm 3 is small (50 images) compared to the dataset size. Thus, there might be a high possibility of an intra-sample

correlation between the images selected. Due to the high dimensionality of training data involved, high entropy images don't certainly imply them being similar to each other.

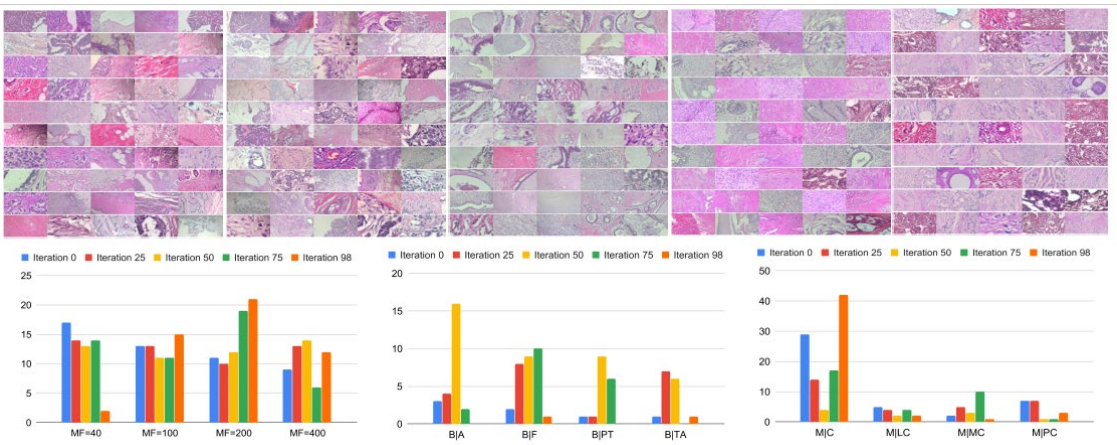


Figure 6-6. Comparing images sampled using active learning criteria during 1st, 25th, 50th , 75th and 98th iterations (out of total 100 iterations), in terms of appearance, magnification factor (MF) and subclass.

Also, as seen in Figure 6-6 (class names B: Benign, M: Malignant, and subclass names A: Adenosis, F: Fibroadenoma, PT: Phyllodes Tumor, TA: Tubular Adenoma, C: Carcinoma, LC: Lobular Carcinoma, MC: Mucinous Carcinoma, PC: Papillary Carcinoma) , images sampled at a particular iteration don't necessarily belong to a particular tumor type, sub-tumor type or magnification factor. Thus, there is no correlation between images selected in a particular sample in terms of tumor-type, sub-tumor type and magnification factor. This eliminates the possibility of overfitting problems due to correlated images sampled. So, we can establish that our method selects a diverse set of images with different magnification factors and disease classes.

Active learning and random selection approaches perform as good as training with all data, using around 2,500 and 4,000 training samples respectively. To understand what causes the difference in the performances of random and active learning-based selection, we perform an in-depth analysis of selected images during one experiment using each approach for training. We examine the image selection process using random and active learning approach in terms of tumor type, magnification level and tumor subcategory of the image selected. This will help in determining which images when selected improve the classifier's performance the most. Table 6-1 and Table 6-2 display the population distribution of histhopathological images from BreaKHis dataset in terms of tumor category, tumor sub-category and magnification values.

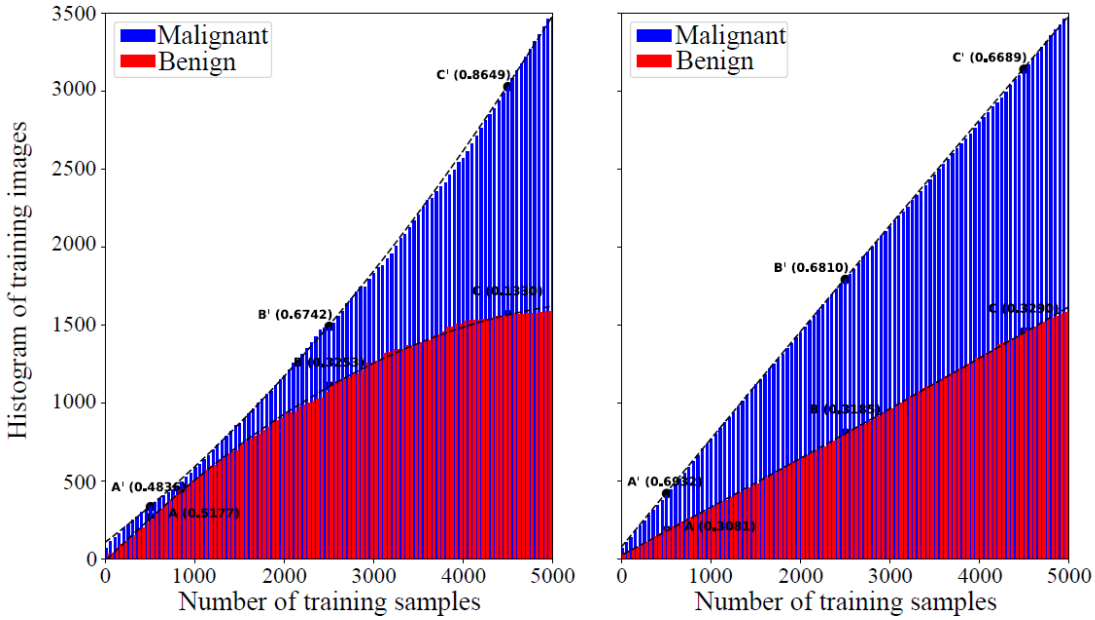


Figure 6-7. Comparing tumor type selection across training using Active learning(left) and Random(right) selection approaches, with slope values for points A(A'), B(B'), C(C') which correspond to selecting 500, 2,500 and 4,500 samples for training respectively.

Figure 6-7 compares tumor type histograms (Malignant or Benign) of the images selected by active learning strategy and random selection during training. There is a total

of 2,480 benign tumor images and 5,249 malignant tumor images (Table 6-1) in the dataset. The slope here is defined as the ratio between an increase in the number of selected images belonging to a particular tumor type category and an increase in the number of training samples.

We observe that using the active learning approach, the slope is almost equal for both tumor types, in the beginning, 0.4836 for Malignant and 0.5177 for Benign. It increases for Malignant tumor images (0.6742 with 2,500 training samples) and decreases for Benign tumor images (0.3253 with 2,500 training samples) with an increasing number of training samples, indicating that the algorithm prefers selecting most Benign tumor images (minority class) in the early training iterations. On the contrary, using a random selection approach, the slope remains constant for both tumor types, throughout the training process (∼0.68 for malignant tumor images, ∼0.31 for benign tumor images). This means the random selection approach doesn't have a particular preference in terms of tumor type while picking images. Another thing to note here is that at their performance convergence (for random selection: ∼4,000 training samples, for active learning selection: ∼2,500 training samples), both the approaches consist of around 1,000 Benign tumor images in their training data.

Thus, we can conclude that the selection of a sufficient number of training samples belonging to the minority class (Benign) is important for the classifier to reach maximum performance, and the active learning approach achieves that goal earlier than random selection by prioritizing picking benign tumor images first.

We secondly study the image selection based on tumor subcategory while training. Malignant tumors can be further classified as Carcinoma, Lobular Carcinoma, Mucinous

Carcinoma, and Papillary Carcinoma. Benign tumors can belong to the following subcategories: Adenosis, Fibroadenoma, Phyllodes Tumor, and Tubular Adenoma. The tumor sub-category population distribution can be found in Table 6-2. Amongst the Benign tumor sub-categories, Fibroadenoma exists almost twice as much as Adenosis, Phyllodes Tumor, and Tubular Adenoma sub-categories. Carcinoma tumor images are five times as compared to Lobular Carcinoma, Mucinous Carcinoma, and Papillary Carcinoma.

Figure 6-8 compares the selection histogram for the sub-categories in the case of an active learning algorithm. Specifically, the selection rate (slope) increases for Carcinoma, decreases for Adenosis, Fibroadenoma, Tubular Adenoma, Mucinous Carcinoma, and remains almost constant for Phyllodes Tumor, Lobular, and Papillary Carcinoma during the training course. This indicates the active learning approach prefers adding samples with Adenosis, Fibroadenoma, Tubular Adenoma, and Mucinous Carcinoma earlier compared to in random selection. For random selection, as shown in Figure 6-9, the selection rate remains almost constant for each subcategory type. This indicates random selection doesn't have any specific preferences based on tumor sub-category for selection.

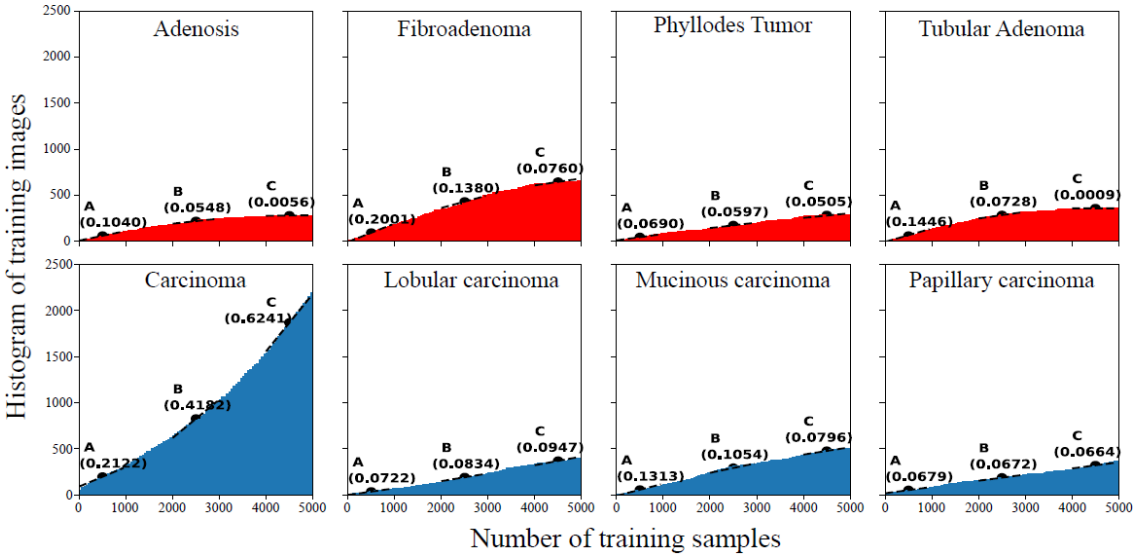


Figure 6-8. Comparing sub-category histogram of images selected using active learning approach with slope values for points A, B, C which correspond to selecting 500, 2,500 and 4,500 samples for training respectively. Benign in red, malignant in blue.

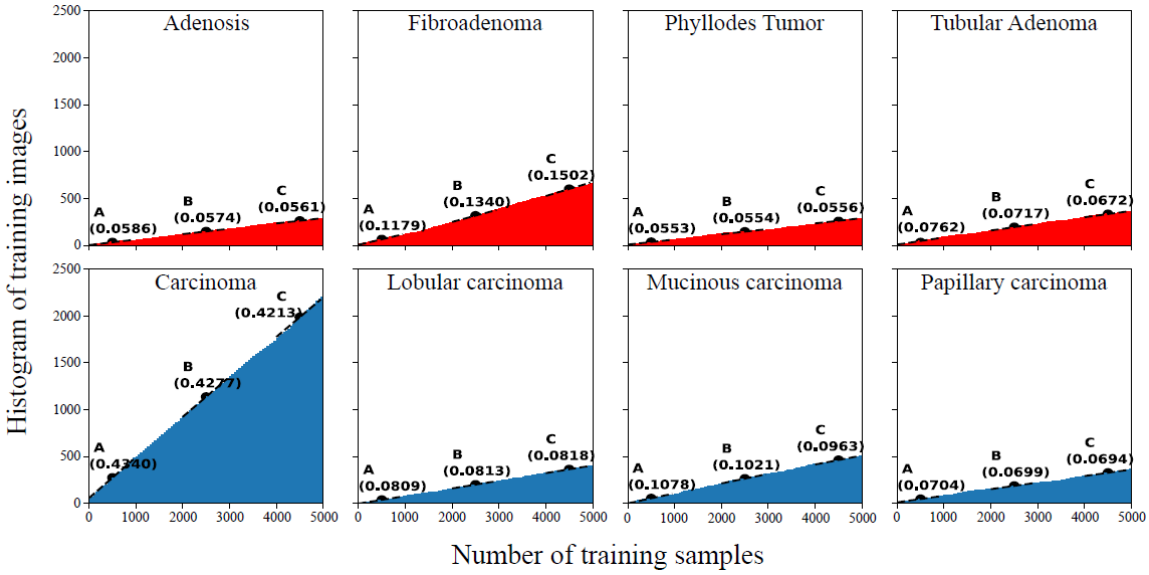


Figure 6-9. Comparing sub-category histogram of images selected using random selection approach with slope values for points A, B, C which correspond to selecting 500, 2,500 and 4,500 samples for training respectively. Benign in red, malignant in blue.

We lastly study the magnification factors of selected images across training using both selection approaches. A higher magnification factor image will include more tissue-specific information, while a lower magnification factor image will provide more information on neighboring tissues with respect to the target tissue. The BreaKHis dataset is well balanced with respect to different magnification levels (Table 6-2).

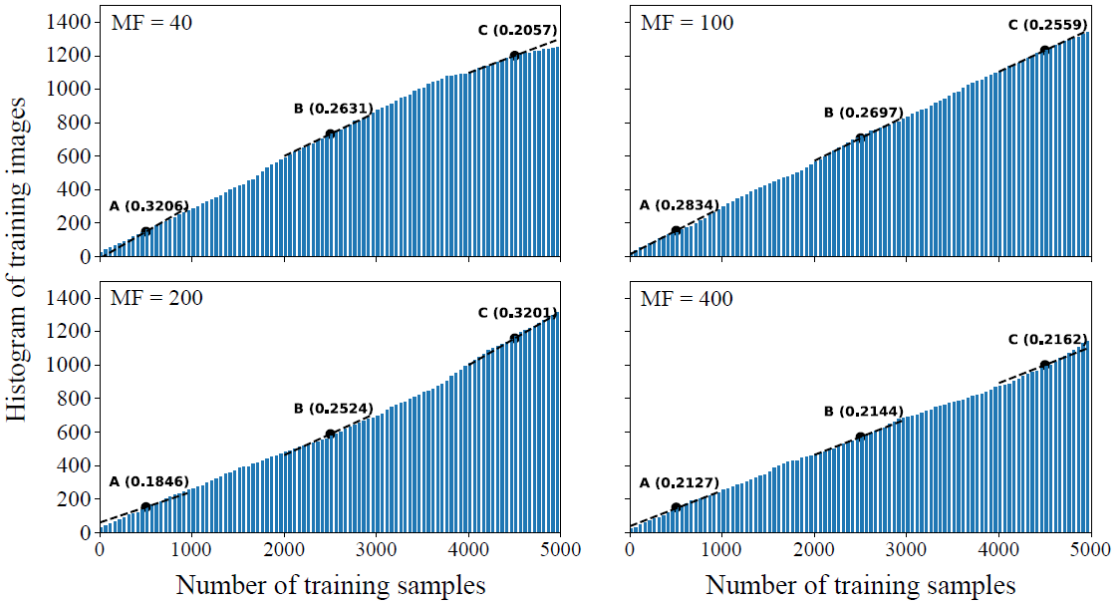


Figure 6-10. Comparing magnification factor (MF) histogram of images selected using Active learning selection approach with slope values for points A, B, C which correspond to selecting 500, 2,500 and 4,500 samples for training respectively.

Observing the active learning-based selection (Figure 6-10) for magnification factors 40×, the slope is high in the beginning and later decreases (0.3206 using 500 training samples, 0.2631 using 2,500 training samples, 0.2057 using 4,500 training samples), while for magnification factors $200\times$, the slope is low in the beginning and rises up with training (0.1846 using 500 training samples, 0.2524 using 2,500 training samples, 0.3201 using 4,500 training samples).

Comparing the slope values for all magnification factors, in the initial training iterations, it is inversely proportional to the magnification factor. Thus, we can say that for active learning selection the slope values are high for lower magnification factor images and low for higher magnification factor images in the beginning. This shows the active learning algorithm prefers selecting low magnification images earlier as compared to high magnification images. At the performance convergence (with ~2,500 images), the slope values and number of training images selected for all magnification factors are almost the same, indicating the same preference of selection to images belonging to any magnification factor, at this stage.

Using random selection, there is no particular preference while picking images in terms of the magnification factor. This can be observed from Figure 6-11 where the slope for different magnification factor images remains constant during the training. Thus, the active learning method selects low magnification images first compared to its random counterpart. This is possible because learning on low-magnification images is more challenging, as they contain high information about the tissue as well as its neighborhood. Thus, the algorithm recognizes them as highly informative and selects them earlier in the training.

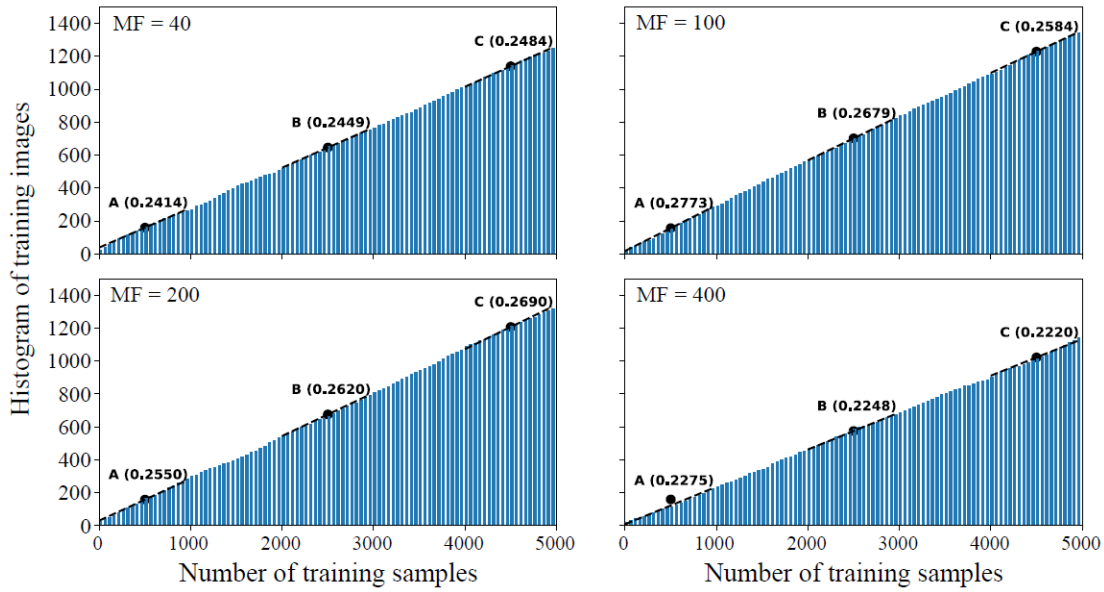


Figure 6-11. Comparing magnification factor (MF) histogram of images selected using random selection approach with slope values for points A, B, C which correspond to selecting 500, 2,500 and 4,500 samples for training respectively.

We also observe that both algorithms at their performance convergence use a training dataset balanced in terms of the magnification factor of selected images. The BreaKHis dataset is balanced in terms of magnification factors (Table 6-2) and the training set at their convergence is a good representation of the actual dataset with respect to the distribution of magnification factors.

Analyzing the statistics of images selected, we can conclude that active learning criterion selects enough samples from the minority classes, subclasses and magnification levels to make the training set a good representative of a highly variant dataset. Active learning achieves a diverse and informative training set earlier than its random selection counterpart, and hence provides the baseline performance earlier, using only half of the dataset.

## 6.5 Conclusions

In this chapter, we propose active learning frameworks to classify breast histopathological images from the BreaKHis dataset into benign and malignant with fewer training samples. The proposed methods are compared against training with all data and iterative random selection. The performance is measured in terms of accuracy and area under the ROC curves. Our approach uses less than half of the entire training dataset and delivers performance comparable to our baseline methods. We exhaustively analyze the behavior of selection strategies based on random and active learning-based selection. We observe that the proposed active learning method selects a highly variant and informative dataset, in terms of class type, subclass type, and magnification factor. This emphasizes the need for a representative training dataset to attain good performance.

Although this study focuses on a specific breast cancer dataset using a particular CNN, we believe that the key findings related to using active learning will hold for other biomedical datasets to train any deep neural network with scarce amounts of labeled data, in cases where the annotation is expensive and requires domain knowledge. Combining active learning with more sophisticated deep neural networks will tremendously cut down the high costs and effort involved in acquiring annotations for medical images, which generally make deep learning an unviable solution for medical images

## REFERENCES


[1] G. Paxinos and C. Watson, The Rat Brain in Stereotaxic Coordinates, 1983.

[2] E. A. Papp, T. B. Leergaard, E. Calabrese, G. A. Johnson and J. G. Bjaalie, "Waxholm Space atlas of the Sprague Dawley rat brain.," *NeuroImage,* vol. 97, pp. 374–386, 2014.

[3] S. W. Oh, J. A. Harris, L. Ng, B. Winslow, N. Cain, S. Mihalas, Q. Wang, C. Lau, L. Kuan, A. M. Henry, M. T. Mortrud, B. Ouellette, T. N. Nguyen, S. A. Sorensen, C. R. Slaughterbeck, W. Wakeman, Y. Li, D. Feng, A. Ho, E. Nicholas, K. E. Hirokawa, P. Bohn, K. M. Joines, H. Peng, M. J. Hawrylycz, J. W. Phillips, J. G. Hohmann, P. Wohnoutka, C. R. Gerfen, C. Koch, A. Bernard, C. Dang, A. R. Jones and H. Zeng, "A mesoscale connectome of the mouse brain," *Nature,* vol. 508, no. 7495, pp. 207–214, 2014.

[4] L. W. Swanson, "Brain maps 4.0-Structure of the rat brain: An open access atlas with global nervous system nomenclature ontology and flatmaps.," *The Journal of Comparative Neurology,* vol. 526, no. 6, pp. 935–943, 2018.

[5] A. Nuñez, M. L. Rodrigo-Angulo, I. D. Andrés and M. Garzón, "Hypocretin/Orexin neuropeptides: participation in the control of sleep-wakefulness cycle and energy homeostasis.," *Current Neuropharmacology,* vol. 7, no. 1, pp. 50–59, 2009.

[6] A. Dorr, J. G. Sled and N. Kabani, "Three-dimensional cerebral vasculature of the CBA mouse brain: a magnetic resonance imaging and micro computed tomography study.," *NeuroImage,* vol. 35, no. 4, pp. 1409–1423, 2007.

[7] D. Maric, J. Jahanipour, X. R. Li, A. Singh, A. Mobiny, H. V. Nguyen, A. Sedlock, K. Grama and B. Roysam, "Whole-brain tissue mapping toolkit using large-scale highly multiplexed immunofluorescence imaging and deep neural networks.," *Nature Communications,* vol. 12, no. 1, pp. 1550–1550, 2021.

[8] J. Jahanipour, "Fluorescence Signal Correction and Deep Cell Population Profiling Algorithms for Analyzing Multiplex Images of Whole Rat Brain Slices," 2019.

[9] R. F. Hevner, R. A. M. Daza, J. L. R. Rubenstein, H. Stunnenberg, J. F. Olavarria and C. Englund, "Beyond laminar fate: Toward a molecular classification of cortical projection/pyramidal neurons," *Developmental Neuroscience,* vol. 25, pp. 139–151, 2003.

[10] R. F. Hevner, "Layer-specific markers as probes for neuron type identity in human neocortex and malformations of cortical development.," *Journal of Neuropathology and Experimental Neurology,* vol. 66, no. 2, pp. 101–109, 2007.

[11] X. Han, D. L. Pham, D. Tosun, M. E. Rettmann, C. Xu and J. L. Prince, "CRUISE: cortical reconstruction using implicit surface evolution.," *NeuroImage,* vol. 23, no. 3, pp. 997–1012, 2004.

[12] S. B. Eickhoff, K. E. Stephan, H. Mohlberg, C. Grefkes, G. R. Fink, K. Amunts and K. Zilles, "A new SPM toolbox for combining probabilistic cytoarchitectonic maps and functional imaging data," *NeuroImage,* vol. 25, no. 4, pp. 1325–1335, 2005.

[13] B. J. Molyneaux, P. Arlotta, J. R. L. Menezes and J. D. Macklis, "Neuronal subtype specification in the cerebral cortex.," *Nature Reviews Neuroscience,* vol. 8, no. 6, pp. 427–437, 2007.

[14] B. J. Molyneaux, P. Arlotta, R. M. Fame, J. L. MacDonald, K. L. MacQuarrie and J. D. Macklis, "Novel Subtype-Specific Genes Identify Distinct Subpopulations of Callosal Projection Neurons," *The Journal of Neuroscience,* vol. 29, no. 39, pp. 12343–12354, 2009.

[15] X. Yu, S. Chung, D. Y. Chen, S. Wang, S. J. Dodd, J. R. Walters, J. T. Isaac and A. P. Koretsky, "Thalamocortical Inputs Show Post-Critical Period Plasticity," *Neuron,* vol. 74, no. 4, pp. 731–742, 2012.

[16] F. Kurth, S. B. Eickhoff, A. Schleicher, L. Hoemke, K. Zilles and K. Amunts, "Cytoarchitecture and Probabilistic Maps of the Human Posterior Insular Cortex," *Cerebral Cortex,* vol. 20, no. 6, pp. 1448–1461, 2010.

[17] R. T. Narayanan, D. Udvary and M. Oberlaender, "Cell type-specific structural organization of the six layers in rat barrel cortex," *Frontiers in Neuroanatomy,* vol. 11, pp. 91–91, 2017.

[18] N. Palomero-Gallagher and K. Zilles, "Cortical layers: Cyto-, myelo-, receptor- and synaptic architecture in human cortical areas," *NeuroImage,* vol. 197, pp. 716–741, 2017.

[19] "Cortical Layer Markers," [Online]. Available: https://www.atlasantibodies.com/primary-antibodies/neuroscience/cortical-layer-markers/.

[20] S. Sugita and T. C. Südhof, "Specificity of Ca2+-dependent protein interactions mediated by the C2A domains of synaptotagmins.," *Biochemistry,* vol. 39, no. 11, pp. 2940–2949, 2000.

[21] S. Sugita, A. Ho and T. Südhof, "NECABs: a family of neuronal Ca2+-binding proteins with an unusual domain structure and a restricted expression pattern," *Neuroscience,* vol. 112, no. 1, pp. 51–63, 2002.

[22] M. Chang and H. D. Kawai, "A characterization of laminar architecture in mouse primary auditory cortex.," *Brain Structure & Function,* vol. 223, no. 9, pp. 4187–4209, 2018.

[23] R. J. Kast, A. L. Lanjewar, C. D. Smith and P. Levitt, "FOXP2 exhibits projection neuron class specific expression, but is not required for multiple aspects of cortical histogenesis.," *eLife,* vol. 8, 2019.

[24] C. E. Rasmussen, "The Infinite Gaussian Mixture Model," *Advances in Neural Information Processing Systems 12*, 1999.

[25] C. E. Antoniak, "Mixtures of Dirichlet Processes with Applications to Bayesian Nonparametric Problems," *Annals of Statistics,* vol. 2, no. 6, pp. 1152–1174, 1974.

[26] D. M. Blei and M. I. Jordan, "Variational Inference for Dirichlet Process Mixtures," *Bayesian Analysis,* vol. 1, no. 1, pp. 121–143, 2006.

[27] H. Wu and S. Prasad, "Semi-Supervised Deep Learning Using Pseudo Labels for Hyperspectral Image Classification," *IEEE Transactions on Image Processing,* vol. 27, no. 3, pp. 1259–1270, 2018.

[28] D. M. Blei, A. Kucukelbir and J. D. McAuliffe, "Variational Inference: A Review for Statisticians," *Journal of the American Statistical Association,* vol. 112, no. 518, pp. 859–877, 2017.

[29] S. T. Mai, S. Amer-Yahia, S. Bailly, J. L. Pépin, A. D. Chouakria, K. T. Nguyen and A.-D. Nguyen, "Evolutionary Active Constrained Clustering for Obstructive Sleep Apnea Analysis," *Data Science and Engineering,* vol. 3, no. 4, pp. 359–378, 2018.

[30] J. Illian, A. Penttinen, H. Stoyan and D. Stoyan, Statistical Analysis and Modelling of Spatial Point Patterns, 2008.

[31] D. Stoyan and H. Stoyan, "Fractals, random shapes and point fields : methods of geometrical statistics," *Biometrics,* vol. 52, no. 1, p. 377, 1996.

[32] M. Megjhani, N. Rey-Villamizar, A. Merouane, Y. Lu, A. Mukherjee, K. Trett, P. H. J. Chong, C. Harris, W. Shain and B. Roysam, "Population-scale three-dimensional reconstruction and quantitative profiling of microglia arbors.," *Bioinformatics,* vol. 31, no. 13, pp. 2190–2198, 2015.

[33] P. M. Kulkarni, E. Barton, M. Savelonas, R. Padmanabhan, Y. Lu, K. Trett, W. Shain, J. L. Leasure and B. Roysam, "Quantitative 3-D analysis of GFAP labeled astrocytes from fluorescence confocal images.," *Journal of Neuroscience Methods,* vol. 246, pp. 38–51, 2015.

[34] Q. Huang, Y. Chen, S. Liu, C. Xu, T. Cao, Y. Xu, X. Wang, G. Rao, A. Li, S. Zeng and T. Quan, "Weakly Supervised Learning of 3D Deep Network for Neuron Reconstruction," *Frontiers in Neuroanatomy,* vol. 14, p. 38, 2020.

[35] D. Labate, P. Negi, B. Ozcan and M. Papadakis, "Directional ratio based on parabolic molecules and its application to the analysis of tubular structures," in *SPIE Optical Engineering + Applications*, 2015.

[36] B. W. Stewart and C. P. Wild, "World cancer report 2014.," 2014.

[37] M. Gurcan, L. Boucheron, A. Can, A. Madabhushi, N. Rajpoot and B. Yener, "Histopathological Image Analysis: A Review," *IEEE Reviews in Biomedical Engineering,* vol. 2, no. 2, pp. 147–171, 2009.

[38] B. Stenkvist, S. Westman-Naeser, J. Holmquist, B. Nordin, E. Bengtsson, J. Vegelius, O. Eriksson and C. H. Fox, "Computerized Nuclear Morphometry as an Objective Method for Characterizing Human Cancer Cell Populations," *Cancer Research,* vol. 38, no. 12, pp. 4688–4697, 1978.

[39] T. Ojala, M. Pietikainen and T. Maenpaa, "Multiresolution gray-scale and rotation invariant texture classification with local binary patterns," *IEEE Transactions on Pattern Analysis and Machine Intelligence,* vol. 24, no. 7, pp. 971–987, 2002.

[40] Z. Guo, L. Zhang and D. Zhang, "A Completed Modeling of Local Binary Pattern Operator for Texture Classification," *IEEE Transactions on Image Processing,* vol. 19, no. 6, pp. 1657–1663, 2010.

[41] V. Ojansivu and J. Heikkilä, "Blur Insensitive Texture Classification Using Local Phase Quantization," in *ICISP '08 Proceedings of the 3rd international conference on Image and Signal Processing*, 2008.

[42] R. M. Haralick, K. Shanmugam and I. Dinstein, "Textural Features for Image Classification," *systems man and cybernetics,* vol. 3, no. 6, pp. 610–621, 1973.

[43] V. Gupta and A. Bhavsar, "Breast Cancer Histopathological Image Classification: Is Magnification Important?," in *2017 IEEE Conference on Computer Vision and Pattern Recognition Workshops (CVPRW)*, 2017.

[44] M. Kandemir, C. Zhang and F. A. Hamprecht, "Empowering multiple instance histopathology cancer diagnosis by cell graphs.," in *Medical image computing and computer-assisted intervention : MICCAI ... International Conference on Medical Image Computing and Computer-Assisted Intervention*, 2014.

[45] F. A. Spanhol, L. S. Oliveira, C. Petitjean and L. Heutte, "A Dataset for Breast Cancer Histopathological Image Classification," *IEEE Transactions on Biomedical Engineering,* vol. 63, no. 7, pp. 1455–1462, 2016.

[46] M. Veta, J. P. W. Pluim, P. J. v. Diest and M. A. Viergever, "Breast Cancer Histopathology Image Analysis: A Review," *IEEE Transactions on Biomedical Engineering,* vol. 61, no. 5, pp. 1400–1411, 2014.

[47] Y. Bengio, A. Courville and P. Vincent, "Representation Learning: A Review and New Perspectives," *IEEE Transactions on Pattern Analysis and Machine Intelligence,* vol. 35, no. 8, pp. 1798–1828, 2013.

[48] Y. M. George, H. H. Zayed, M. I. Roushdy and B. M. Elbagoury, "Remote Computer-Aided Breast Cancer Detection and Diagnosis System Based on Cytological Images," *IEEE Systems Journal,* vol. 8, no. 3, pp. 949–964, 2014.

[49] Y. Zhang, B. Zhang, F. Coenen and W. Lu, "Breast cancer diagnosis from biopsy images with highly reliable random subspace classifier ensembles," in *Machine Vision and Applications archive*, 2013.

[50] G. J. S. Litjens, T. Kooi, B. E. Bejnordi, A. A. A. Setio, F. Ciompi, M. Ghafoorian, J. A. W. M. V. D. Laak, B. V. Ginneken and C. I. Sánchez, "A survey on deep

learning in medical image analysis," *Medical Image Analysis,* vol. 42, pp. 60–88, 2017.

[51] Z. Hu, J. Tang, Z. Wang, K. Zhang, L. Zhang and Q. Sun, "Deep learning for image-based cancer detection and diagnosis − A survey," *Pattern Recognition,* vol. 83, pp. 134–149, 2018.

[52] F. A. Spanhol, L. S. Oliveira, C. Petitjean and L. Heutte, "Breast cancer histopathological image classification using Convolutional Neural Networks," in *2016 International Joint Conference on Neural Networks (IJCNN)*, 2016.

[53] N. Bayramoglu, J. Kannala and J. Heikkila, "Deep learning for magnification independent breast cancer histopathology image classification," in *2016 23rd International Conference on Pattern Recognition (ICPR)*, 2016.

[54] B. Wei, Z. Han, X. He and Y. Yin, "Deep learning model based breast cancer histopathological image classification," in *2017 IEEE 2nd International Conference on Cloud Computing and Big Data Analysis (ICCCBDA)*, 2017.

[55] C. Szegedy, W. Liu, Y. Jia, P. Sermanet, S. Reed, D. Anguelov, D. Erhan, V. Vanhoucke and A. Rabinovich, "Going deeper with convolutions," in *2015 IEEE Conference on Computer Vision and Pattern Recognition (CVPR)*, 2015.

[56] Z. Han, B. Wei, Y. Zheng, Y. Yin, K. Li and S. Li, "Breast Cancer Multi-classification from Histopathological Images with Structured Deep Learning Model.," *Scientific Reports,* vol. 7, no. 1, p. 4172, 2017.

[57] Z. Alom, C. Yakopcic, M. S. Nasrin, T. M. Taha and V. K. Asari, "Breast Cancer Classification from Histopathological Images with Inception Recurrent Residual

Convolutional Neural Network," *Journal of Digital Imaging,* vol. 32, no. 4, pp. 605–617, 2019.

[58] K. He, X. Zhang, S. Ren and J. Sun, "Deep Residual Learning for Image Recognition," in *2016 IEEE Conference on Computer Vision and Pattern Recognition (CVPR)*, 2016.

[59] R. Girshick, J. Donahue, T. Darrell and J. Malik, "Rich Feature Hierarchies for Accurate Object Detection and Semantic Segmentation," in *CVPR '14 Proceedings of the 2014 IEEE Conference on Computer Vision and Pattern Recognition*, 2014.

[60] C. Szegedy, S. Ioffe, V. Vanhoucke and A. A. Alemi, "Inception-v4, Inception-ResNet and the Impact of Residual Connections on Learning," in *Proceedings of the Thirty-First AAAI Conference on Artificial Intelligence*, 2016.

[61] Y. Bengio, "Deep Learning of Representations for Unsupervised and Transfer Learning.," in *Proceedings of ICML Workshop on Unsupervised and Transfer Learning*, 2012.

[62] F. A. Spanhol, L. S. Oliveira, P. R. Cavalin, C. Petitjean and L. Heutte, "Deep features for breast cancer histopathological image classification," in *2017 IEEE International Conference on Systems, Man, and Cybernetics (SMC)*, 2017.

[63] D. Wang and Y. Shang, "A new active labeling method for deep learning," in *Neural Networks (IJCNN), 2014 International Joint Conference on*, 2014.

[64] A. Samat, J. Li, S. Liu, P. Du, Z. Miao and J. Luo, "Improved hyperspectral image classification by active learning using pre-designed mixed pixels," *Pattern Recognition,* vol. 51, pp. 43–58, 2016.

[65] Z. Zhou, J. Shin, L. Zhang, S. Gurudu, M. Gotway and J. Liang, "Fine-Tuning Convolutional Neural Networks for Biomedical Image Analysis: Actively and Incrementally," in *2017 IEEE Conference on Computer Vision and Pattern Recognition (CVPR)*, 2017.

[66] A. J. Joshi, F. Porikli and N. Papanikolopoulos, "Multi-class active learning for image classification," in *2009 IEEE Conference on Computer Vision and Pattern Recognition*, 2009.

[67] D. Koller and S. Tong, "Active learning: theory and applications," 2001.

[68] X. Zhu, J. Lafferty and Z. Ghahramani, "Combining active learning and semi-supervised learning using Gaussian fields and harmonic functions," in *In: (Proceedings) 20th International Conference on Machine Learning workshop. (2003)*, 2003.

[69] X. Li and Y. Guo, "Adaptive Active Learning for Image Classification," in *2013 IEEE Conference on Computer Vision and Pattern Recognition*, 2013.

[70] O. M. Aodha, N. D. F. Campbell, J. Kautz and G. J. Brostow, "Hierarchical Subquery Evaluation for Active Learning on a Graph," in *CVPR '14 Proceedings of the 2014 IEEE Conference on Computer Vision and Pattern Recognition*, 2014.

[71] B. Kwolek, M. Koziarski, A. Bukała, Z. Antosz, B. Olborski, P. Wąsowicz, J. Swadźba and B. Cyganek, "Breast Cancer Classification on Histopathological Images Affected by Data Imbalance Using Active Learning and Deep Convolutional Neural Network," in *International Conference on Artificial Neural Networks*, 2019.

[72] Q. Qi, Y. Li, J. Wang, H. Zheng, Y. Huang, X. Ding and G. K. Rohde, "Label-Efficient Breast Cancer Histopathological Image Classification," *IEEE Journal of Biomedical and Health Informatics,* vol. 23, no. 5, pp. 2108–2116, 2019.

[73] A. Mobiny, H. V. Nguyen, S. Moulik, N. Garg and C. C. Wu, "DropConnect Is Effective in Modeling Uncertainty of Bayesian Deep Networks," *arXiv preprint arXiv:1906.04569,* 2019.

[74] Y. Gal and Z. Ghahramani, "Dropout as a Bayesian approximation: representing model uncertainty in deep learning," in *ICML'16 Proceedings of the 33rd International Conference on International Conference on Machine Learning - Volume 48*, 2016.

[75] Y. Gal, R. Islam and Z. Ghahramani, "Deep Bayesian active learning with image data," in *Proceedings of the 34th International Conference on Machine Learning - Volume 70*, 2017.

[76] Y. LeCun, Y. Bengio and G. Hinton, "Deep learning," *Nature,* vol. 521, no. 7553, pp. 436–444, 2015.

[77] A. Krizhevsky, I. Sutskever and G. E. Hinton, "ImageNet classification with deep convolutional neural networks," *Communications of The ACM,* vol. 60, no. 6, pp. 84–90, 2017.

[78] Y. Jiang, L. Chen, H. Zhang and X. Xiao, "Breast cancer histopathological image classification using convolutional neural networks with small SE-ResNet module.," *PLOS ONE,* vol. 14, no. 3, 2019.